Summer 6-15-2023

Role of Defect Type in Optimizing Photoelectrochemical Hydrogen Production Catalysts

Mohamed Mahrous
mohamedmahrous1@aucegypt.edu

The American University in Cairo
الجامعة الأمريكية بالقاهرة

Graduate Studies

Role of Defect Type in Optimizing Photoelectrochemical Hydrogen Production Catalysts

A Thesis Submitted by

Mohamed Mahrous

to the

Nanotechnology program

July 2023

in partial fulfillment of the requirements for the degree of
Master of Science in Nanotechnology

Declaration of Authorship

I, Mohamed Mahrous declare that this thesis titled, "Role of Defect Type in Optimizing Photoelectrochemical Hydrogen Production Catalysts" and the work presented in it are my own. I confirm that:

- This work was done wholly or mainly while in candidature for a research degree at this University.
- Where any part of this thesis has previously been submitted for a degree or any other qualification at this University or any other institution, this has been clearly stated.
- Where I have consulted the published work of others, this is always clearly attributed.
- Where I have quoted from the work of others, the source is always given. With the exception of such quotations, this thesis is entirely my own work.
- I have acknowledged all main sources of help.
- Where the thesis is based on work done by myself jointly with others, I have made clear exactly what was done by others and what I have contributed myself.

Signed:

_____

Date:

_____

Abstract

The search for new energy sources has become a global challenge due to the increasing demand for energy and the negative impact of traditional energy sources on the environment. The photoelectrochemical water splitting has emerged as a promising alternative source for producing hydrogen, which can be used as a clean fuel. However, it is necessary to tailor the properties of the light-active material that will be used to absorb sunlight and split water. This research project aimed at providing detailed insights into the effect of varying the type and concentration of defects on the optical and electronic properties of diamond as a catalyst for photoelectrochemical water splitting. This study focused on three categories of dopants, including one, two, and three substituted boron atoms, as well as additional substitution dopants, such as nitrogen. The selection of boron and nitrogen dopants was based on their rich p- and n-characteristics, respectively, which could enhance the catalytic properties of the material. Interstitial hydrogen atoms were also introduced as another type of defect to stress the lattice atoms and cause variations in the electronic and optical properties of the material.

The results showed that the type and concentration of dopants is significantly affecting the band gap, dielectric constant, and absorption of the material. The band gap decreased with increasing the concentration of dopants, indicating that higher dopant concentrations enhanced the ability of the material to conduct electricity. The dielectric constant and absorption coefficient also showed a strong dependence on the type and concentration of dopants. For example, the addition of interstitial hydrogen atoms caused a significant reduction in the dielectric constant, while the addition of nitrogen dopants increased the absorption coefficient of the material. The study also applied the conclusions drawn from the analysis to another material, CuO, and found that the material exhibited the expected behavior. This finding indicates that the conclusions drawn from the analysis of the first material are generally applicable to other materials.

Acknowledgements

I would like to express my deepest gratitude to my advisor, Dr. Nageh, for his unwavering support, guidance, and encouragement throughout my M.Sc. journey. His expertise, knowledge, and insightful feedback have been instrumental in shaping my research project and developing my skills as a researcher. I am truly fortunate to have had such a dedicated and supportive mentor who taught me valuable lessons in research methodology, critical thinking, and problem-solving. His mentorship has been a transformative experience that has helped me grow both personally and professionally.

I would also like to extend my sincere thanks to my family for their continuous support, encouragement, and understanding during the ups and downs of my M.Sc. journey. Their unwavering emotional support, motivation, and words of encouragement have been invaluable in keeping me focused and motivated, and helping me persevere through the challenges I faced. Their support has been a constant source of inspiration and has given me the strength to overcome obstacles and achieve my goals.

Also, I am deeply grateful to my colleagues in the EML lab for their collaboration, constructive feedback, and insightful discussions that enriched my research experience and helped me achieve my goals. Their contributions have been invaluable in shaping my research project and broadening my understanding of the field. I am grateful for the opportunity to work alongside such talented and dedicated individuals who share a passion for research and innovation.

Finally, I would like to extend my heartfelt thanks to everyone who has supported me along the way. To my family, friends, colleagues, and mentors, you have been my pillars of strength throughout this journey, and I am forever grateful for your unwavering support and encouragement. This achievement would not have been possible without you.

Dedication

I dedicate this thesis to my mother and my father.

Contents

List of Figures

List of Abbreviations

PPM	**Part Per Million**
PEC	**photoelectrochemical**
TW	**Terawatt**
GW	**Gigawatt**
UV	**Ultraviolet light**
DFT	**Density Functional theory**
SCF	**Self-Consistent Field**
LDA	**Local Density Approximation**
GGA	**General Gradient Approximation**
LSDA	**Local Spin Density Approximation**
FFT	**Fast Fourier transformation**
PAW	**Projector-Augmented Wave**
VASP	**Vienna Ab initio Simulation Package**
ABINIT	**AB Initio Numerical Implementation on Top of the Innovative and robust library**
TMO's	**Transition Metal Oxides**
MO	**Molecular Orbitals**
VBM	**Valence Band Maximum**
CBM	**Conduction Band Minimum**
XRD	**X-ray Diffraction**
STEM	**Scanning Transmission Electron Microscopy**
EPR	**Electron Paramagnetic Resonance**
FCC	**Face Centered Cubic**
BS	**Band Structure**
HOMO	**Highest-Occupied-Molecular-Orbital**
LUMO	**Lowest-Unoccupied-Molecular-Orbital**
CASTEP	**Cambridge Serial Total Energy Package**
CB	**Conduction Band**
PBE	**Perdew-Burke-Ernzerhof**
BFGS	**Broyden-Fletcher-Goldfarb-Shanno**
PW19	**Perdew-Wang 1991**
MVB	**Maximum Energy of Valence Band**
MCB	**Minimum Energy of Conduction Band**
PDOS	**Partial Density of States**
OER	**Oxygen Evolution Reaction**
HER	**Hydrogen Evolution Reaction**
EBS	**Electronic Band Structure**
S.T.P	**Standard Temperature and Pressure**

List of Symbols

H	**Hamiltonian operator**
Ψ	**Wavefunction**
E	**Eigenvalue of the system**
$\hbar$	**reduced Planck's constant**
V	**Potential Energy**
∇	**Laplace Operator in x, y, z**
Tn	**nuclei kinetic operators**
Te	**electrons kinetic operators**
Vnn	**Coulombic interactions between nuclei-nuclei**
Vne	**Coulombic interactions between nuclei-electrons**
Vee	**Coulombic interactions between electrons-electrons**
$\Psi_n(R)$	**wavefunction describing nuclei in position R**
$\Psi_n(r, R)$	**wavefunction describing lectrons around nuclei in position R and electrons in position r**
En	**nuclei energy**
Ee	**electronic energy**
$\rho(r)$	**Electron Density**
$V_{ext}(r)$	**External Potential Function**
E_{Total}	**Total Energy**
E_{GS}	**Ground-state energy of a system**
$v_{eff}\ (r)$	**Kohn-sham potential**
$T(\rho)$	**kinetic energy of non-interacted electrons**
$E_{ee}(\rho)$	**Energy of electrons interactions**
$V_{XC}\ (\rho)$	**Exchange-correlation potential**
$E_{xc}\ (\rho)$	**Exchange-correlation energy**
r	**Electron position**
Ψ_B	**Bloch wave**
u(r)	**periodic function**
l	**Unit cell length**
k	**Crystal momentum vector**
e	**Euler's number**
i	**imaginary number**
G	**Reciprocal lattice vector**
ΔS	**entropy**
ΔG	**Gibbs free energy change**
ΔH	**enthalpy**
T	**Temperature**
ΔHf	**Formation Energy**

ΔS_f	**Entropy of formation**
ΔE	**Energy Difference**
m^*	**Effective mass**
F	**The Coupling strength**
ε	**complex dielectric function**

Chapter 1

Introduction and Scope of the Thesis

1.1 Building a Sustainable Future

Since the first day of the human discovery of fire, his lifestyle has changed. In the beginning, the fire was mainly used for warming; then, humans used it for a range of activities such as cooking, light on night, inventing the pottery wheel, and smelting metals [1]. This progress started a sequence of changes that shaped human civilization for eras; it increased the need for more energy resources ending with the coal discovery and the invention of steam engines, which played a crucial role in the industrial revolution of the 19th century [2]. The power level provided by coal and steam engines enabled us to upscale the manufacturing of goods and the innovation of new industries, such as steel manufacturing and transportation [3]. That impacted society, leading to economic and technological growth, which in turn required a higher energy supply. Fossil fuels were a strong candidate for this purpose of energy supply to meet our industrial needs, primarily if they were used in supplying different types of energy, such as electricity that expanded the circle of industrial applications [4]. However, Fossil fuels have a negative impact on the environment, leading to raising awareness of the need to move to renewable energy sources. As a result, of that negative environmental impact, we are now facing the dual challenge of meeting the rapid growth in energy demand while alleviating the negative impacts of climate change.

During the 19th century, it was observed that most of the carbon dioxide and CO_2 gases in the atmosphere were produced from fossil fuel combustion, which was postulated later by

Arrhenius to be the main responsible for the greenhouse effect and causing global warming. Recently, due to the increased awareness of the climate change challenges, countries started to monitor the concentration of atmospheric carbon dioxide CO_2 [5,6]. In 2023, the concentration of atmospheric CO_2 reached an extraordinary stage of 423.28 parts per million (ppm) [7], representing a 0.7% increase since last year [8]. Climate models predict the concentration of atmospheric CO_2 to reach 550 ppm by 2030 as shown in Figure 1. If this ratio continues, it will eventually cause a catastrophic effect similar in magnitude to the last ice age but in an opposite sign of temperature.

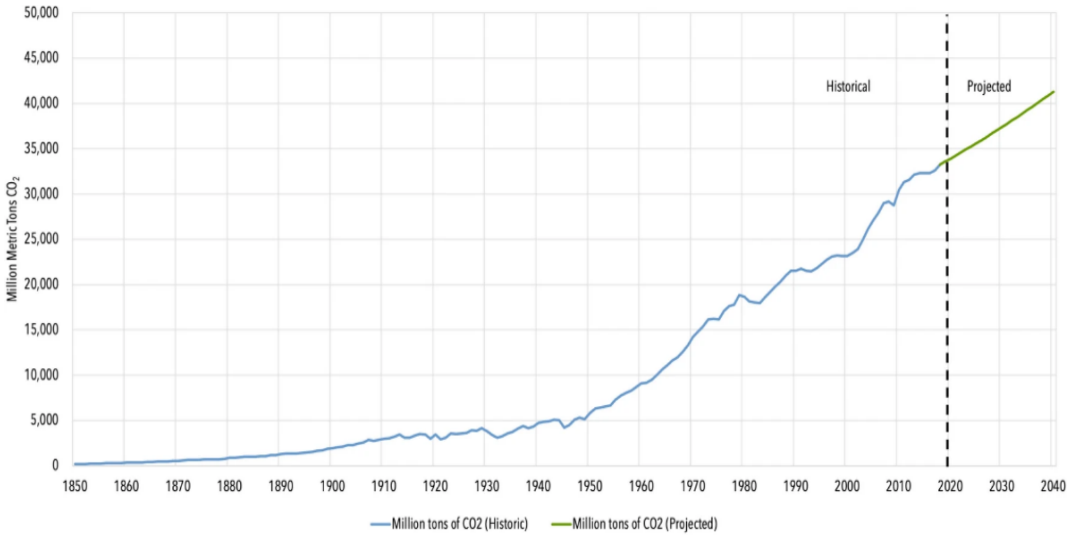

Figure 1: Global CO_2 emissions since 1850 to 2040 (International Energy Agency) [7]

Every year, the number of populations around the world is dramatically increasing, this increase reflects the expected growth in the usage of power sources depending on fossil fuels [10,11]. Therefore, that would increase carbon monoxide emissions; most populations reside in developing countries. Those developing countries are intended to enhance their quality of life, and therefore, the demand for carbon-based energy sources would increase significantly and negatively affect the environment. The daily use of hydrocarbon-based energy sources such as

coal and oil for the purpose of transporting and manufacturing This would increase the effect of greenhouse gases on the environment [12].

The most produced gas among the greenhouse gases is carbon monoxide, which is the main responsible for raising the average global temperatures [13]. Scientists are not concerned about climate change; it is typical and expected; their most concerns are the speed of that change and the dramatic increase in CO_2 emissions. However, to meet the growing energy demand, you would need to generate more power; those power sources are limited to the finite amount of fossil fuels that are the primary sources of covering that demand. One more fact is that fossil fuels are nonrenewable sources [14], and that means the more you use them, the less amount will be founded for future generations, this is not sustainable, so the only attempt to generate more energy is to slow down the usage of energy sources and obviously that will not allow us to meet the growing demand for energy in the future and move from Figure 2(a) that represents the percentage of power sources in 2022 to be as wished in 2050 shown in Figure 2(b) [15].

The negatively tremendous effect on the environment and the limitations of our energy sources made it essential to recognize the consequences of our random consumption of fossil fuels and its effect on the economy, as once we have a complete understanding of this concept, we can only fully understand the economic implications of energy usage. The challenging part here is to develop the living standards for individuals without adequately harming the environment.

On the other hand, building new renewable energy sources can cover the needs of the increased population.

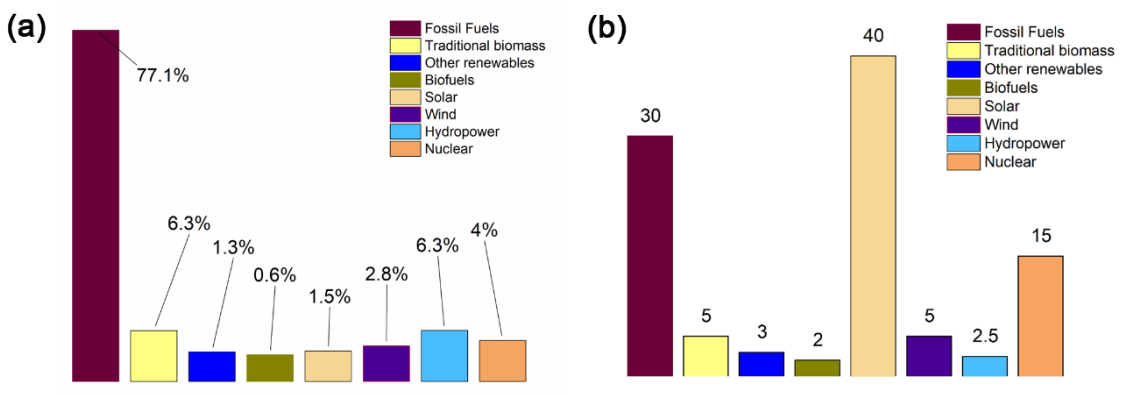

Figure 2: (a)The percentage of each power source in 2022 [15] (b) The expected percentage of each power source in 2050 [15]

1.2 The Hydrogen Revolution: Transforming How We Power Our World

The hydrogen molecule: H_2 gas, is composed of two hydrogen atoms; each atom consists of just one proton and one electron. The ionic form of hydrogen is very active and unstable, making it always found in the molecular form. However, Hydrogen gas explosively reacted, but it becomes combustible when mixed with other oxidants such as Halogens or Oxygens [16].

Hydrogen has a wide range of applications due to its outstanding physical properties of low molecular weight and high energy content under standard temperatures and pressure of 20 C and 1 atm, respectively, shown in **Table 1.1** [16]. That made it a strong candidate in the transportation and industrial processes. Despite all the advantages of hydrogen as a fuel source, its high cost of production and storage added more difficulties to the challenges of handling it safely, and here comes the role of research and development to solve those challenges making it a crucial candidate in the race of future energy production [17].

Table 1: Physical Properties of Hydrogen under S.T.P [16]

Property	amount
Density	0.0838 Kg/m^3
Diffusion Coefficient in Air	6.1 $cm^{3/s}$
Specific Heat capacity	10.16 J/g.K
Enthalpy	4098 KJ/Kg

Although all the promising physical properties of hydrogen, what makes it a strong candidate for energy production is its environmentally friendly nature. Hydrogen does not produce carbon monoxide during combustion [18]; it produces water from combustion in the air and electricity when it reacts with oxygen in fuel cells [17, 18]. These unique characteristics and others make hydrogen an ideal energy carrier. One more challenge that caused researchers racing to produce hydrogen is its poor abundance in the atmosphere [19], as it represents around 0.000055% of the air by volume [20], which imposes us to generate it to meet our energy demand while considering our climate health. For the purpose of that, the way of producing hydrogen varies depending on the source of it. It could be produced from water electrolysis, steam methane reforming, biomass gasification, coal gasification, partial oxidation, and photoelectrochemical water splitting (PEC) [21]. In this context, photoelectrochemical water splitting is the main scope of this thesis.

1.3 Solar Energy and Hydrogen Production

Hydrogen cannot be considered a primary source of energy. Otherwise, it is an energy carrier akin to electricity [22]. In order to produce hydrogen from other sources, such as hydrocarbons or water, we need to provide energy to extract it. To overcome the terawatt challenge, renewable energy is used more during these processes to decrease the carbon footprints per each energy unit produced. [23]

1.3.1 Solar Energy

The most abundant source of renewable energy is the sun; its abundancy comes from the continuous process of nuclear fusion around the day as each second sun fuses a massive amount of hydrogen atoms to form Helium atoms accompanied by a vast amount of energy released to the sun's surface causing a raise to its temperature that leads to the spectral distribution of solar radiation [24]. Although the energy radiation from the sun is abundant, this radiation is not consistent across the world [25]. What means here by solar irradiance is the amount of solar radiation that reaches a particular area, as solar irradiance varies for each particular area around the world. This variation depends on factors such as latitude, time, and weather conditions [24,25]. In addition, electricity can only be generated during the daytime; therefore, the amount of electricity generated is different and cannot be predicted [26]. Therefore, there is a need to store the electricity generated during the daytime to be used at other times when the sun's radiation is low. However, there is no ideal energy storage system to store large amounts of electricity for long periods due to the high installation and maintenance costs [27].

Moreover, transporting electricity generated from solar energy for long distances is a crucial challenge due to the energy loss resulting from transmission and distribution. Therefore, there is a need for ideal energy carriers that can store and transport the energy generated efficiently [28]. Hydrogen is considered an ideal energy carrier to meet that demand as it could be produced by variant renewable energy sources such as solar and wind energy. It could store and transport energy for later use, making it an ideal solar energy storage choice. It also produces electricity and water in fuel cells when it reacts with oxygen making it a clean energy source with high efficiency and without harmful emissions. Similarly, using hydrogen as an energy carrier will significantly reduce our dependence on fossil fuels, which is responsible for climate change.

It will be essential in meeting our future energy demand cleanly and sustainably.

1.3.2 Hydrogen Generation by Water Splitting

Establishing a sustainable hydrogen economy depends on using renewable methods for hydrogen production, which is critical for reducing our reliance on non-renewable resources and mitigating the impact of global warming [29]. Water is a primary source of hydrogen, which can be used to generate hydrogen using renewable energy sources. In 1874, In his book Mysterious Island; Jules Verne imagined the possibility of using clean hydrogen fuels, stating that water would someday be utilized as fuel and that hydrogen and oxygen would provide an endless source of heat and light [30]. This vision has become a reality, as water is recognized as the most sustainable and ideal source for hydrogen production. There are various renewable sources for producing hydrogens, such as biomass, wind, nuclear reactors, and hydroelectric power, but all of them lack applicability, as shown in **Table 1.2** [31].

It is worth mentioning that nuclear power could also be used for hydrogen production, but it is not cheaper than renewable energy sources [32]. As hydrogen is produced, thereby supplying the reactor with a mixture of fuels, such as natural gases or Biomass, under highly heated steam resulting in a mixture of hydrogen gas and carbon monoxide (CO). Likewise, this method was not demonstrated due to the challenges associated with waste disposal and the lack of public acceptance. Additionally, producing 10 TW of hydrogen via a nuclear power plant will allow us to construct a 1GW nuclear fission reactor each day for 50 years to meet our demand and consumption [33].

Table 2: Nuclear and renewable energy sources' capacity to supply energy demand by 2050.

Source	Power capacity	Comments
Biomass	10	It needs the global arable land
Wind	2.1	It needs installing windmills around all the world lands
Nuclear	8	It needs building 8000 new reactor
Hydroelectric	1.5	It needs storing all rivers behind dams

Due to all of the challenges associated with the other methods of producing hydrogen, solar power is considered one of the promising and efficient methods for producing hydrogen via water splitting reaction, among other reaction approaches [34], as shown in Figure 3. One of the approaches used in a Water splitting reaction is thermolysis, where the heat from solar radiation is used directly to split water into Oxygen and Hydrogen. This method is environment-friendly and cost-effective on large-scale approaches.

Although there are many advantages to the thermolysis process, research has shown that its efficiency is only 25%; that means for every ten water molecules, only two molecules are split and produce Oxygen and hydrogen gases [35]. This low efficiency is due to the speed of the inverse reaction of Oxygen and Hydrogen to form water under high temperatures, so the thermolysis process is not favorable for the water-splitting process [36].

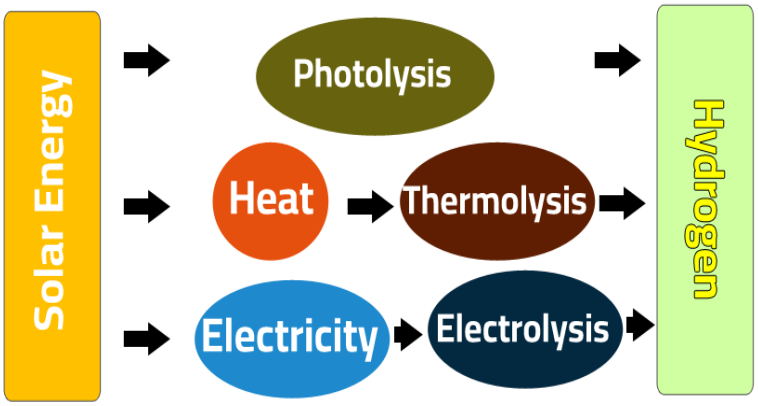

Figure 3: Hydrogen production pathways [34]

Coming to our second approach, which is the electrolysis method [37], means using electricity to split water; it is considered a simple and efficient method, as shown in the equation below:

$$H_2O\ (liquid/vapor)\ +\ electrical\ energy\ \rightarrow\ H_2\ (g)\ +\ ½\ O_2\ (g)$$

Electrolysis is a widely used method for hydrogen production, as it covers about 3.9% of the total global demand for hydrogen gas [38]. It has the power to produce hydrogen on different scales starting from lab scales to mass production. However, electrolysis efficiency is limited by the sluggish reactions on the electrodes, rate-determining steps, and, therefore, overpotentials; these challenges encouraged researchers of the field to find alternative methods for producing hydrogen via electrolysis [39].

One of the most promising approaches for splitting water is the photolysis process, which means converting light into electricity for splitting water. This method involves using photoelectrochemical cells to split water, which consists of an anode and cathode. At the anode absorbing light occurs and converting it into electricity, and at the cathode, the reaction occurs. This reaction occurs in two steps; the first step is where water oxidation occurs to form Hydrogen and Oxygen ions, then the hydrogen atoms are reduced to form hydrogen gas [40].

The Advantages of photolysis for water splitting are more than the conventional electrolysis

method as it is not dependent on the source of electricity being used, as light is being used directly to convert light into electricity and drive the reaction. Furthermore, greenhouse gases are not produced as emissions from that reaction, making it a clean and sustainable method for producing hydrogen. However, photolysis has many challenges, such as low efficiency and high synthesis cost. The use of photolysis for water splitting has several advantages over conventional water electrolysis. For one, it does not rely on external energy sources, as sunlight is used directly to drive the reaction.

Furthermore, it does not produce greenhouse gases or other harmful emissions, making it a clean and sustainable method for hydrogen production. However, there are also several challenges associated with photolysis, including the relatively low efficiency of current photoelectrochemical cells and the high cost of materials used in their construction [39, 40]. Despite those challenges, photolysis is considered a promising method in water splitting, further research and development in this area could lead to the optimization of photoelectrochemical cells and the widespread implementation of photolysis as a method for hydrogen production.

1.4 Optimizing Photoelectrochemical cell Efficiency.

The reaction type of splitting water into its constituent elements, hydrogen, and oxygen, is endothermic. That means the reaction needs to absorb energy to break the strong bonds between atoms; theoretically, the energy needed for it is approximately 1.23 V, corresponding to 285.8 KJ/mole, which could be found easily in the sun's electromagnetic spectrum [41].

Fortunately, it is not happening spontaneously because water molecules inadequately absorb the energy in the UV-Visible light region. If water molecules do not have that low absorption coefficient, global water will disappear from oceans. In the same vein, the needed

amount of energy for driving the water-splitting reaction to occur depends on several factors, such as the temperature, pressure, and catalyst used in the process. In general, the energy required to split water is related to the thermodynamic potential of the reaction, which is determined by the difference in energy between the products (hydrogen and oxygen) and the reactant (water) [42]. However, the semiconductor could be excited to work as a catalyst in the electrochemical cell by utilizing it to absorb sunlight, and therefore the reaction occurs.

In fact, improvements to photoelectrochemical water-splitting techniques are limited by the materials accessible today. The main challenges for creating a water-splitting technique are; finding a material with a proper band gap capable of capturing energy from sunlight, guaranteeing its long-term viability in various aqueous electrolytes, and curtailing charge carrier recombination [43]. On the other hand, the materials should be abundant and environmentally friendly to fit with different scalable applications found in metal oxide semiconductors and diamonds, as we will show in the coming chapters.

1.5 Scope of the Thesis

How could the defects engineer materials' optical and electronic properties ease water-splitting reactions for hydrogen production? The thesis discussed that there are different parameters, such as the defects type and defect concentration, that can control the optical and electronic properties of the materials, such as the absorption, dielectric constants, band structure, and reaction pathway. Chapter 1 introduces the story of hydrogen production, starting by mentioning the global energy challenges and how they negatively affect our climate. Then, mentioning the capability of substituting hydrogen with fossil fuels to resolve energy challenges and what is photoelectrochemical water-splitting reaction mechanism. Chapter 2 gives a general overview of the science behind simulating water-splitting reactions, starting with the theoretical

background for Density functional theory, defects, and disorders in solids and the photoelectrochemical cell reaction. Chapter 3 reveals the previously published work on the different methods used to calculate the properties of the materials based on the type of defect for water splitting reaction. Chapter 4 discusses the detailed computational methods used for our simulation. Chapter 5 discusses the results of defective diamonds and CuO. Chapter 6 gives a conclusion and future work.

Chapter 2
Fundamentals of Quantum mechanics

Schrödinger Equation is an essential mathematical expression describing quantum mechanical systems' behavior. Its importance comes from its mathematical terms, which have the wave function term that contains all the information that could be known about the system. The equation was first postulated by Erwin Schrödinger in 1925 and published the following year. Since then, it has been widely used to study the behavior of particles and atoms at a microscopic level [44].

One of the most significant implications of the Schrödinger Equation is its impact on electronic structure description. By solving the equation, scientists can determine the probability distribution of electrons in an atom or molecule. This information is essential for understanding the chemical and physical properties of materials [45]. Additionally, the Schrödinger Equation has been used to develop various computational tools, such as density functional theory (DFT), which is widely used in the field of materials science as:

$$H\Psi = E\,\Psi \qquad (1)$$

Where H, Ψ, and E are the Hamiltonian operator, the system's wavefunction, and its eigenvalue of the system energy, respectively. As the Hamiltonian operator describes the total energy of that quantum system, it could be written as the sum of the kinetic and potential energy:

$$H = \frac{-\hbar^2}{2m}\nabla^2 + V \qquad (2)$$

Where $\hbar$ is the reduced Planck's constant and equals $\frac{h}{2\pi}$, m is the mass of the system, V is the potential energy, and ∇ is a symbol of the Laplace operator and represents the kinetic energy term in x, y, and z positions of the 3D cartesian coordination:

$$\nabla^2 = \frac{\partial^2}{\partial x^2} + \frac{\partial^2}{\partial y^2} + \frac{\partial^2}{\partial z^2} \qquad (3)$$

Getting the energy of any system is a crucial factor in inspecting its properties, which could be found by solving Schrodinger's equation for straightforward systems like hydrogen atoms. In contrast, it has been found that solving Schrodinger's equation for a medium or large system model could consume a lot of time due to the complexity of its terms.

2.1 The Many-Body Problem

The many-body problem is a fundamental physics problem that occurs from attempting to describe the behavior of a system composed of many interacting particles. It is a challenge encountered in many domains, including astrophysics, condensed matter physics, and nuclear physics. It is challenging to solve because the system's behavior cannot be characterized by studying the particles in isolation. Instead, each particle's behavior is impacted by the behavior of all the other particles in the system, resulting in complicated and frequently unpredictable performance [46].

The behavior of particles in a quantum chemical system is complex due to interactions between them, such as electron-electron interaction, electron-nuclei interaction, and other cross-interactions. It is challenging to obtain a precise computation of such systems. To simplify the Schrödinger Equation, the Born-Oppenheimer approximation is commonly used. This approximation assumes that the nuclei remain static while the electrons are in their ground state, which is valid since electrons move much faster than nuclei. In this approximation, the system can be described as having stationary nuclei surrounded by electrons moving at their ground state. The Hamiltonian operator can then be separated into nuclei portion terms and electron terms as follows:

$$H = T_n + T_e + V_{nn} + V_{ne} + V_{ee} \quad (4)$$

Where T_n and T_e are nuclei and electrons kinetic operators, while V_{nn}, V_{ne}, and V_{ee} are Coulombic interactions between nuclei-nuclei, nuclei-electrons, and electrons-electrons, respectively.

Applying the Born–Oppenheimer approximation on the Schrödinger equation considering the nuclei and electron part, it could be written as:

$$\Psi(r.R) = \Psi_n(R)\,\Psi_e(r,R) \quad (5)$$

Where $\Psi_n(R)$ is the wavefunction describing nuclei in position R; while $\Psi_e(r,R)$ Is the wavefunction describing the electrons around nuclei in position R and electrons in position r. Therefore, the Schrodinger equation could solve the electronic and nuclei energy as:

$$H_e(r,R)\Psi_e(r,R) = E_e\,\Psi_e(r,R) \quad \& \quad H_n(R)\Psi_n(R) = E_n\Psi_n(R) \quad (6)$$

Where E_n and E_e represent the nuclei and electronic energy, respectively, therefore, the total energy would be:

$$E_{Total} = E_{electronic} + E_{nuclear-nuclear} \quad (7)$$

2.2 The Hartree-Fock Approximation

The self-consistent field method, also known as the Hartree method, is a computational approach used to solve the Schrödinger equation for multi-electron atoms and molecules. It is based on the assumption that the electrons in a stable molecule or atom move approximately independently of one another. In other words, the wave function of an n-electron system is approximated as the product of n single-electron wave functions; each one is determined by the electronic field created by the nucleus and other electrons [46, 47]. The total electron states are obtained by multiplying all the single-electron wave functions, leading to a simplified wave function description.

To calculate the system's energy, the Hartree method uses the self-consistent field approach, which involves solving the Schrödinger equation for each electron while keeping the electronic

field constant. The electronic field is updated after each iteration until a consistent solution is obtained.

The Hartree method has several advantages over other methods for solving the Schrödinger equation for multi-electron systems. It is pretty easy to realize and be able to be used to calculate the ground-state energy and wave function of atoms and molecules with high accuracy. However, the method has limitations, particularly for systems with electron-electron solid interactions or when the wave functions of the electrons overlap significantly.

$$\Psi_{(r)} = \Psi_{(1)}(r_1) \,.\, \Psi_{(2)}(r_2) \ldots\ldots \Psi_{(n)}(r_n) \qquad (8)$$

Back in 1930, Slater and Fock criticized the Hartree method for violating the wave function antisymmetric principle and failing to account for the spin of the electrons [48]. As an improvement, they proposed a new method called the Hartree-Fock approach better to describe the electronic wave function of a system.

The Hartree-Fock approach treated electrons as fermions [49], meaning they follow the Pauli exclusion principle, so two electrons cannot occupy the same quantum state. The method assigns each electron a unique spin state, such as spin-up or spin-down. For example, the first electron will occupy a state of $\Psi_{(1)}$ with spin α, while the second electron occupies a state of $\Psi_{(2)}$ with spin β, and so on. Coming to the antisymmetry principle that Hartree ignored, Slater used a mathematical expression to represent the wave function of the N-electron system [48, 49]. This expression, the Slater determinant, ensures that the wave function changes sign when two electrons are exchanged, as the antisymmetry principle requires.

$$\Psi_{HF} = \frac{1}{\sqrt{N!}} \begin{vmatrix} \Psi_{1,\alpha}(1) & \Psi_{1,\beta}(1) & \ldots & \Psi_{N,\beta}(1) \\ \Psi_{1,\alpha}(2) & \Psi_{1,\beta}(2) & \ldots & \Psi_{N,\beta}(2) \\ \vdots & \vdots & \vdots & \vdots \\ \Psi_{1,\alpha}(N) & \Psi_{1,\beta}(N) & \ldots & \Psi_{N,\beta}(N) \end{vmatrix} \qquad (9)$$

This Determinant represents each wave function in columns, while the electron coordinates are

in the rows. Aligned with our mathematical knowledge of the determinants' properties, exchanging any two columns or rows would change the sign of equation (2.1.2.9), which agrees with the antisymmetric principle. In other words, the rule that two different electrons cannot occupy the same electron state is based on the Pauli exclusion principle [50]. This principle is reflected in the wave function determinant, which is a mathematical property of the wave function. When two rows or columns of the Determinant are the same, the value of the Determinant becomes zero. This means that the wave function changes sign when two electrons are swapped, and that's why two electrons cannot occupy the same electron state. Hence, the Hartree-Fock approach is suitable for solving many-body problems due to five main guesses listed as follows:

(1) The Born-Oppenheimer approximation assumes that the motion of atomic nuclei in a molecule is slow compared to electrons. A molecule's wave function includes electrons and nuclei, but the approximation simplifies the calculation by treating electronic and nuclear motion separately.

(2) The method being used does not take into account any effects related to the theory of relativity. Additionally, it only uses operators that are related to non-relativistic physics.

(3) In quantum mechanics, the wave function of a system can be represented as a linear combination of mathematical functions called basis functions. These basis functions should be chosen to be orthogonal, meaning that their overlap is zero and they are independent of each other. The wave function can be accurately represented by choosing orthogonal basis functions, and simplified mathematical calculations can be performed to solve the Schrödinger equation.

(4) In quantum mechanics, a single Slater determinant represents the energy eigenfunction of a system. This Determinant describes the wave function of identical particles, like electrons, with an antisymmetric characteristic, meaning it changes sign when two similar particles are exchanged. The energy eigenfunction is expressed as a one-electron wave function that shows the

probability of finding an electron in a particular state.

(5) The Hartree-Fock method neglects electron correlation effects because it uses an approximation that assumes a mean-field environment. This last approximation is the most significant and can cause large deviations between experimental and calculated results, which can be defined as:

$$E_{Exp} - E_{HF} = E_{correlation} \qquad (10)$$

In certain situations, the Hartree-Fock method can be replaced by density functional theory (DFT) to solve the electronic structure of molecules and solids. Unlike the Hartree-Fock method, DFT considers both exchange and correlation energies simultaneously [51]. Exchange energy arises from the quantum mechanical exchange interaction between electrons, while correlation energy arises from the interactions between electrons that cannot be described by the mean field approximation.

DFT is a more robust method than Hartree-Fock as it can calculate the electronic properties of a system more accurately. By considering exchange and correlation energies, DFT can provide a more accurate description of the electronic structure of molecules and solids.

2.3 The Density Functional Theory

1960, the density functional theory (DFT) was developed to overcome the calculation errors associated with the Hartree-Fock approach with the low cost of computational resources [52]. It is used to estimate the properties of a many-electron system. In contrast to the Hartree-Fock method that used wavefunctions, DFT uses the functionals representing the spatially dependent electron density as shown in Figure 4.

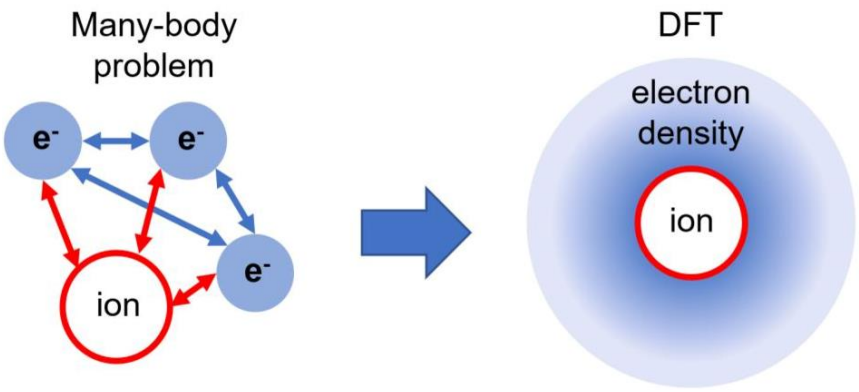

Figure 4: The difference between the hypothesis for solving many -body problem and Density functional theory [11].

In 1927, the DFT method was first presented by the Thomas-Fermi model [53]. It hypothesized that an atom is surrounded by a uniform distribution of electrons acting as a cloud around the nucleus. However, this model was lack of accuracy due to its neglect of the electron-electron interaction and, therefore, the exchange of energy. In fact, Hohenberg-Kohn theorems solved this issue and their theoretical DFT foundations in their publications.

2.3.1 The Hohenberg–Kohn Theorems

The Hohenberg-Kohn theorems are a set of fundamental theorems in density functional theory (DFT) that provide a theoretical foundation for the method [54]. The theorems state that the external potential and electron density uniquely determine a many-electron system's ground-state wave function and energy. This means that the complex and challenging problem of calculating the wave function of a many-electron system can be replaced by the more straightforward problem of estimating the electron density $\rho(r)$. Firstly, they calculated the ground state electronic energy using the electron density functional $\rho(r)$, which is a function of the external potential function $V_{ext}(r)$ and the obtained total energy E_{Total}. Additionally, a system's electron density exclusively predicts its external potential. This implies that any two

external potentials with the same electron density should share similar ground-state energies and be comparable. This theorem establishes a critical relationship between the electron density and the external potential, allowing the ground-state energy of a system to be calculated using just the electron density, as shown in equation (2.2.1.11).

$$E_{GS}[\rho(r)] \geq E_{GS}[\rho_{GS}(r)] \qquad (11)$$

Where $E_{GS}[\rho(r)]$ Is the random density calculated energy while $E_{GS}[\rho_{GS}(r)]$ is the least energy due to the ground state reached by the electron density. For simplicity, equation (2.1.1.4) of the Born-Oppenheimer approximation can be stated as follows:

$$E[\rho(r)] = T[\rho(r)] + V_{ee}[\rho(r)] + V_{en}[\rho(r)] \qquad (12)$$

2.3.2 The Kohn-Sham Equations

Based on the previously mentioned Hohenberg–Kohn Theorems, for the purpose of calculating the total energy of a system, it is essential to find out its ground state density first [55]. In 1965, Kohn-Sham hypothesized a self-consistent equation based on the Schrödinger equation of one electron problem [56]. They derived the main equation that reduced the complexity of the Slater determinant into a one electron wavefunction as shown in equation (13)

$$\left(-\frac{\hbar^2}{2m}\nabla^2 + \upsilon_{eff}(r)\right)\varphi_i(r) = \varepsilon_i\,\varphi_i(r) \qquad (13)$$

Where $\upsilon_{eff}(r)$ is the Kohn-sham potential where the particles with no interactions move.

$\varphi_i(r)$ Is Kohn-Sham orbital function with an energy ε_i

Therefore, the total electron density $\rho(r)$ Of position r could be calculated with the following expression:

$$\rho(r) = \sum_{i=1}^{N} |\varphi_i(r)| \qquad (14)$$

Hence, Equation (2.2.2.13) could be written as:

$$v_{eff}\,(r) = E_{eff}\,(r) + e^2 \int \frac{\rho(r')}{|r - r'|}\, dr' + V_{xc}\,(r) \qquad (15)$$

Therefore, when an external Kohn-Sham potential $v_{eff}(r)$ added to the equation, the total energy $E(\rho)$ Could be expressed as:

$$E(\rho) = T(\rho) + E_{ee}\,(\rho) + \int v_{eff}\,(r)\,\rho(r)\,dr\; + V_{XC}\,(\rho) \qquad (16)$$

Where $T(\rho)$ is the kinetic energy of non-interacted electrons, $E_{ee}(\rho)$ Is the energy of electrons interactions, $V_{XC}\,(\rho)$ is the exchange-correlation potential.

It is worth noting that the exchange-correlation potential is the term used to describe the effects of electron-electron interactions that are not accounted for by the Hartree-Fock approximation, which neglects electron correlation, as shown below:

$$V_{xc} = \frac{\delta E_{xc}\,(\rho)}{\delta \rho(r)} \qquad (17)$$

The exchange-correlation energy $E_{xc}\,(\rho)$ is comprised of four functionals: the Coulomb, Exchange, Correlation, and Kinetic functional.

Furthermore, It is essential to introduce some crucial approximations that lead to more accurate results of the $E_{xc}(\rho)$, such as the Generalized Gradient Approximation (GGA) and Local Density Approximation (LDA), are well-known methods in most DFT calculations.

2.3.3 Local Density Approximation (LDA)

The Local Density Approximation (LDA) is a computational method used in density functional theory (DFT) to calculate the electronic structure of a many-electron system [57]. LDA is a type of exchange-correlation energy approximation that assumes the exchange-correlation energy of a system is a function of the local electron density. In LDA, the exchange-correlation energy is approximated by considering the electron density at each point in space and assuming that the exchange-correlation energy at that point depends only on the local electron density at that point. This approximation makes the calculation of the exchange-correlation energy computationally efficient, as it reduces the number of variables that need to be considered. It is widely used in estimating the electronic structure of molecules and materials and has been shown to provide reasonable accuracy for many systems. However, it does not account for the non-local or long-range effects of electron correlation and exchange, which can sometimes lead to errors. An extension of the Local Density Approximation (LDA) in density functional theory (DFT) is the Local Spin Density Approximation (LSDA), which includes the effects of electron spin on the exchange-correlation energy. In LDA, the exchange-correlation energy is approximated as a function of the local electron density. In LSDA, the electron density is replaced by the spin density, which is the difference between the number of electrons with spin up and spin down at each point in space. The spin density is used to calculate the exchange-correlation energy, considering the effects of electron spin [58]. The inclusion of spin in LSDA allows for the calculation of magnetic properties and spin-dependent phenomena, such as spin-polarized transport and magnetism in materials; the mathematical difference between the LDA and LSDA could be expressed as:

$$E_{xc}^{LSDA}\left(\rho(r)\right) = \int \rho(r)\, \varepsilon_{xc}\left(\rho(r_{\uparrow}, r_{\downarrow})\right) dr; \qquad (18)$$

$$E_{xc}^{LDA}\left(\rho(r)\right) = \int \rho(r)\, \varepsilon_{xc}\left(\rho(r)\right) dr \qquad (19)$$

However, the LSDA is still an approximation and may not accurately describe some systems with strong electron correlation effects. Therefore, more advanced exchange-correlation energy approximations, such as the Generalized Gradient Approximation (GGA) [59] and the Hybrid Functionals [60], have been developed to improve the limitations of LSDA.

2.3.4 Generalized Gradient Approximation (GGA)

Generalized Gradient Approximation (GGA) is a computational method used in density functional theory (DFT) to calculate the electronic structure of a many-electron system [61]. GGA is an extension of the Local Density Approximation (LDA) and includes the effects of the electron density gradient on the exchange-correlation energy. In GGA, the exchange-correlation energy is approximated as a function of both the local electron density and the electron density gradient. This approximation considers the non-local and long-range effects of electron correlation and exchange that are not included in the LDA and could be expressed as:

$$E_{xc}^{GGA}\left(\rho(r)\right) = \int \rho(r)\, \varepsilon_{xc}\left(\rho(r_{\uparrow}, r_{\downarrow}, \nabla r_{\uparrow}, \nabla r_{\downarrow})\right) dr \qquad (20)$$

The GGA method has been shown to provide better accuracy than the LDA for many systems, including molecules, solids, and surfaces. However, GGA is still an approximation and may not accurately describe some methods with strong electron correlation effects. To overcome the limitations of GGA, more advanced exchange-correlation functionals have been developed, such as the hybrid functionals, which combine the GGA approximation with some exact exchange contributions. These more advanced functionals improve the accuracy of DFT calculations and make it possible to study a wide range of materials and chemical reactions with high accuracy.

2.4 Applying DFT Calculation in Solids

The Kohn-Sham equations provide an advantageous structure for understanding systems with significant interactions between electrons [62]. Though these formulas serve the purpose of modeling basic systems with numerous electrons in a confined region, they become insufficient when used to describe the movements of an unlimited number of non-interacting electrons within particular potentials. To overcome this obstacle, a limited representation basis set is used to depict significant infinite space that is made up of many repeating periodic unit cells in three dimensions. This base set is required to adequately model complicated systems' electrical structure while keeping computing costs to a minimum.

2.4.1 Basis Sets

The basis set is an array of mathematical equations employed for expressing the behavior and characteristics of the system's electrons represented by the wave function of a molecule or solid. It mathematically approximates the electronic wave function by estimating it as a linear combination of smaller functions [63]. These more specific functions are selected to be theoretically accessible and to represent the sophisticated electronic wave function while minimizing processing expense accurately. The most common basis sets used in quantum chemistry are atomic orbitals, such as the Slater-type orbitals and Gaussian-type orbitals, and plane waves, often used for solid-state calculations. However, the choice of basis set depends on the nature of the system being studied and the accuracy required for the calculation. It is typically chosen to be mathematically convenient, and they are combined in various ways to approximate the electronic wavefunction as the number and type of basis set function used in a calculation can strongly influence the accuracy of the results.

On the other hand, the size and complexity of the basis set also affect the computational cost of electronic structure calculations; Larger basis sets require more computation time and

memory, but they can provide more accurate results. Therefore, a balance must be struck between accuracy and computational efficiency when choosing a basis set. In addition to atomic orbitals and plane waves, other basis sets have been developed, such as spherical harmonics and wavelets. These basis sets are often used in specialized calculations, such as relativistic calculations or calculations involving non-equilibrium systems [64]. In this work, I used plane wave basis sets [65] as they are often used in electronic structure calculations of solids because they have several advantages that make them well-suited for this type of system.

Plane waves are a convenient choice for describing extended systems because they have a simple mathematical form and can be easily transformed between real and reciprocal space. This makes them computationally efficient, as many calculations can be performed in reciprocal space using fast Fourier transforms [66]. Also, plane wave basis sets have excellent convergence properties, meaning they can accurately represent the electronic wave function with a relatively small number of basis functions. This is important for large systems, such as solids, where the number of basis functions can become prohibitively large using other basis sets. Therefore, plane wave basis sets are well-suited for describing the properties of solids, such as band structures, because they provide a complete basis set that can explain all the periodic functions of the crystal lattice.

2.4.2 The Supercell Approach

The supercell approach is a computational method used in solid-state physics to model the electronic and structural properties of crystalline materials. The technique involves creating a more extensive unit cell, called the supercell, by replicating the original unit cell of the crystal in all three dimensions as shown in Figure 5. The supercell is typically constructed by multiplying the primitive lattice vectors of the actual unit cell by integers, resulting in a larger unit cell that

contains multiple primitive cells. It is used to study the properties of defects, impurities, surfaces, and interfaces in crystalline materials. By introducing a defect or impurity into the supercell, the electronic and structural properties of the material can be studied in the presence of the defect or impurity [67].

Similarly, it is commonly used in conjunction with electronic structure calculations, such as density functional theory (DFT), to model the electronic properties of materials. The electronic structure calculations are performed on the supercell, which includes the defect or impurity, and the results are compared to those obtained from calculations on the perfect crystal.

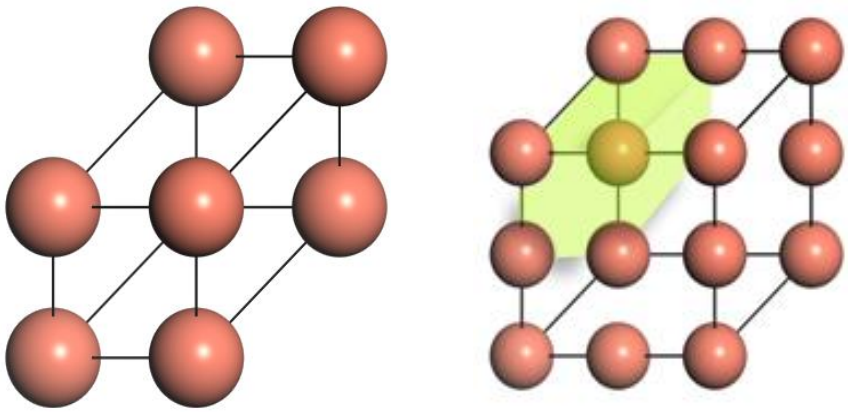

Figure 5: The difference between primitive cell on the left and supercell on the right of copper element

One of the advantages of the supercell approach is that it allows for the study of complex systems that cannot be easily studied experimentally. For example, the method can be used to investigate the properties of materials under extreme conditions, such as high pressure or high temperature, or to study the effects of doping on the electronic properties of materials. However, the supercell approach can also be computationally demanding, as the supercell size must be chosen carefully to balance accuracy and computational cost. Additionally, the method may not accurately capture the long-range effects of defects or impurities, which can be important for some systems [68].

Using conventional wavefunction approaches, the behavior of numerous electrons in a real-world system, especially those near the surface and interface, may be brutal to compute. Bloch's Theorem solves this difficulty by dividing a massive structure into more superficial unit cells that are subsequently substituted with bounded cell units in three dimensions [69]. This enables periodic problems to be addressed using Bloch's Theorem, significantly simplifying the calculations to be:

$$\Psi(r) = e^{ik.r}\, u(r) \qquad (21)$$

$$u(r) = u(r + l) \qquad (22)$$

Where r, Ψ, u(r), l, k, e, and i are the electron position, Bloch wave, periodic function, the length of the unit cell, the crystal momentum vector in the reciprocal lattice in the first Brillouin zone(Z), the Euler's number, and the imaginary number, respectively.

When a periodic function is expanded using a Fourier series, a mathematical representation of the function can be obtained:

$$u(r) = \sum_{G} C_{i,G}\, e^{iG,r} \qquad (23)$$

Where G. represents the reciprocal lattice vector, therefore, the wave function of the electrons could be written as:

$$u(r) = \sum_{G} C_{i,k+G}\, e^{i(k+G),r} \qquad (24)$$

The plane-wave basis set is created by combining multiple trigonometric functions (e^{ix} = cosx+i sinx), resulting in a wavefunction that can be easily used in periodic systems through the use of fast Fourier transformation (FFT) to convert between real space and reciprocal space. K-point sampling can be extended in the DFT calculation to improve the accuracy of estimates in reciprocal space, although this requires more computational resources [70]. Therefore, when starting a simulation, choose a suitable supercell that is large enough to eliminate lateral contact

but not so large as too computationally expensive since calculating a vacuum can be just as costly as calculating atoms. The number of K-points used to represent the Brillouin zone in a periodic system may vary depending on the smearing method used, and the Monkhorst-Pack grid approach is commonly used in the industry. In the thesis being referenced, the Material Studio program was used to determine the appropriate K-points, and the results were satisfactory. However, it's essential to balance the desire for perfect precision with the available computational resources and to choose an appropriate level of K-point sampling that is both accurate and efficient.

2.4.3 The Pseudopotential Approximation

Bloch's Theorem provides a way of using plane waves to describe wavefunctions in a given system. However, in particular systems with high ionic potential, the wavefunctions of valence electrons can fluctuate rapidly and approach the core region [71]. To obtain a high level of accuracy, a large number of plane waves, often exceeding 10,000, are needed to capture the core orbitals that are closely bound accurately. This can lead to computationally expensive calculations due to the large number of computations required. To address this challenge, pseudopotential approximation is often used to reduce computational costs and increase the accuracy of calculations. This method involves replacing the core electrons with a pseudopotential that approximates the core electron behavior, significantly reducing the number of plane waves required for an accurate calculation. This approach has been extensively studied and is commonly used in modern quantum chemical calculations.

The pseudo-wavefunction and all-electron wavefunction are equivalent and have identical potentials when the radius exceeds the designated core cutoff radius r_{cut} [72]. It's important to note that the pseudopotential approximation method minimizes the size of the basis set and

the number of electrons in the calculation while still accounting for relativistic and other effects. This approach has a significant impact on balancing the computational costs and the accuracy of the results, as reducing the number of electrons in the calculation can significantly decrease the computational resources required while still maintaining the accuracy of the results obtained. Therefore, the pseudopotential approximation method is a valuable tool for minimizing computational costs while preserving the accuracy of quantum chemical calculations.

The plane-wave cutoff energy is a crucial factor in DFT calculations and is typically associated with the atoms being studied especially their pseudopotentials. The value of the cutoff energy is determined by the maximum energy required to describe the entire system accurately [73]. To ensure precise calculations, the recommended cutoff energy is 450 eV for electronic static calculations and 380 eV for molecular dynamics simulations, taking into account the available computational resources [74]. This parameter is crucial for achieving accurate results in DFT calculations and is an important consideration when choosing the appropriate method for a given system.

2.4.4 The Projector Augmented Wave Method

The Projector Augmented Wave (PAW) method is a widely used approach in computational materials science and solid-state physics for simulating the electronic structures of atoms, molecules, and solids. It was developed in the 1990s as an extension of the pseudopotential method, which replaces the atomic cores with an effective potential that a small number of basis functions can describe [75].

The PAW method improves upon the pseudopotential method by incorporating an additional set of basis functions that are used to project the proper wave function onto a smaller group of basis functions. This projection is made using a projector operator that maps the actual wave function

onto the auxiliary basis functions. The additional basis functions are then augmented with a set of localized functions that capture the near-core behavior of the wave function. This allows the PAW method to achieve high accuracy in electronic structure calculations while requiring a smaller number of basis functions than other methods.

The PAW method has become a popular tool for studying the properties of materials at the atomic and electronic levels. It has been applied to a wide range of materials, including metals, semiconductors, and insulators. The method has been implemented in many computational packages, such as VASP [75], Quantum ESPRESSO [76], and ABINIT [77], and is widely used by researchers in the field.

One of the advantages of the PAW method is that it provides a smooth transition between the core and valence regions of the electronic structure, which allows for accurate calculations of properties such as ionization energies and electron affinities. Additionally, the PAW method includes relativistic effects, such as spin-orbit coupling, which is vital for studying heavy elements.

2.4.5 Geometry Optimization

Geometry optimization is a computer approach used in computational chemistry and materials science to discover the most stable molecular or solid shape. It entails calculating the forces acting on atoms or ions in a system and manipulating them to minimize the system's potential energy. This procedure is continued until all the atoms' forces are minimized, and a stable configuration is obtained [60]. Typically, the geometry optimization process consists of multiple phases. First, an initial structure is chosen or developed, which is frequently based on experimental evidence or theoretical predictions. The forces acting on the system's atoms or ions are then estimated using quantum mechanical or classical simulation methods. The atoms are

then relocated in a direction that minimizes the system's potential energy, and the forces are recalculated. This procedure is continued until all of the atoms' forces are minimized, and a stable structure is formed. Because the structure of a substance may considerably impact its characteristics, geometry optimization is a crucial technique for investigating the properties of molecules and solids. Geometry optimizations, for example, may be used in drug development to anticipate the most stable conformations of a therapeutic molecule, which might alter its activity and pharmacokinetics. Geometry optimizations can be used in materials research to examine the crystal structure and characteristics of materials, such as their mechanical, electrical, or optical properties.

Chapter 3
Review of Relevant Literature on the effect of defects type on the material's properties

3.1 Engineering the properties of metal oxides.

Semiconductors has the strength of capturing light to drive a chemical reaction such as hydrogen generation from water or converting carbon dioxide into higher energy compounds such as ethanol, therefore research studies have been conducted in that area which called solid-state photo electrochemistry [78]. Since the revolutionary work of Gerischer [79], Fujishima [80], and Honda [81] in the field of photocatalysis, resulting in today's semiconductor becoming a more practical technology.

Recent studies are focusing not just on showing catalytic activity, but also on boosting the effectiveness of conversion to achieve commercially competitive levels and building functional devices [82]. Significant progress in solid-state photo electrochemistry has been made possible by better varying metal oxide structures, such as nano structuring, heterojunction assembly, and more efficient compositions [83]. These improvements were made possible by better control over defect concentration and distribution, which would significantly affect the solid or device properties. Defects may impede electron transmission and serve as recombination spots, negatively impacting electronic properties [84]. While defects in solid-state photo electrochemistry may have negative effects on material properties, they can also have desirable influences. Chemical doping, for instance, can convert an oxide insulator to be working as an excellent catalyst. This process is done by enhancing the concentration of charge carriers and ionizing the

structure point defects. Moreover, controlling electronic band structure and the density of states correlated with the type of defect could engineer and increase the lifetime of charge carriers [85].

Recently, a fast-growing recognition of polarons was for the devices based on the photocatalysis process. As Polarons are confined charges via the deformation of lattice, despite the lack of actual defects of point types [86]. Understanding defect's role and localized carriers that form polarons is essential for enhancing the functionality of solids for a variety of applications, and particularly crucial for mixed photocatalysts [87]. Additionally, the process of reorganizing the bonds between the interface between the solid and liquid is beginning by the effect of light, which in turns needs a manipulation in the dangling bonds to operate. It is worth mentioning that the type of solids is specifying the type and suitability of defects in it. One of the tough challenges that act during the process of making the defects is when a favorite chemical interaction occurs as a result to the desired defect that changes a specific property [88]. The meaning of electronic defect concerns the change in the electronic structure as a result to defects such as hydrogen interstitial that changes the density of charges carriers [89]. Though photocatalysis formed of oxides are dynamic and rapidly advancing field, with promising materials being discovered and new catalytic process (for instance CO_2 reaction and water splitting) in both liquid and gas phases. The main focus is on the photocatalytic process of splitting water into its component parts using light energy, a reaction that is known as photocatalytic water splitting. Through this chapter, I will explain how electronic defects impact the functionality of photo electrocatalytic oxides.

3.1.1 Point Defects

While solid formation, the atoms within the crystal structure are arranged in a specific pattern with a well-defined symmetry. However, the formation of defects is inevitable due to several factors such as impurities, thermal processing, and growth conditions [90, 91]. Volumetric defects, such as pores, are three-dimensional defects that occur when there is an absence of material in a localized region. Planar defects, such as grain boundaries, are two-dimensional defects that occur when there is a misalignment of crystallographic planes. Linear defects, such as dislocations, are one-dimensional defects that occur when there is a misalignment of atoms along a crystallographic plane. Point defects, such as vacancies, are zero-dimensional defects that occur when there is an absence of an atom, or an atom is replaced by another [92].

Point defects are intrinsic in nature and can be present even in a perfect crystal due to thermal vibrations and other factors. Therefore, understanding the formation and behavior of point defects is essential for predicting and controlling the properties of metal oxides [93]. Kröger's work provides a comprehensive sorting for the type of defects in the crystal structure based on different characterization methods [94]. This classification includes defects such as vacancies, interstitials, substitutional impurities, and antistites defects. The characterization techniques used to study these defects include X-ray diffraction, electron microscopy, and spectroscopy [95]. For understanding how defects form, one of the essentials steps is to study the electronic band structure of metal oxides, it may be employed as a foundation for discussing the chemical mechanisms behind defect formation [96]. The electronic band structure is a critical role in their catalytic properties, and defects can alter this electronic structure by introducing localized states in the band gap. This alteration can lead to changes in the reactivity and selectivity of the metal oxide catalyst. Therefore, understanding the formation and behavior of point defects in metal oxides is essential for optimizing their catalytic properties. This requires a combination of

theoretical modeling, experimental characterization, and materials synthesis and processing techniques [97]. By studying the formation and behavior of point defects, it is possible to design and optimize metal oxide catalysts for specific applications, ranging from the production of chemicals and fuels to environmental remediation and energy conversion.

3.1.2 Electronic band structure

One of the most important characteristics is the electronic band structure and band gaps that are affected by several factors related to their crystal structure and bonding characteristics. One important factor is the crystal symmetry of the metal oxide, which determines the allowed energies and wavefunctions of the electrons in the material. The symmetry also affects the strength and directionality of the chemical bonding between the metal and oxygen atoms [98].

Another factor that affects the electronic structure of metal oxides is the degree of ionicity in the metal-oxygen bond [99]. Metal oxides can have either ionic or covalent bonding, depending on the electronegativity difference between the metal and oxygen atoms. The magnitude of the band gap was also altered by the hybridization between the metal and oxygen atoms [100]. In particular, the blending between 2p orbital of an oxygen atom the s orbital of metal can lead to the formation of hybrid orbitals with unique energy levels and wavefunctions influencing the DOS and BS of the structure. Examples on metal oxides with large band gaps due to ionic bonding and orbital mixing include ZnO [101], Ga_2O_3 [102], and Al_2O_3 [103]. ZnO has a 3.4 eV band gap, hence, it is too large for efficient solar energy conversion. Ga_2O_3 has 4.8 eV BG which is considered as a promising material for high-power electronics and UV photodetectors. Al_2O_3 has 8.8 eV BG and is employed as a dielectric material in electronic devices due to its high electrical insulation properties. Transition metal oxides (TMOs) are a class of metal oxides that exhibit unique electronic properties due to the presence of partially filled valence d orbitals in the cation [104].

One example of a TMO with a reduced band gap is Fe_2O_3, which has a band gap of 2.2 eV [105]. The other bonding involving the overlapping between the d and s orbitals in Fe_2O_3 which enables it to enhance the absorption intensity in the visible light region, making it a bright material for the conversion applications in solar energy and photocatalysis. The TMOs electronic structure could be understandable by the crystal-field theory, where the oxygen anions arrangement around a metal cation determines the energy levels and wavefunctions of the metal d orbitals [106]. This crystal-field model could give a useful approximation of the TMOs electronic band structure and is often used to predict their electronic and catalytic properties. The orientation of the d orbitals of a metal center with respect to oxygen anions affects the degree of electron repulsion experienced by the electrons occupying the d orbitals. If the octahedron structure had an elimination to an oxygen atom, that could be said as an oxygen vacancy created, the octahedron structure would become pyramidal resulting a more stabilization in the orbitals of t2g and eg [107].

Ligand field theory extends the crystal field model by considering the intersect between p orbital electron density of oxygen and the d orbitals of the metal [108]. Hence, the case of forming weak π and π* bonding and antibonding respectively. Nevertheless, the overlapping between orbitals among metallic atoms with eg symmetry is interacting toughly with the oxygen orbitals, causing the formation of σ and σ* bonding and antibonding MO is shown in Figure 6(a).

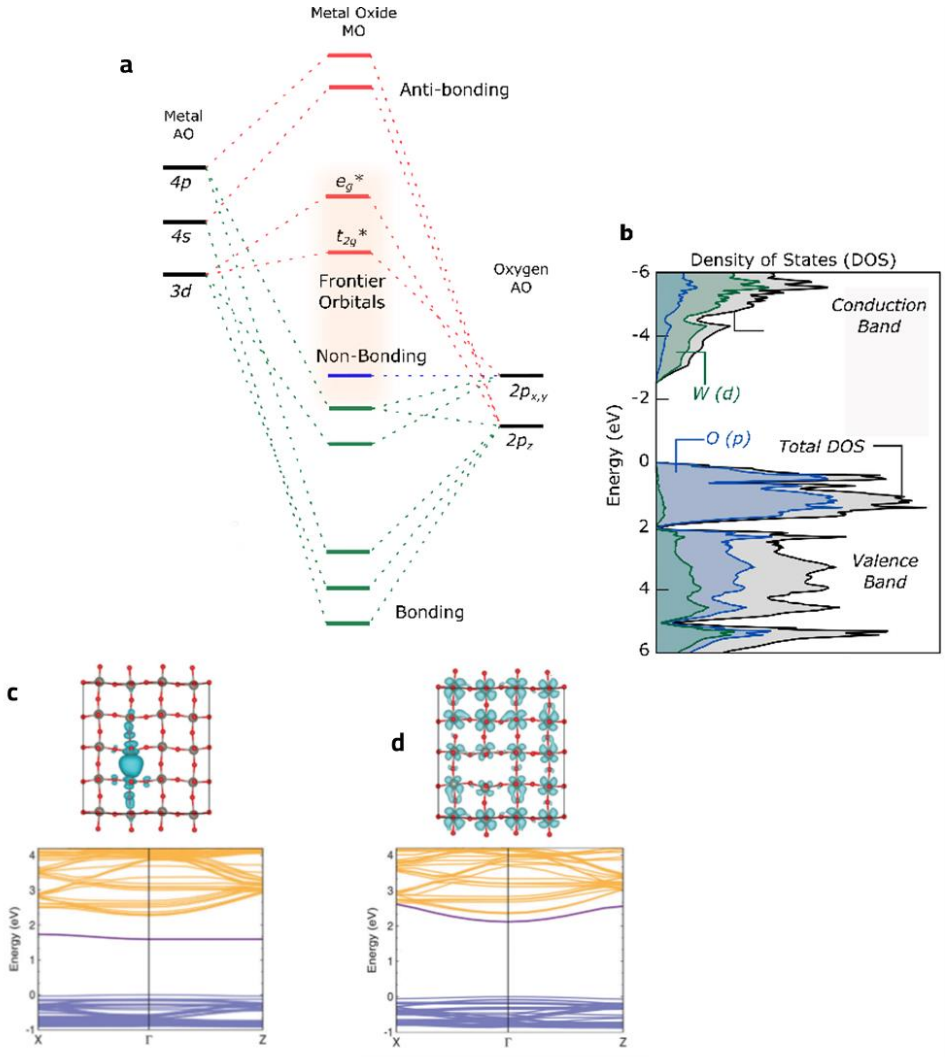

Figure 6: (a) Metal oxides MO diagram. (b) DOS of WO_3 (c) The relation between deep charge density and its band structure (d) The relation between shallow charge density and its band structure [79].

3.1.3 Frontier orbitals.

It is hard to understand the Frontier orbitals that control chemical interactions on crystallographic large scales, as the momentum and band dispersion is complicated in k-space [109]. We may obtain a comparable insight by examining groups of electronic bands, As seen in Figure 6(b) for WO_3, electronic bands are often grouped by the energy for each momentum on different bands, valence and conduction bands and the density of each band is expressed as a density of states (DOS) [110]. The bonding/antibonding character of each of these states play an important role

in defining how the oxide material behaves when supplying or withdrawing electrons, and forming dangling bonds as well. Like molecules, the highest occupied molecular orbital (HOMO) and lowest unoccupied molecular orbital (LUMO) in metal oxides shows a fundamental character in determining their chemical activity and response to the defect formation. Band structure analysis has been shown to be an effective method for explaining physical events and reaction patterns of oxides [111]. Increasing the degree of electronegativity of a metallic cation (higher oxidation state and fewer d electrons) sets the d states of valence band nearer to the energy of the oxygen 2p levels, boosting a hybridization between the p orbital in oxygen and d in the metal. If the orbitals found in the valence band of a metal have equal energy as O 2p orbital, the HOMO bands would be occupied, likely seen in orbital d^{10} in Cu_2O [112]. The electronic band structure in metal oxides can have significant impacts to the construction of point defects, polarons as localized charges, also ultimately in photocatalytic yields. For example, in TiO_2 [113], the d^0 conduction band can become filled with excess electrons, preceding to the founding charges, subject on the structure of the crystal. This can create point defects that these defected sites could trap the charge, causing localized polarons formation, that can significantly adjust the photocatalytic characteristics of TiO_2, affecting its efficiency in processes such as water splitting or pollutant degradation.

3.1.4 Point defects thermodynamics

Point defects are structural imperfections in a crystal lattice that can notably affect the characteristics of materials. Point defects could be classified to two main classes: intrinsic and extrinsic. Intrinsic defects occur naturally in a crystal and involve the absence of an atom out of the crystal site (vacancy), in other words, the presence of an atom in an empty position (interstitial). Intrinsic defects can form due to thermal fluctuations or irradiation damage. On the

other hand, extrinsic defects are introduced intentionally or unintentionally into the crystal lattice. For instance, impurities can be unintentionally incorporated into a crystal during growth or processing. Alternatively, materials can be intentionally doped with specific impurities to alter their electrical properties. Extrinsic defects could have a profound effect over the material's characteristics, and their behavior can be predicted based on the concentration and type of dopants. Apart from the above two types, polarons are another type of electronic defect that can be considered. Polarons are trapped electrons, which are formed due to the coupling between electrons and lattice vibrations. These trapped electrons can create localized charge carriers, which can have a significant influence on the material's electronic properties.

The most accurate method to provide valuable insights on the defect's concentration in the crystal is thermodynamic analysis [114]. A perfect crystal has a configurational entropy (ΔS) of zero, which means all atoms arranged correctly in their sites. However, the introduction of point defects increases the number of possible configurations and raises the entropy of the system [115]. This increase in entropy can be quantified by the configurational entropy difference (ΔS) in case of forming a defect. The formula of the total Gibbs free energy change (ΔG) for a defect formation is expressed as $\Delta G = \Delta H - T\Delta S$, where ΔH, T are the enthalpy change and temperature respectively. The enthalpy change represents the energy required to create or destroy a defect, while the configurational entropy accounts for the increase in the number of possible configurations. The temperature also has an important role in deciding the defect concentration, as higher temperatures lead to higher entropies and a greater tendency for defects to form [116]. The statistical distribution for the equilibrium concentration of defects species is represented by the Boltzmann distribution, which is proportional to the exponential of the negative Gibbs free energy change divided by the thermal energy (kBT). This equation describes the probability of a defect forming at a given temperature, and it can be used to predict the concentration of a specific

defect species. The concentration of a defect species is determined by its formation energy (ΔH_f) [117] and its entropy of formation (ΔS_f) [118], as well as the temperature and the chemical potential of the species involved [119]. By calculating the formation energies of different defects, it is possible to predict which types of defects are most likely to form under different conditions and how their concentrations may vary with temperature and other factors.

As the temperature of a crystal rises, the contribution of entropy to the free energy increases, which leads to an increase in the concentration of defects. Defects can have various effects on the crystal's properties, including electronic, optical, and mechanical properties. For example, the presence of oxygen vacancies in a metal oxide can alter its photocatalytic activity by creating localized charge carriers and changing the band structure [120]. This change can lead to improved efficiency in energy conversion and storage devices. Similarly, dislocations and filling defects in a crystal can affect its mechanical properties by providing preferential sites for deformation and fracture [121]. These defects can cause changes in the crystal's strength, ductility, and fracture toughness. It is, therefore, essential to understand the formation and concentration of defects in a crystal to predict and control its properties. This requires a combination of theoretical modeling and experimental characterization techniques, such as density functional theory (DFT), X-ray diffraction (XRD), and scanning transmission electron microscopy (STEM). These methods can provide valuable information about the structure, composition, and behavior of defects in a crystal, enabling the design and optimization of materials with specific properties for various applications.

3.1.5 Tailoring electronic band structure

Electronically speaking, defect formation in a metal oxide can result in changes to its electroneutrality conditions. In an ideal stoichiometric material, filled valence band, and empty conduction band, with a large band gap enough to prevent electron and hole charge carrier thermal excitations [122]. However, introducing electron or hole defects creates in the band gap new energy bands. The needed energy to exchange between electrons and holes in the band structure is significantly affecting the position of those inserted sub-bands. Just like an oxygen vacancy (V_o^+) could be ionized for adding electrons to the conduction band, as shown in the defect equation below. The position of the sub-band gap defect levels determines the ease with which this process can occur. The needed energy to transfer electrons and holes between the bands could have a notable influence on the material's electronic and optical properties.

$$V_o^+ \rightarrow V_o^{2+} + e^-$$

or by hole removal out of the valence band, it might end up at the identical ultimate charge state:

$$V_o^+ + h^+ \rightarrow V_o^{2+}$$

This energy difference, denoted as ΔE, is of critical importance for optimizing energy conversion systems since it decides whether the defect will have a positive or negative effect on the material's electronic properties.

One of the vital factors to explain the behavior of materials under defects is to specify ionization levels positions in the semiconductor band gap [123]. There are two cases to consider when assessing the energy of a defect in a semiconductor crystal. The first is a shallow state, which occurs when a defective band level is approaching the band edge, typically at room temperature within k_{BT} ~ 26 meV. Similarly, defect level could be thermally ionized, which could have a significant effect on the electronic properties of materials. Shallow states in a material are typically linked to a defect wavefunction that spreads over a significant number of unit cells,

ranging from tens to thousands. When considering a charged defect in a dielectric host, the energy of a shallow state can be determined by the effective mass and dielectric constant of the host, based on the hydrogenic limit. This relationship is expressed in atomic units and can be used to optimize the energy conversion efficiency of semiconductor devices:

$$\Delta E = \frac{m^*}{2\varepsilon^2} \qquad (25)$$

In tetrahedral semiconductors like silicon [124] and zinc oxide [125], the needed energy for ionization of defects ranging between 1-50 meV, which is relatively low. As a result, shallow states are common in these materials, where the defect level is positioned in close proximity to the band edge and has the potential to be ionized thermally. Shallow states can rise the free carrier's concentration in the bands, leading to an increase in the material's electrical conductivity.

On the other hand, deep states refer to defects where the energy required for ionization of the defect is greater than the thermal energy, and the defect wavefunction is confined to one or a few atoms in space. Deep states in a material are typically created as a result of a substantial chemical alteration in the crystal structure, like the formation of a vacancy or the substitution of an element with a significantly different size orbital. These types of defects are frequently linked to significant structural deformations and can have a notable effect on the electronic and optical characteristics of the material [124, 125, 126].

The presence of deep states can limit the material's electrical conductivity by trapping charge carriers and reducing their mobility, leading to reduced device performance. Deep states can play a key role in the charge carrier entrapment in optoelectronic and photocatalytic devices. They can also restrict the range of energy levels available to the Fermi level, affecting the device's performance. There are two kinds of defect levels to think about: optical and thermal. Optical levels correspond to a fast vertical excitation under the Franck-Condon principle, with the defect

geometry remaining constant. Thermal levels, on the other hand, require a slower process in which the fault shape might alter over time. Capacitive techniques, like deep-level transient spectroscopy, can be employed to investigate these thermal energy levels. The position of the defect states within the band gap can be explained by examining the frontier orbitals of the parent crystal. When a defect is formed, such as an oxygen vacancy, it generates an empty space in the lattice that has unpaired electrons on the neighboring metal atoms. These unpaired electrons, or dangling bonds, have an energy level that is comparable to that of the metal atomic orbitals. If these bonds are situated in close proximity to the band edges or within the bands themselves, they can result in the formation of shallow defect states [127].

Low hybridization among the hanging metal atoms, aided by a high metal-metal distance and a poor interaction structure at the defect location, can also favour the creation of shallow defects. When an oxygen atom is removed from the WO_3 lattice, it results in an oxygen vacancy and two unpaired tungsten atoms that have dangling bonds, each of the tungsten atoms with the dangling bonds acquires an additional electron, resulting in a decrease in the oxidation state from W^{+6} to W^{+5}. The presence of the dangling bonds creates a situation where there is a doubly filled energy level through material's band gap.

Nonetheless, length of bond should be relaxed near crystal vacancy to lower the risk of repulsion that shortens the distance between tungsten and brings the level of defects close within the CB, making carrier injection easier. Optical energy levels in a material are typically positioned deeper within the band gap than thermal energy levels by a factor equal to the energy of structure relaxation of the specific defect species. This is due to the fact that thermal levels entail a longer process in which the defect geometry might vary over time, whereas optical levels relate to a quick vertical excitation in which the defect geometry remains constant [128].

In some cases, when an electric charge is confined in the vicinity of a vacancy, it can lead to the creation of a deep defect level within the material as shown in Figure 6(c). If there is no significant structural deformation, the charge can spread out over adjacent sites, leading to the formation of a shallow defect level instead of a deep one, as illustrated in Figure 6(d). If there is significant overlap between the wavefunction of the defect and the density of states in the material, the defect is said to be resonant with the band [129]. The formation of a point defect in a crystal can result in the addition of extra charge in the form of either electrons or holes. For instance, doping Fe_2O_3 [130] with Ti or Sn or $BiVO_4$ [131] with W can elevate the number of electrons in the host material, and can strengthen the n-type behavior of the material. Defects can lead to modifications in the crystal structure that allow for the inclusion of dopant atoms, but the additional electronic charge can also create a lattice distortion in the material. When excess charge is introduced into a highly polarizable solid, the excess charge could decrease its energy by causing the neighboring atoms to move via electron-phonon interactions. this creates a quasi-particle called a polaron that can generate an energy level within the band gap. If the additional charge and its associated structural alteration are strongly attached to another imperfection or irregularity in the material's crystal lattice, like vacancy, the polaron can alter the properties of the defect level. For instance, electron polarons in $BiVO_4$ localized in V centers can change the oxidation number from V^{+5} to V^{+4} and bond between Vanadium and Oxygen by approximately 0.1 Å. However, inducing such a structural deformation may necessitate an input of activation energy. The formation of a polaron is important because it can significantly alter the material's optical and electronic properties. Polarons can introduce an energy band through the band gap, modify the level of defects, and affect material's transport properties. Therefore, understanding the formation and behavior of polarons is crucial for optimizing the performance of electronic and optoelectronic devices. Polarons near a defect, such as a vacancy, can exist in different

configurations, which can make it challenging to analyze the properties of the localized state in both the volume and on the surface of $BiVO_4$. The formation of a polaron occurs due to a trade-off between the potential energy increase achieved through the structural deformation and the kinetic energy reduction due to carrier confinement. The overall energy of the excess charge in a dielectric medium can be minimized to yield the polaron binding energy [132], as shown in the following equation:

$$E_{PBE} = E_{bulk} + E_{polaron} - E_{defect} - E_{free}$$

where E_{PBE} is the polaron binding energy, E_{bulk} is the energy of the bulk material, $E_{polaron}$ is the energy of the polaron, E_{defect} is the energy of the defect, and E_{free} is the energy of the free electron or hole. Understanding the polaron binding energy is crucial for optimizing the performance of optoelectronic devices, as it determines the stability and mobility of the polarons within the material. Additionally, the different configurations of polarons near a defect can affect the localization and transport of charge carriers, further complicating the characterization of the localized state:

$$E_P = \frac{1}{4\pi^2} \frac{m^* e^4}{2\hbar^2 \varepsilon_{eff}^2} \qquad (26)$$

Where; $m^*, and\ e$ are the effective mass, and electronic charge whilt ε_{eff} value could be obtained by the reciprocals of static and dielectric constants as follows:

$$\frac{1}{\varepsilon_{eff}} = \frac{1}{\varepsilon_\infty} - \frac{1}{\varepsilon_o} \qquad (27)$$

The polaron binding energy refers to the amount of energy necessary to stabilize a polaron state in comparison to an unaccompanied valence band hole or conduction band electron. At the microscopic level, the creation of polarons is determined by the interaction between charge carriers and vibrational modes. The coupling strength, F, is determined using the Landau-Pekar model [133], that counts the traits of the longitudinal optical phonon frequency (o). Hence, that

model is a theoretical framework used to understand electron-phonon interactions in polar materials. It describes the polaron as a self-trapped excitation in a dielectric medium that is coupled to lattice vibrations.

The coupling strength, F, is related to the polaronic mass and the effective dielectric constant of the medium. It is crucial to comprehend the level of interaction between charge carriers and vibrational modes for predicting polarons' formation and in materials. The formation of polarons can significantly affect a material's transport properties, which can have implications on the development of electronic and optoelectronic devices. There are two types of polarons, which are categorized based on the degree of interaction between electrons and phonons and the amount of structural deformation they induce. Fröhlich polarons [134] or large polarons, have a weak coupling between electrons and phonons, and their structural distortions extend over more than one unit cell. They are characterized by a broad wavefunction that extends over many lattice sites, leading to a long polaronic tail. Large polarons are typically found in materials with low dielectric constants and/or low carrier concentrations. Small polarons, also known as Holstein polarons [135], have a strong coupling between electrons and phonons, and their structural distortions extend over less than one unit cell. They are characterized by a localized wavefunction that is confined to a few lattice sites. Small polarons are typically found in materials with high dielectric constants and/or high carrier concentrations. The distinction between large and small polarons is important for understanding their behavior in materials. Large polarons are more mobile and can contribute to the electrical conductivity of a material, while small polarons are less mobile and can contribute to trapping and recombination processes [136]. The type of polaron that is formed depends on the specific material and the conditions under which it is formed. The formation of polarons is usually encouraged in materials with high dielectric constants and effective carrier masses. The possibility of polaron formation is influenced by the electronic

structure of the material. When the atomic orbitals of a material overlap weakly, it results electronic bands that are weakly dispersive and carriers with significant effective masses. This favors carriers' localization and thus encourages creation of polarons.

The electronic structure of numerous metal oxides is often distinguished by a high density of states near the band edges and orbitals with weak interaction. This type of electrical structure is common in transition metal oxides and is often associated with polaron formation. Understanding the electrical structure of a material is important for predicting the likelihood of polaron formation and for optimizing the performance of electronic and optoelectronic devices [133]. By designing materials with specific electrical properties, researchers can tailor the formation and behavior of polarons to suit their needs. TiO_2 is a well-studied photocatalytic system, and electron paramagnetic resonance (EPR) investigations have shown that localized states of electrons, in the form of Ti^{+3} $3d^1$ ions, exist in TiO_2. Interestingly, the generation of polarons in TiO_2 is dependent on its polymorph.

Rutile TiO2 is recognized for producing minimal electron polarons, while anatase TiO_2 generates main electron polarons that possess narrow states situated under the conduction band. This variation in polaron production helps explain why anatase and rutile behave differently in optoelectronic applications. The difference in polaron generation between anatase and rutile TiO_2 is significant because it affects their optoelectronic properties. Anatase TiO_2, which produces large electron polarons, has a higher charge carrier mobility and a longer electron lifetime, making it a better candidate for applications requiring efficient charge carrier separation and transport. Rutile TiO_2, on the other hand, produces small electron polarons, which can lead to greater recombination of charge carriers, reducing its efficiency in optoelectronic applications [137]. Polarons have been found to have an impact on various oxides used in different applications such as photocatalysts, electrocatalysts, or co-catalysts. These oxides include WO_3, $BiVO_4$, iron oxides,

Co_3O_4, and titanates. Polarons can be generated in these materials by light, and the creation of polarons by injecting charges of the induced light into a semiconductor can also stimulate this phenomenon. Photo-induced polarons could be generated indirectly by injecting electrons from a surface-sensitized dye molecule, or directly via band gap excitation that creates electrons and holes. These photo-induced polarons can affect the material's optoelectronic properties, such as its charge carrier mobility and lifetime, and ultimately impact its performance in various applications. Understanding the formation and behavior of polarons in these materials is important for optimizing their performance in different applications [137]. By controlling the generation and behavior of polarons, researchers can design materials with specific optoelectronic properties, leading to improved device performance.

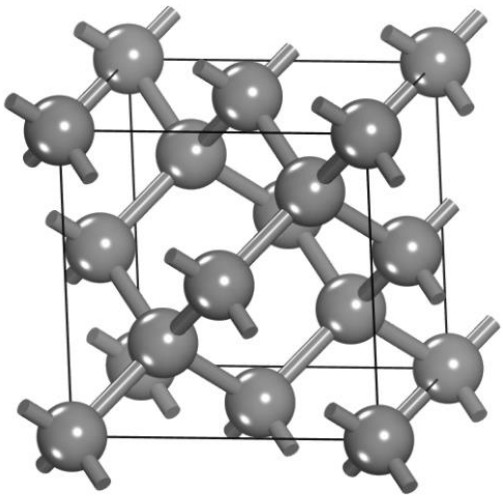

Figure 7: Diamond crystal structure

3.2 Engineering the properties of Diamond.

Diamond is a material made entirely of carbon, which is the sixth element in the periodic table. Carbon's ground state electronic configuration is $1s^2\,2s^2\,2p^2$. In diamond, the valence electrons in the second shell of carbon ($2s^2\,2p^2$) hybridize to form sp3 orbitals. These sp3 orbitals create four strong bonds that are tetrahedrally arranged, with a bond length of 1.54 Angstroms and bond angles of 109.47 degrees.

The diamond structure has a face-centered cubic (FCC) crystal structure, with a basis of two atoms, meaning each carbon atom is bonded to four neighboring carbon atoms, forming a tetrahedral arrangement Figure 7. This strong covalent bonding results in diamond's exceptional hardness. Despite being one of the hardest minerals, diamond is less stable than graphite at normal temperature and pressure. Carbon's most common allotrope is graphite, which is sp2 hybridized. Diamond is kinetically stable under air circumstances, whereas graphite is thermodynamically stable. Despite graphite's thermodynamic stability, diamonds are nevertheless produced naturally because they develop under favorable circumstances in the Earth's mantle.

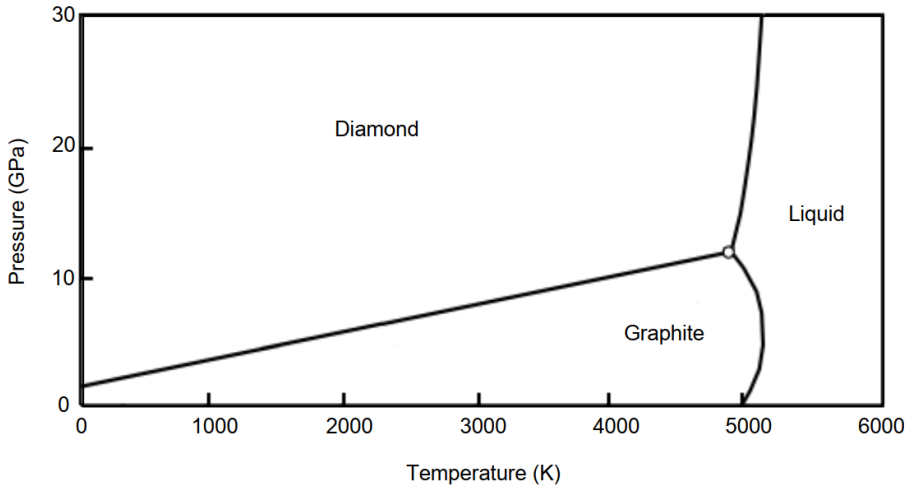

Figure 8: Phase diagram of carbon for its allotropes Diamond and Graphite. [61]

At standard circumstances, the conversion barrier is quite high once produced, implying that carbon is trapped in the diamond form. As a result, even at normal temperature and pressure, diamonds stay stable and are not transformed back into graphite [138]. Figure 8 shows the conditions under which diamond can form under equilibrium, as a function of pressure and temperature. It provides a graphical representation of the diamond stability field, which indicates the range of conditions where diamond is more thermodynamically stable than graphite or other forms of carbon. The graph shows that diamond formation is favored at higher pressures and lower temperatures, consistent with the natural formation of diamonds deep within the Earth's mantle.

3.2.1 Defects in diamond

Defects in crystals can be classified as either extended or point defects, and they can arise from either intrinsic or extrinsic sources. Extended defects are characterized by their dimensional nature, meaning they extend into the crystal lattice. Linear defects called dislocations arise due to lattice mismatch, voids can result from the removal of several atoms, leaving empty spaces within the crystal, and grain boundaries are observed in polycrystalline materials where each grain is a single crystal with a different orientation to its neighbors [139]. The boundary can be represented as an edge dislocation if the misorientation between two grains is not significant. Understanding the types of defects that can occur in diamond is crucial for optimizing its performance and designing new materials with specific properties. Crystal defects are imperfections or irregularities that occur in the crystal lattice structure of diamond [140]. There are three main types of crystal defects: substitutional, interstitial, and vacancy defects. A substitutional defect occurs when an impurity atom takes the place of a host atom at a lattice site. This can happen when the impurity atom is a different size or has a different charge than the host atom, leading to a distortion in the crystal

lattice. An interstitial defect occurs when an impurity atom is located in a space between lattice sites, rather than occupying a lattice site itself. This can also cause a distortion in the lattice structure [141]. A vacancy defect occurs when a host atom is missing from its lattice site, leaving a hole or "vacancy" in the crystal lattice. This can happen due to thermal or radiation-induced diffusion, or because of defects introduced during crystal growth or processing. Diamonds can contain defects in their crystal lattice structure that can affect their properties. These defects can be introduced during the growth of the diamond, whether through intentional doping or accidentally during the manufacturing process. Natural and synthetic diamonds can also undergo radiation and heat treatments to alter these defects. Even in very small concentrations, as low as parts per billion, point defects can significantly affect the properties of diamonds [142]. Some of these defects can cause the diamond to exhibit certain colors, which are highly valued in the gemstone market. Specific elements or defects are linked to specific colorations, and the presence of these point defects can be visually detected even at low concentrations. The insertion of particular materials or defects in the crystal lattice structure of a diamond can result in distinct colors. For example, nitrogen inclusion can produce canary yellow diamonds, but boron inclusion can produce rare natural blue diamond's [143]. The existence of vacancy clusters and plastic deformation, on the other hand, might result in a less desired brown color. Because nitrogen is comparable in size to carbon, plentiful in nature, and easily accessible throughout the diamond formation process, it is the most common defect identified in diamonds. As a result, nitrogen is employed as the foundation for the diamond categorization system explained in the next section.

3.2.2 Modeling of doping characteristics

To fully comprehend the electronic properties resulted from crystal doping, a quantum-mechanical technique is typically required. These techniques take into account the quantum nature of both the electrons and nuclei in the material, and there are various levels of complexity within the field of quantum chemistry. These methods are necessary because classical approaches are not able to accurately describe the behavior of these quantum systems [144].

Nevertheless, it is critical to understand the foundation underlying the computed characteristics. To give context for appraising the predictions presented in this analysis, we explain the most commonly utilized band-structure approaches. The common strategies for estimating the level of donors and acceptors are then discussed. However, the description of atom groups is now being carried out using a variety of quantum-mechanical computational frameworks. There exist several quantum-chemical techniques for modeling the properties of atoms sets, including the tight-binding limit, that is applicable to large collections of atoms, but lacks rigorous accuracy, and more exact first principles Hartree-Fock methods, which are highly accurate but computationally intensive [145]. There are many techniques that rely on density functional theory to solve problems in different domains that fall in between these two extremes. While there are several works that cover the essentials of these methods, the paper does not provide an in-depth explanation of them. However, it is worth noting that DFT is currently a widely used method for simulating the quantum calculations of solid states [146]. DFT approaches are a type of theoretical method used to understand the properties of materials. To achieve this, the charge density is expressed in terms of one-particle-like functions and energies, referred to as Kohn-Sham levels and states.

3.2.3 Interpretation of band-structures

To understand the acceptors and donors level's position in relation to the HOMO and LUMO, it is essential to interpret the band structure accurately. This interpretation often depends on the Kohn-Sham equation solutions of eigen values and functions, which are usually perceived as a one-electron system representation, similar to the HF method, in which they constructed one-electron states [146]. Therefore, the understanding of these mathematical solutions is crucial for predicting and interpreting the electronic properties of materials and their behavior in electronic devices. Although interpreting Kohn-Sham spectra in terms of one-electron functions and energies is theoretically incorrect, it can still provide useful information about the electronic structure of a group of atoms. However, it is important to use caution when doing so. Understanding the HOMO and LUMO of Kohn-Sham orbitals can be particularly useful in understanding donor or acceptor characteristics. Janak's theorem provides support for this connection by linking the ionization energy of a system to the energy of its highest occupied Kohn-Sham level [147].

However, the electrons affinity method is not able to accurately identify the lowest empty state, but a a lot of facts could be generated from an empty Kohn-Sham levels. However, there are concerns when using band structures of Kohn-Sham for quantitatively investigating the levels of donors and acceptor. The primary concerns with this method are the imprecisions in determining the bandgap energy and the vertical orientation of the transitions. For example, in many materials with negative-U interstitial hydrogen systems [147], the neutral charge state is inherently unstable and only exists in a metastable state. One of the issues during the use of Kohn-Sham band-structures is that they tend to substantially underestimate the bandgap energy, which raises questions about which edge of band should set the level reference to, or whether the energy values must be modified in a certain manner to align with experimental findings. Despite these

challenges, the placement of Kohn-Sham orbitals within the bandgap can be used to predict whether a defect would result in changing in the valence and conduction bands [148].

3.2.4 Substitutional boron

Boron typically appears in a solitary substitutional form (BS), either at or on a host site, which causes slight dilation of the surrounding lattice. The energy necessary to activate a hole that is confined to a bound state into the valence band has been measured computationally to be 0.37 eV. The existence of uncharged boron atoms that replace carbon atoms in diamond can induce infrared electronic transitions, leading to noticeable spikes at 2450 cm^{-1} and 2820 cm^{-1}, which correspond to energies of 304 and 350 meV, respectively. This optical property It can be utilized to track the levels of neutral acceptors, for example, in investigations that involve hydrogen passivation. It is worth noting that in one theoretical study, the electronic transition associated with neutral substitutional boron has been incorrectly linked to transitions involving hydrogen-boron pairs. The activation energy required for conduction reduces as the concentration of BS rises, and at a concentration of around 5×10^{20} cm^{-3}, the semiconductor material converts to metal [148, 149].

The illustration in Figure 1 presents two conceivable pathways that could give rise to this effect. One possible explanation involves the emergence of an impurity band in the bandgap of the diamond material, as a consequence, there is a nonzero amount of available states at the Fermi level shown in Fig. 1(a). Second scenario suggests the presence of boron-linked hole states situated below the VBM, with the conduction path located within a host band that has been depleted [150]. It is important to note that there are several scenarios that fall between these two limiting cases, with a boron-related impurity band being made up of a blend between the VBM and states originating from the boron acceptors. (Fig. 1(b)).

Both limiting cases have some experimental support. The impurity band concept has been offered as a theoretical explanation for cathodoluminescence spectra, although X-ray angle-resolved photoemission spectroscopy seems to show that below the host valence band will be existing the Fermi level line. A large percentage of the computer study appears to support the latter conclusion. Boron-doped materials exhibit metallic conduction and are capable of superconductivity at low temperatures. This subject has been covered elsewhere and will not be examined in depth here.

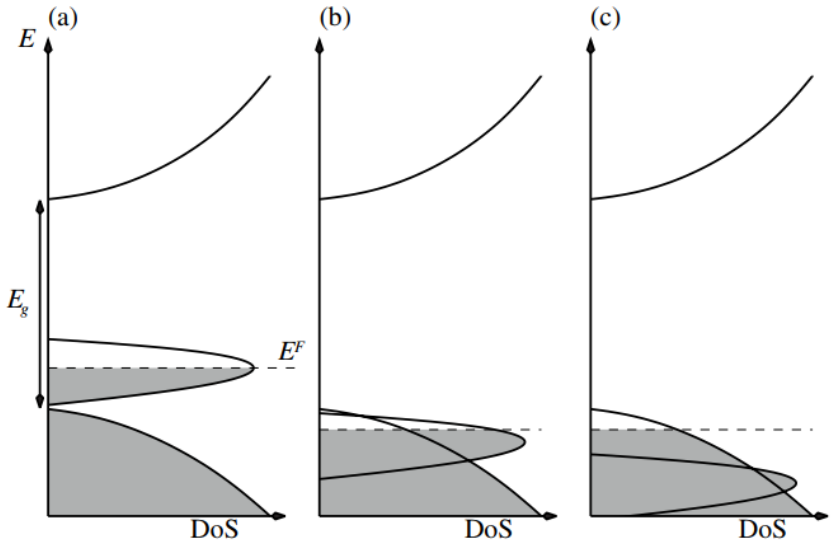

Figure 9: Total DOS of a diamond doped with Boron (a) Boron doping involves producing a band that passes through the real diamond band. (b) the band is on the HOMO. (c) Overlapping between the doped band and HOMO [150]

Supercell simulations have been employed to investigate how boron doping affects the lattice constant of metallic diamond. The studies discovered that in materials with high concentrations of boron, the reduction of orbital states results in a nonlinear shift in the lattice parameter in relation to the amount of boron present. This means that as the concentration of boron increases, the lattice expansion becomes increasingly nonlinear [151]. Interestingly, to explain the data observed, it does not require the inclusion of theoretically high-energy interstitial boron dopants. It is suggesting that the depletion of bonding states is the primary mechanism

underlying the observed lattice expansion. These results provide significant understandings into the impact of doping boron on the structural characteristics of metallic diamond and could develop implications for the development of new materials that incorporate boron doping.

3.2.5 Interstitial dopants

One of the potential methods to create n-type conductivity in diamond is by introducing mono-valent interstitial dopants, specifically alkali metals such as lithium and sodium [152]. Theoretical simulations suggest that these dopants can create shallow donor levels in the T-site of the diamond lattice, with donor levels relative to the conduction band minimum with an average of 0.25 eV for Lithium and 0.3 eV for Sodium. Experimental methods depending on doping lithium have been successfully estimated and measured electrical activation energies are similar to the calculated values for Lithium [153]. However, caution must be exercised when interpreting these results, as further investigation is needed to confirm that the conduction is taking place through lithium that has been dissolved within the diamond crystal structure. The conductivity of diamond can be enhanced by introducing impurities, such as lithium, into its crystal lattice. However, the exact mechanisms that generate conduction electrons in these doped materials are not well understood. The energy needed to initiate conduction is not conclusively associated with a mechanism, but it may result from the introduction of lithium into the diamond lattice, which can cause lattice damage in some cases.

It is important to consider the approaches used to dope diamond structure, as this can significantly affect the material's electrical conductivity. For instance, lithium can be introduced into diamond through a range of methods, including ion implantation, in-diffusion, and during growth. Each of these methods can yield different levels of success in terms of conductivity. Ion implantation, for example, is a common method for introducing lithium into diamond, which

often results in n-type material [154]. However, annealing the material at a relatively low temperature of 600°C can significantly reduce its conductive properties. This reduction in conductivity may be due to the passivation of lithium donors through the creation of a complex through interaction with residual damage in the lattice structure. This is due to the fact that self-interstitials start to become mobile above a temperature of approximately 400°C, while neutral vacancies become mobile at around 600°C, which corresponds to the activation energies range of 16.8 ± 0.15 eV for interstitials and 2.4 ± 0.3 eV for vacancies, respectively. Despite these observations, the donor's actual identity in the n-type diamond that has been implanted with lithium remains unclear and uncertain, and further research is necessary to gain a complete understanding of the mechanisms that lead to conduction electrons generation in these materials.

In simpler terms, the conductivity in Li-doped diamond may be a result of implantation damage rather than the presence of lithium. Nuclear techniques show that only a small percentage of the doped Li would be formed as an interstitial dopant or a substituted dopant through the crystal. The existence of lithium atoms that substitute for other atoms in the crystal lattice is significant since they can function as deep acceptors leading to self-compensation. If lithium is diffused inward or added to diamond using a lithium source, the resulting material is typically classified as an insulator. There are indications that the deactivation of possible lithium interstitial donors may be caused by impurity clusters forming within the material. While photo-thermal defect spectroscopy and photo-conductivity assessments demonstrate the existence of energy levels within the bandgap of diamond that has been doped with lithium causing absorption enhancement. The exact relationship between these features and the presence of lithium point defects or clusters of lithium atoms is not clear how it affects it.

In general, there is an absence of a definite comprehension of the atomic mechanisms that are stimulated by the diverse measured quantities, and additional research is required to acquire

a complete understanding of the behavior of diamond that has been doped with lithium. To put it more simply, attributing optical and electrical properties to lithium in diamond is challenging because it is commonly found a blend between lithium and other impurities such as boron or oxygen, which can have a different electronic structure than isolated lithium. Compared to diamond doped with lithium, there is significantly less experimental information available for diamond that has been doped with sodium. The interstitial defect of sodium atom is a potential dopant for creating n-type diamond, but compared to lithium it has a higher level of dopants. Recent computations exploring the possibility of using lithium as an n-type dopant have produced unfavorable results, primarily due to two characteristics of lithium when present in diamond. First, the ability of the interstitial lithium atom to move within the diamond's crystal structure is restricted. Secondly, A variety of clusters can develop, either electrically inert or operating as acceptors, that may neutralize the dispersed donors within the material. Recent simulations using density functional calculations estimated activation energy of interstitial lithium neutral donor movement to be around 1.09 - 1.2 eV, which is around 30-40% higher than previous estimates using smaller supercells [155].

Chapter 4
Computational methods

4.1 Computational Methods of Untapped Potential of Zn-Enriched Cupric Oxide Photocathodes for Stable and Durable Green Hydrogen Generation via Photoelectrochemical Water Splitting

Computational calculations were conducted for 95Cu-5Zn sample. All calculations were based on a spin-polarized density functional theory (DFT) and were performed using the standard Cambridge Serial Total Energy Package (CASTEP), as implemented in Materials Studio 2017 [156]. Generalized gradient approximation (GGA) and the Perdew-Burke-Ernzerhof (PBE) exchange-correlation functional were used for geometry optimization, electronic property calculation, and adsorption energy computation [157].

The interaction between electrons and ions was represented using an OTFG ultrasoft pseudopotential, where the Broyden-Fletcher-Goldfarb-Shanno (BFGS) algorithm was utilized with a cutoff energy of 630 eV and a separation distance of 0.07 Aº for the K-points. Convergence was ensured by relaxing the bulk structure of CuZnO, until it met the convergence criteria of less than 5.0×10^{-6} eV/atom, 0.01 eV/ Aº, 0.02 GPa, and 5.0×10^{-4} Aº for the energy, force, stress, and displacement, respectively [158]. The optimized lattice constants for the bulk CuZnO were determined to be a=7.21 Aº, b=5.38 Aº, c=9.63 Aº, $\alpha = \gamma = 90^{o}$, and $\beta = 89.81^{o}$, providing valuable insights into the structure of the material. The bulk structure is shown in Figure 10.

For the step of geometry optimization of pristine CuO, we used the CuO structure stored in Material's studio data base. To compare the accuracy and efficiency of the particular structure and computational setup, the positions of atoms and lattice parameters of CuO were obtained from a previously published work by Burak et al. [159]. The values of the CuO atomic coordinates and lattice parameters, obtained from a previous study, were compared to those reported in other literature to assess the accuracy of the current methodology. The comparison indicated that the

obtained values were consistent with those reported in other sources. Hence, we performed structural relaxations and calculated the energy bandgap, which was found to be in agreement with both experimental and theoretical values previously reported, with a value of Eg = 1.21 eV.

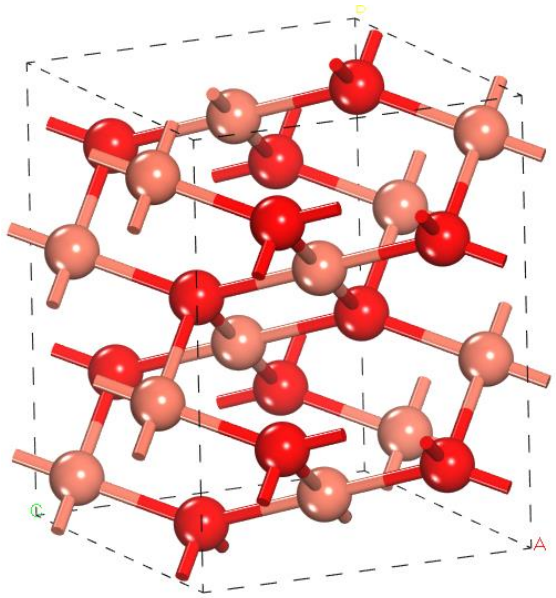

Figure 10: Bulk structure of Pure CuO

After building the bulk structure of CuO, we doped it with Zn atoms to get the ratio of (95%Cu and 5%Zn) as shown in Figure 11(a). The Kroger Vinck notation for the doped structure is given by the following equation:

$$CuO + Zn_{Cu^{+2}} -> Cu_{Zn^{+2}} + O_v$$

To obtain a more accurate electronic band structure diagram, DFT+U calculations were performed to avoid the self-interaction error that often leads to a significant underestimation of the band gap. A Hubbard correction value of 9 eV was set for Cu's d orbitals, a band gap of 1.445 eV, which closely matches the actual experimental band gap of 1.42 eV. The results emphasize the significance of utilizing precise computational methods when analyzing electronic properties, particularly when dealing with materials that exhibit complex electronic behavior. Given that the

facet (-1 1 1) is the most favorable face for the hydrogen evolution reaction, which is the dominant facet in our material, a cleaved surface of (-1 1 1) was utilized to build a bulk crystal with a vacuum slap of 15 A⁰ as shown in Figure 11(b).

This approach prevented interaction between the periodic layers and allowed for an accurate analysis of the material's electronic properties.

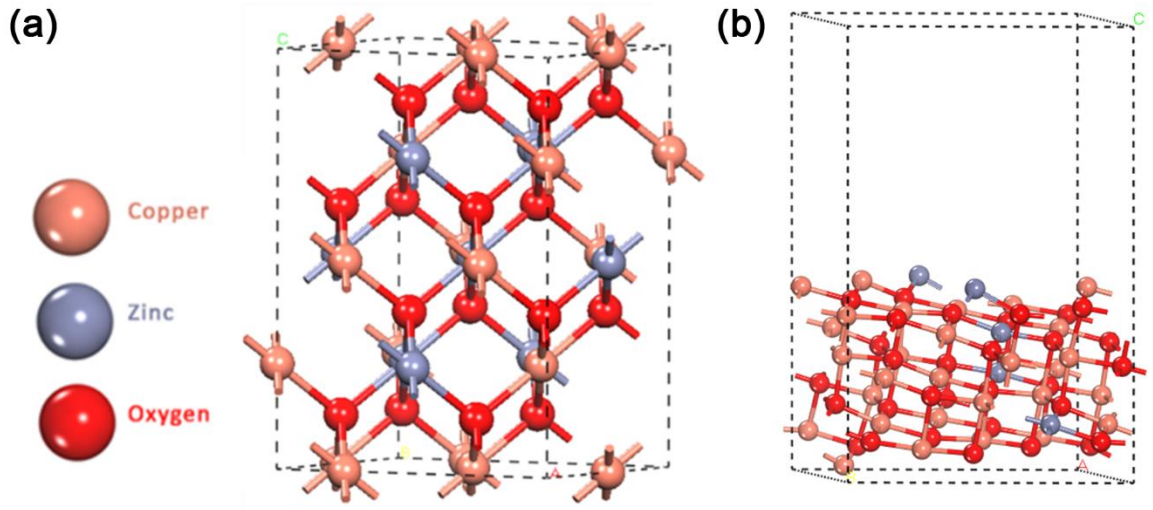

Figure 11: (a) Crystal structure of CuO doped with zinc (Cu95%, Zn5%) **(b)** surface of (-1 1 1) with a vacuum slap over the (-1 1 1) face to prevent the layer-layer interaction.

For the feasibility evaluation of the introduced defects into the crystal structure of CuO, we calculated the defect formation energy. This energy represents the essential energy for defect creation in the material and it is a significant factor in understanding the defective chemical structure of a substance. In addition to this, we also computed the binding energy for complex defects, which is a thermodynamic stability indicator that determines if a complex defect is more stable or less stable than its constituent defects. The defect formation energy of a neutral defect (D) is denoted by E_{Df} and is defined as the energy required to create a defect in the material while maintaining charge neutrality. This energy includes contributions from the change in the internal energy of the material due to the defect formation and the energy required to add or remove electrons to maintain charge neutrality. The formation energy is given by the relation:

$$E_{Df} = E_{defected} - E_{Pristine} - \sum_{i} \Delta n_i \mu_i$$

where $E_{defected}$ represents the total energy of the defected structure of CuO with Zn, while $E_{pristine}$ represent the total energies of the pristine structure of CuO. The symbol Δn_i represents the difference between the number of a particular species (i) present in the pristine supercell and the number of the same species present in the defected supercell. In other words, it quantifies the change in the number of species i due to the introduction of a defect into the crystal lattice. For instance, if the pristine supercell contains 10 oxygen atoms and the defected supercell contains 9 oxygen atoms, then Δn_i for oxygen would be -1, indicating a decrease of one oxygen atom due to the introduction of the defect. Similarly, if the defected supercell contains an additional 2 zinc atoms compared to the pristine supercell, then Δn_i for zinc would be +2, indicating an increase of two zinc atoms due to the introduction of the defect. Eventually, μ_i symbolizes the chemical potential of a given species i. The complex dielectric function (ε) can be described as:

$$\varepsilon = \varepsilon_1 + i\,\varepsilon_2$$

where ε_1 is the real part while ε_2 is the imaginary part of the dielectric constant. The estimation of the imaginary part of the dielectric function involves using a particular relationship or equation. The dielectric function is a complex-valued function that describes the response of a material to an applied electric field. It is often represented by two components: the real part and the imaginary part. The imaginary part of the dielectric function is related to the absorption of light by the material, and it can be calculated using a variety of theoretical and experimental methods. One common approach involves using a relationship or equation that takes into account the electronic structure and optical properties of the material. The specific relationship or equation used to estimate the imaginary part of the dielectric function may depend on the specific material

being studied and the computational or experimental techniques being used:

$$\varepsilon_2(\omega) = \frac{2\,e^2\pi}{\Omega\varepsilon_o} \sum k, v, c\, |\langle\varphi_k^c|H'|\varphi_k^c\rangle|^2\, \delta(E_k^c(\vec{k}) - E_k^v(\vec{k}) - \hbar\omega) \quad (28)$$

The symbol Ω represents the unit cell volume, ħω represents the photon energy, and H' denotes the electromagnetic disturbance applied to the normal Hamiltonian that separates the valence and conduction band Bloch states at wave vector k. The δ-function is used to ensure energy conservation at k. The imaginary part of the dielectric constant is calculated first, using the relationship between the photon energy and the matrix element. From this, the real part of the dielectric constant can be obtained using the Kramers-Kronig transform, which considers the causal response of the dielectric constant. The dielectric constant is a function of frequency and can be separated into electronic and lattice vibrational contributions. The electronic contribution dominates at high frequencies, while the lattice vibrational contribution dominates at low frequencies. Based on the calculated dielectric constants, other optical properties such as refractive index, extinction coefficient, absorption coefficient, reflectivity, and energy-loss spectrum can be determined using specific relationships or equations that depend on the material being studied and the experimental or computational methods being used [160].

4.2 Computational methods of the effect of defects on the photoelectrochemical characteristics of Diamond

In order to study the properties of a diamond sample, computational calculations were performed using a spin-polarized density functional theory (SPDFT). These calculations were carried out using the Cambridge Serial Total Energy Package (CASTEP) as implemented in Materials Studio 2017. Generalized gradient approximation (GGA) and the Perdew-Wang 1991 (PW19) exchange-correlation functional were used for the geometry optimization, electronic property calculation, and adsorption energy computation. The selection of the PW19 exchange-

correlation functional was based on try and error until founding the most accurate functional that gave the exact value of the diamond band gap compared to experimental results [161].

The calculated band gap using PW19 was found to be 5.2 eV, which was slightly lower than the experimental band gap of 5.4 eV with an accepted error less than 4%. For an accurate representation of the interaction between electrons and ions; this interaction can be represented using various types of pseudopotentials that mimic the behavior of the electrons and ions, an OTFG (optimized, transferable, and generalized) ultrasoft pseudopotential was used. The use of an ultrasoft pseudopotential is advantageous because it allows for a more efficient and accurate calculation of the electronic structure of the material. To ensure accurate calculations, the Broyden-Fletcher-Goldfarb-Shanno (BFGS) algorithm was utilized, which is a commonly used algorithm for minimizing functions in computational studies. The BFGS algorithm was used in conjunction with a cutoff energy of 440 eV and a separation distance of 0.05 Å for the K-points.

These parameters were chosen to ensure that the calculations were efficient and accurate. In addition to the selection of appropriate computational methods, it is important to ensure that the calculations have converged to an accurate solution. In this study, convergence was ensured by relaxing the bulk structure of the diamond sample until specific convergence criteria were met. These criteria included less than 5.0×10^{-6} eV/atom, 0.01 eV/Å, 0.02 GPa, and 5.0×10^{-4} Å for the energy, force, stress, and displacement, respectively.

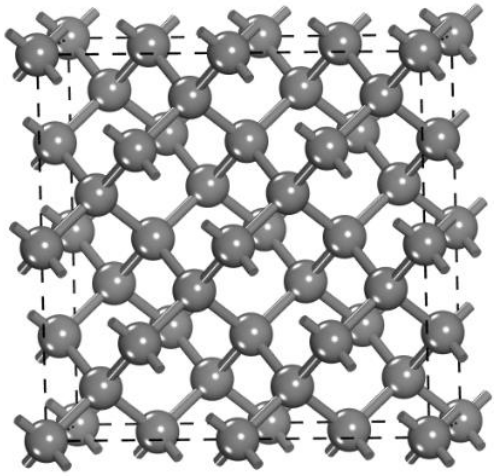

Figure 12: Pristine Diamond crystal structure.

In the process of geometry optimization for diamond, a pre-existing structure from the Material's Studio database was used. To ensure the accuracy and efficiency of the computational setup, the positions of the atoms and lattice parameters were compared with those obtained from a previously published work by Wen et al. Hence, the computational setup was able to avoid the time-consuming process of generating a new structure from scratch. This allowed for a more efficient optimization process and reduced the likelihood of errors in the generated structure.

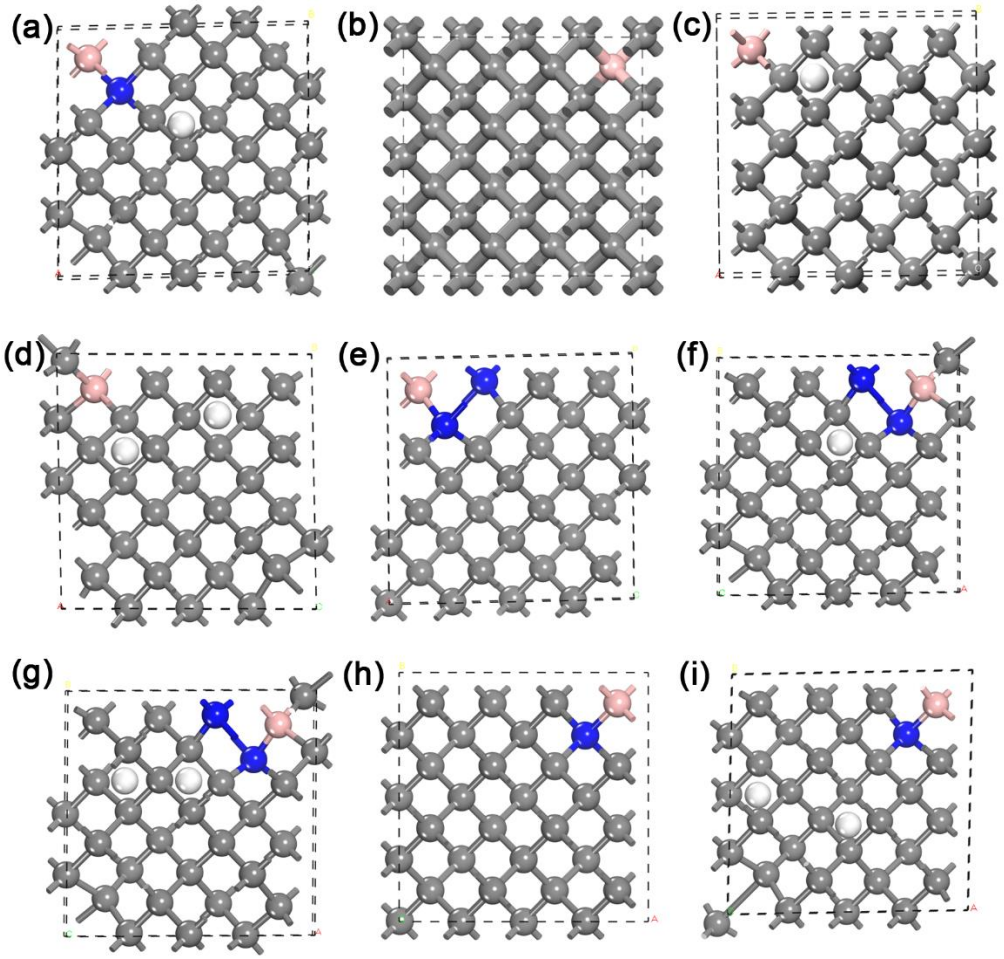

Figure 13: Doped structure of Diamonds, orange for Boron, blue for Nitrogen and white for Hydrogen **(a)** 1B – 1N – 1H -Diamond **(b)** 1B -Diamond **(c)** 1B -1H Diamond **(d)** 1B –2H -Diamond **(e)** 1B – 2N -Diamond **(f)** 1B – 2N – 1H -Diamond **(g)** 1B – 2N – 2H -Diamond **(h)** 1B – 1N -Diamond **(i)** 1B – 1N – 2H -Diamond

In this study, our main dopant is Boron with different ratios of 1, 2, and 3 atoms per cell, that is equivalent to 3.13%, 6.25%, and 9.38% of the total number of atoms (32 atom). Then for each case we tried the effect of adding Nitrogen as a substitution defect then hydrogen in the interstitial positions. Additionally, we calculated the electronic band structure, and optical properties for the purpose of better understanding the effect of doping as shown in Figure 13.

Chapter 5
Results and Discussion

5.1 The effect of defects on the photoelectrochemical characteristics of Diamond

After building the bulk structure of Diamond and performing the relaxation step, we compared the band gap of our simulated structure with the experimental one. We found a great agreement between our calculated results of 5.179 eV, shown in Figure 14, and the previously reported values in literature of 5.2 eV.

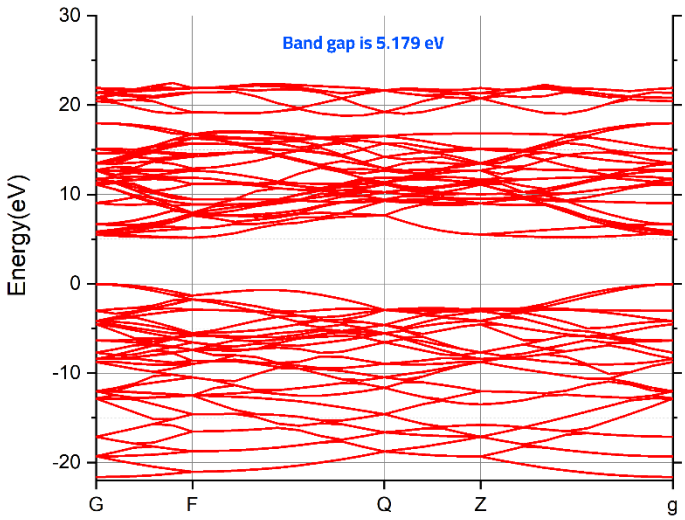

Figure 14: Band structure of pristine diamond

On the other hand, the calculated partial density of states, shown in Figure 15, proofs the band structure diagram where the maximum energy of the valence band (MVB) and the minimum energy of the conduction band (MCB) is occuring at the same momentum value in the Brillouin zone. Which indicates it is a direct band gap. Therefore, we inspected the optical properties of the doped structures focusing on the absorption and dielectric constants mainly. Absorption is an important property in water splitting because it determines how effectively a material can absorb

light and convert it into chemical energy. In order to efficiently split water using solar energy, the material used as a catalyst must be able to absorb light across a wide range of wavelengths. The absorption of a material is determined by its electronic structure and the band gap, or the energy difference between the valence and conduction bands.

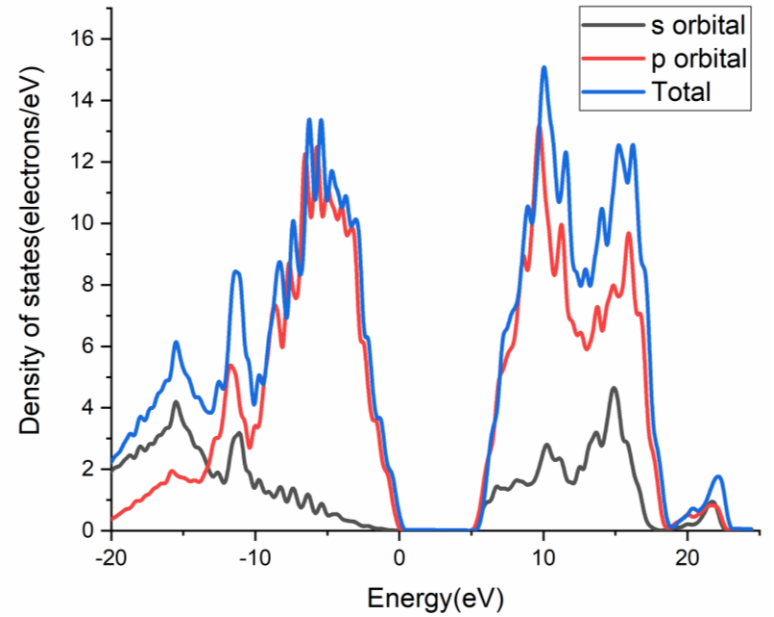

Figure 15: Partial density of states (PDOS) of pristine diamond

Materials with a narrow band gap are able to absorb light more effectively across a wide range of wavelengths, which makes them good candidates for use in water splitting reactions. In addition to the absorption of the material, other factors such as the efficiency of charge separation and the stability of the catalyst are also important for efficient water splitting. However, the absorption property is particularly important because it determines how much of the solar energy can be converted into chemical energy, which is the ultimate goal of water splitting. Therefore, it is crucial to get an idea over the absorption profile for pristine diamond to be our reference while comparing with the doped structures as shown in Figure 16.

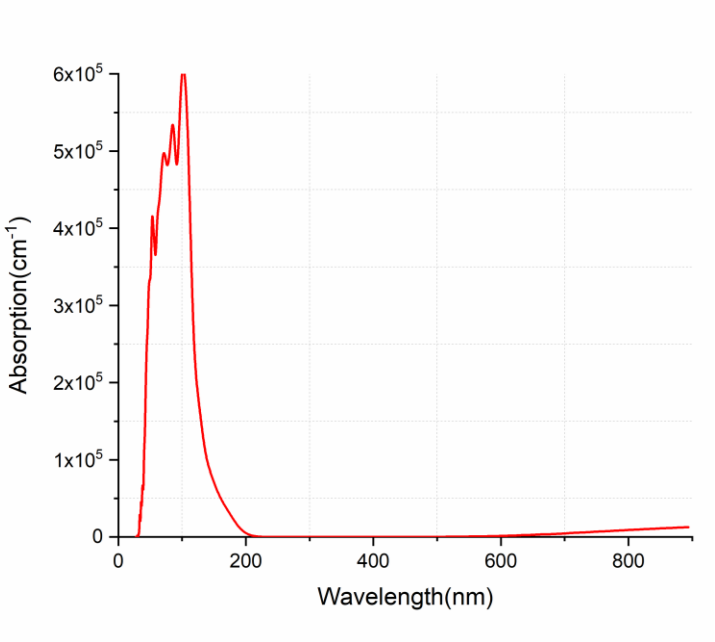

Figure 16: The normalized absorption coeffecient for pristine diamond

It is worth mentioning that dielectric constant or relative permittivity, is an important material property that describes how easily a material can be polarized by an electric field. The dielectric constant is defined as the ratio of the electric flux density in a material to the electric flux density in a vacuum, under the same electric field strength. It is a dimensionless quantity and is denoted by the symbol ε. The importance of the dielectric constant lies in its impact on the behavior of electric fields in the material. A high dielectric constant indicates that a material can be easily polarized by an electric field, while a low dielectric constant indicates that a material is less easily polarized. In dielectric materials, the dielectric constant is an important parameter for understanding the material's ability to store electrical energy and to insulate against electrical charges. Hence the calculated dielectric function is shown in Figure 17.

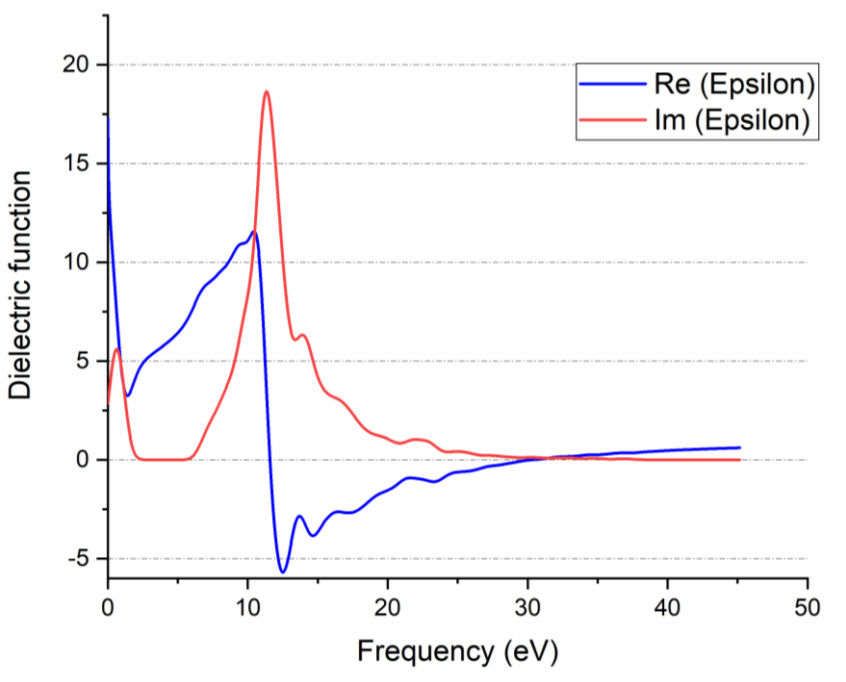

Figure 17: Dielectric function of the pristine diamond without doping, the blue represents the real part (static dielectric constant) while the red represents the imaginary part(loss)

Then, we selected different types of dopants such as Boron, Nitrogen, and Hydrogen. The selection of Boron and nitrogen was due to their similar electronic configuration like carbon, as Boron has 5 electrons in its shell, while Nitrogen has 7 electrons. Hydrogen has a small size, high diffusivity, high concentration, shallow energy levels, and is low cost that make it a popular choice for use as an interstitial dopant in semiconductors. Its properties make it useful for controlling the electrical properties of a semiconductor and for creating new materials with specific properties. It is worth noting that Boron and nitrogen are two of the most common dopants found in natural diamond. When these elements are introduced into the diamond lattice as impurities, they can significantly alter the material's electrical and optical properties. Boron is a p-type dopant, which means it introduces holes (positive charge carriers) into the diamond lattice. As a result, boron-doped diamonds are highly conductive and have a high thermal conductivity. Boron-doped diamonds also exhibit interesting optical properties, such as a deep

blue color and strong absorption in the ultraviolet region.

Nitrogen is an n-type dopant, which means it introduces electrons (negative charge carriers) into the diamond lattice. Nitrogen-doped diamonds can exhibit a range of colors, including yellow, orange, and brown, depending on the specific nitrogen configuration. Nitrogen-doped diamonds also have interesting optical properties, such as strong photoluminescence and high refractive index. Interestingly, when both boron and nitrogen are present in a diamond lattice, they can form complexes that have unique optical and electrical properties. For example, the boron-nitrogen complex in diamond has been shown to exhibit strong photoluminescence and may have potential applications in quantum information processing. Hence, we had three main concentrations of boron, then we tailored the resulted electronic and optical properties by introducing the doped structure to nitrogen atom as a substitution defect and hydrogen as an interstitial defect with different concentrations.

5.1.1 Doping 1B

A diamond supercell is a larger unit cell made up of multiple individual diamond unit cells, which are the basic building blocks of diamond crystal structures. In our specific case, the diamond supercell contains a total of 32 carbon atoms. The supercell is doped with a single boron atom, which represents a concentration of 4.16%. This means that out of the 32 atoms in the supercell, only one is a boron dopant.

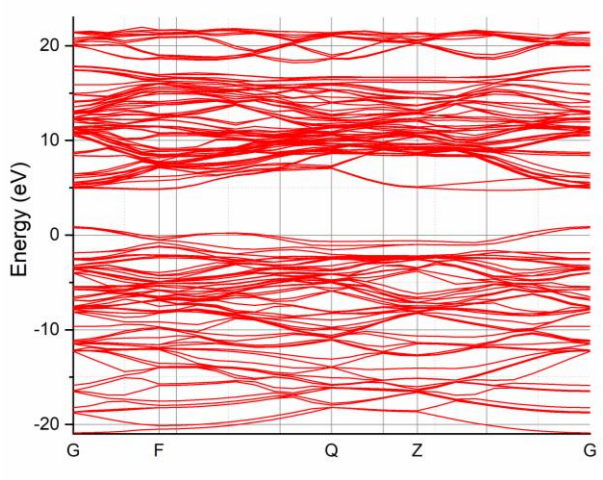

Figure 18: Band structure of Diamond doped with one boron atom as a substitution defect.

Despite the low concentration of the boron dopant, its presence has a significant impact on the electronic properties of the material. Specifically, the boron dopant changes the type of the material by controlling the band gap to be 3.58 eV, as shown in Figure 18. The band gap is the energy difference between the valence band (the highest energy band of filled electron states) and the conduction band (the lowest energy band of empty electron states) in a semiconductor material.

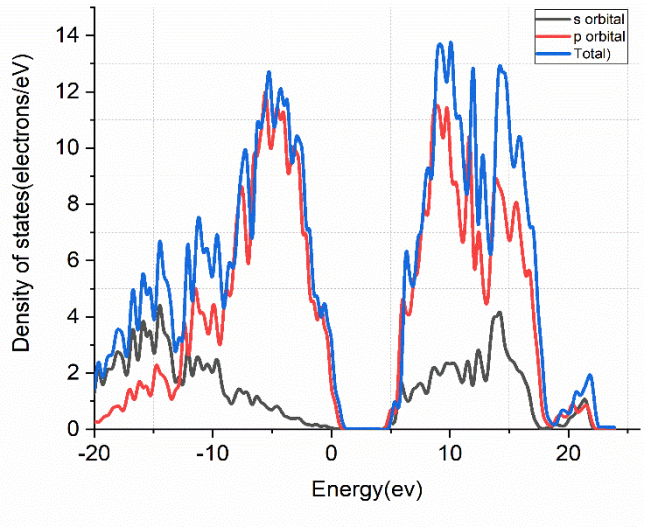

Figure 19: Partial density of states (PDOS) for the diamond doped with one boron atom.

In order to gain a better understanding of the behavior of the boron-doped diamond supercell, a partial density of states (PDOS) calculation was performed. This calculation shows the contribution of each orbital to the overall band structure of the material. Figure 19 shows the results of the PDOS calculation, which indicates that the boron dopant has increased the density of states (DOS) of the p orbital. This increase in the DOS of the p orbital has caused a shift in the Fermi level of the material towards the valence bands. The Fermi level is a measure of the energy at which electrons in a material are at thermal equilibrium, and it is often used as a reference point for measuring the energy of electrons in the material. When the Fermi level shifts towards the valence bands, it is a result to an increase in the number of available holes, which are positively charged vacancies in the valence band.

However, the boron dopant created impurity levels within the band gap that can absorb and emit light in the visible range of the electromagnetic spectrum. This means that the material can exhibit interesting optical properties, such as strong absorption and emission of light in the visible range. Figure 20 shows a tiny increase in absorption coefficient in the visible light region between 300 to 700 nm.

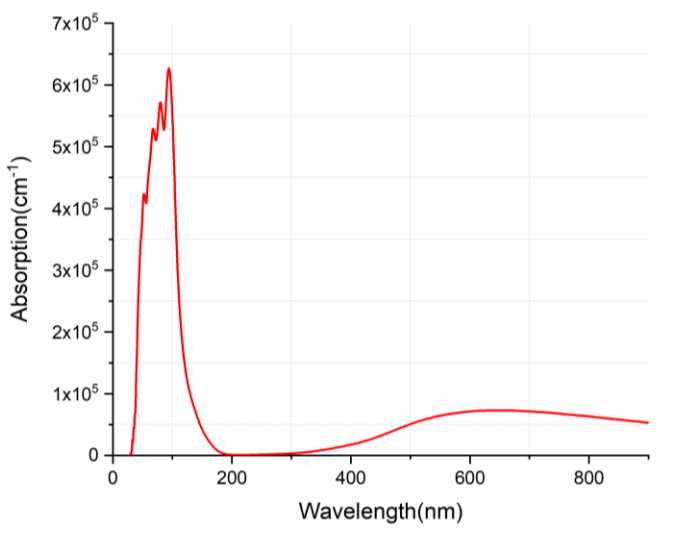

Figure 20: Normalized absorption coefficient for the diamond doped with one boron atom.

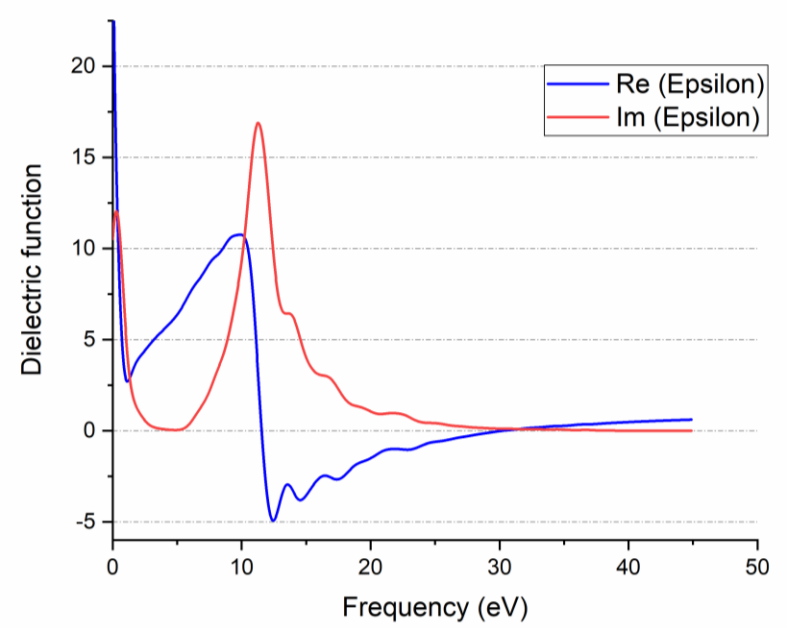

Figure 21: Dielectric constants of the 1B-diamond

On the other hand, the static dielectric constant increased from 18 for the pristine diamond to 36 for the doped structure with 1 boron atom as shown in Figure 21. It is worth mentioning that the static dielectric constant of water plays an important role in the ability of the water molecules to be polarized by the applied electric field. A higher static dielectric constant indicates that the water molecules are more easily polarized by the electric field, leading to a higher efficiency of the water splitting process. This is because the polarization of the water molecules results in a higher concentration of ions at the electrode surface, which increases the rate of the electrochemical reactions involved in the process. In addition, the static dielectric constant of water also affects the stability of the intermediate species formed during the water splitting process, particularly the oxygen evolution reaction (OER) intermediates. These intermediates are highly reactive and can undergo various side reactions that can reduce the efficiency of the water splitting process. The high static dielectric constant of water can stabilize these intermediates and prevent these side reactions, leading to a higher efficiency of the water splitting process.

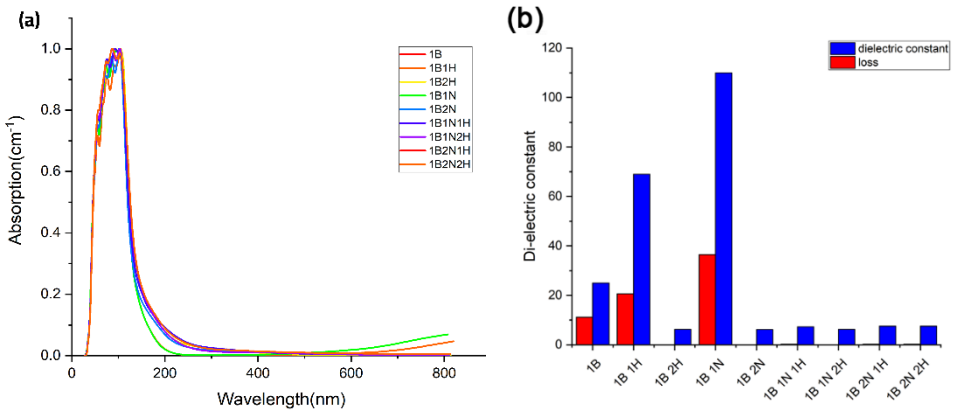

Figure 22: (a) Absorption for the defected structures **(b)** Di electric values for each structure.

As doping one atom of boron enhanced some optical properties but on the other hand lost the semiconductor behavior of the material, therefore we tried adding hydrogen atoms as an interstitial's defects. These interstitial hydrogens are introducing a stress overall the atoms in the crystal that is causing a decrease in the carbon-carbon bond length in addition to increasing the density of electron clouds by introducing the electrons of the s orbital. As expected, adding one hydrogen atom in an interstitial defect position caused a widening of the band gap as it became 4.9 eV. This behavior could be explained from the PDOS shown in Figure 24, that lowered the number of holes in the valence band compensating that in the conduction band and shifting the fermi level a bit more towards the conduction band allowing for a band gap of 4.9 eV, as shown in Figure 23.

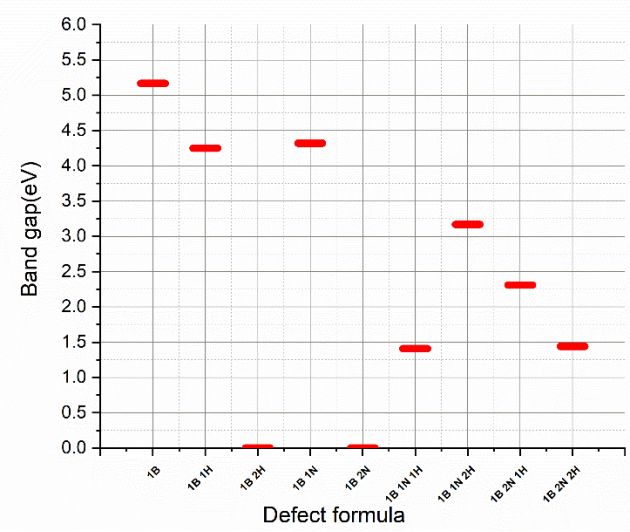

Figure 23: Band Gap distribution for each defect

Alternatively, that has no effect on the absorption coefficient of the material in the visible spectrum region, while the static dielectric constant value increased with low loss and high Dielectric constant of the absorbed energy. Following, the absorption behavior of our defected materials shown in Figure 22(a), we can conclude that the process of making defects with 1 Boron atom introduced in this study has small effect on the absorption coefficient in the visible light region.

The highest Dielectric constant could be found in case of doping 1 Boron and 1 Nitrogen as substitution defects, which is reflected on its band structure that shows a direct band gap of 3.4 eV shown in Figure 22(b). That could be explained from the PDOS graph of it shown in Figure 24. It shows an increase in the conduction band DOS supported by the p orbital making the fermi level move a bit far from the valence band position.

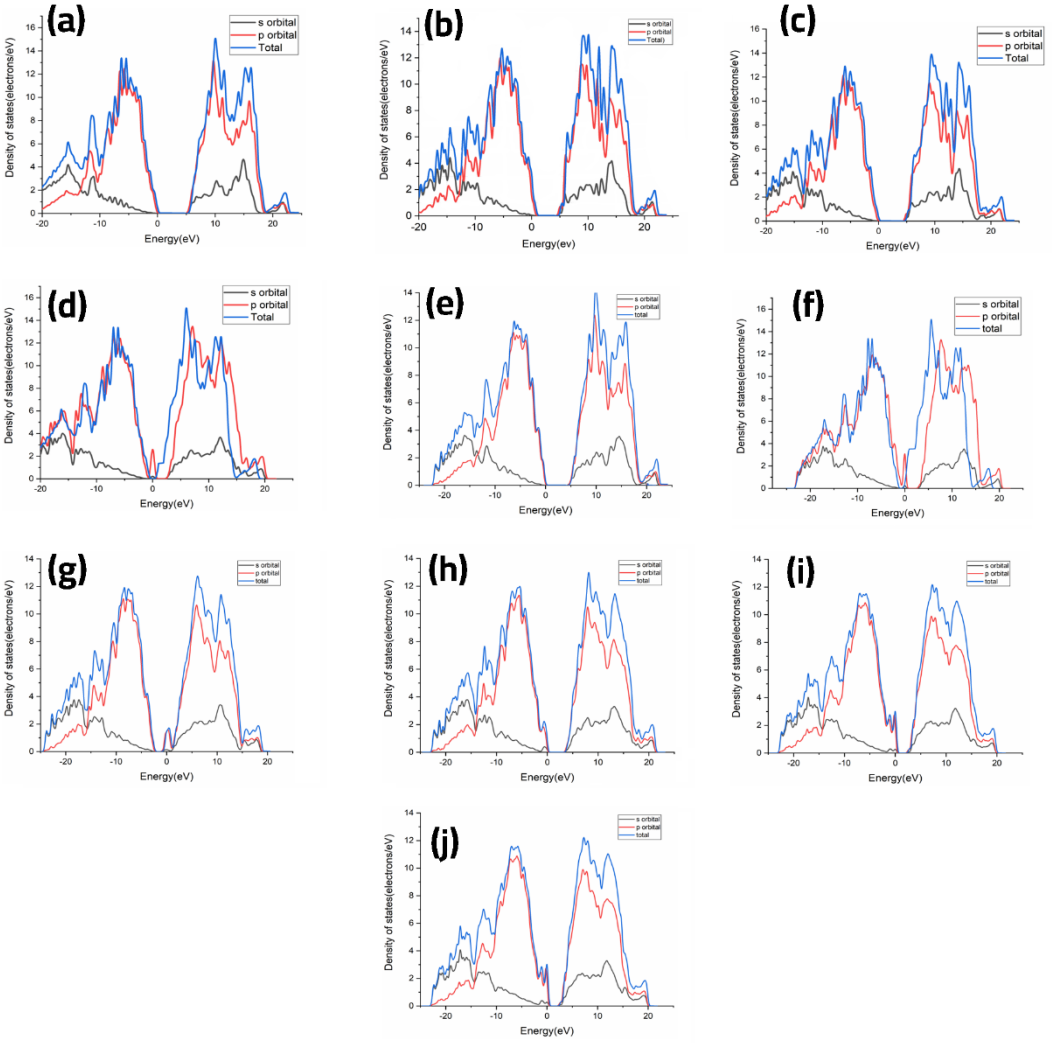

Figure 24: Partial density of states for each defect **(a)** Pristine-Diamond **(b)** 1B – Diamond **(c)** 1B– 1H -Diamond **(d)** 1B –2H -Diamond **(e)** 1B – 1N -Diamond **(f)** 1B – 2N –Diamond **(g)** 1B – 1N – 1H -Diamond **(h)** 1B – 1N – 2H -Diamond **(i)** 1B – 2N – 1H -Diamond **(j)** 1B – 2N – 2H -Diamond

5.1.2 Doping 2B

In this case we increased the dopant concentration ratio of substitution boron atoms, the concentration became 6.25%. Comparing to the band structure of 1B as a dopant, we found insignificant increase in the holes ration in the valence band while keeping it with 3.13 eV band gap as shown in Figure 25(a). The PDOS shows the same behavior like in case of doping one boron but with an increase in the density of electrons coming from the p orbitals of boron to the valence band. As mentioned before, the boron atom is a p-type dopant, as expected it enhanced the holes ratio in the valence band as shown in Figure 25(b).

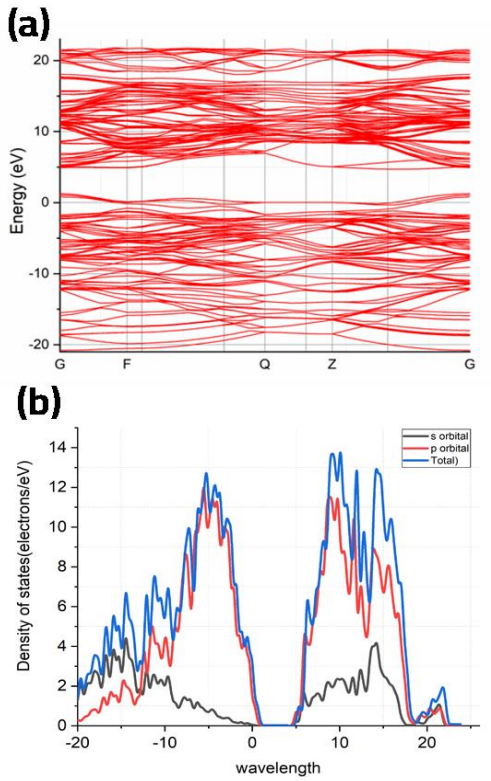

Figure 25: Diamond doped with two Boron atoms.
(a) Band structure **(b)** Partial Density of States PDOS

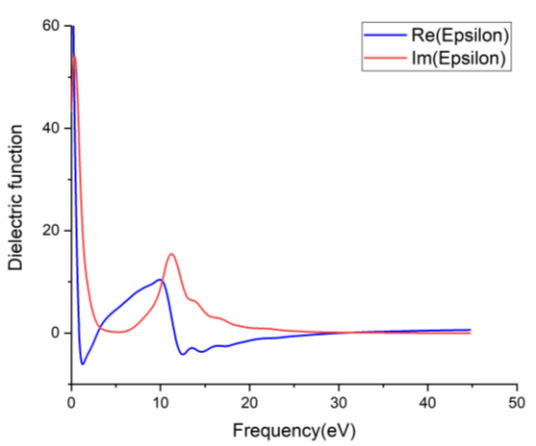

Figure 26: Dielectric constants of Diamond doped with two Boron atoms.

However, doping one boron atom has a tiny effect on the DOS in the valence band, but it significantly enhanced the absorption performance in the visible light region between 300 to 700 nm. Compared to the efficiency of the absorbed light, it also enhances the Dielectric constant of light and loss as well as shown in Figure 26, the static dielectric constant at zero energy was improved for the real and imaginary part as well.

When two boron atoms and one hydrogen atom are added to a material as an interstitial defect, the band structure shows a 2.6 eV band gap, resulting in an enhancement of Dielectric constant and loss due to the static dielectric constant. However, the PDOS analysis indicates that adding one hydrogen atom into the interstitial position has no observable effect on the electron and hole density. There is only a small decrease in the absorption coefficient in the visible light region. On the other hand, when two boron atoms and two hydrogen atoms are added as an interstitial defect, the band structure shows a band gap of zero eV, and there is an enhancement in the Dielectric constant and loss due to the static dielectric constant. The PDOS shows an increase in the DOS of the p orbital, which causes a shift of the Fermi level towards the conduction band. As

a result, there is a more significant drop in the absorption compared to the case of one hydrogen.

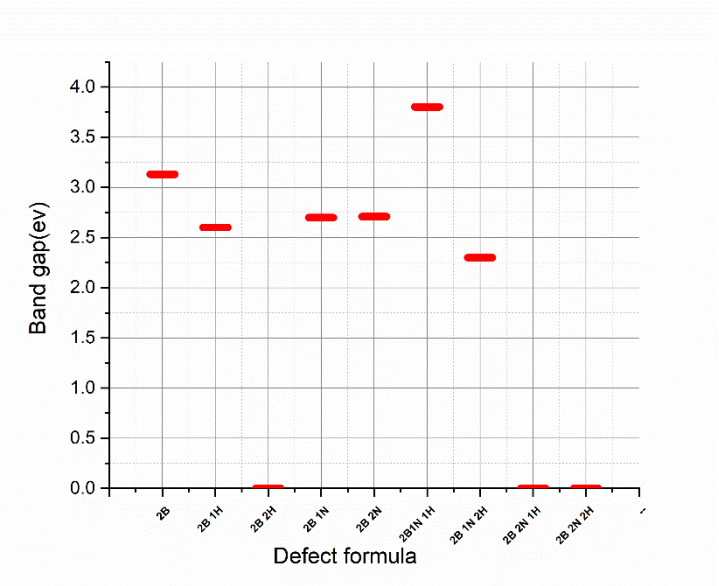

Figure 27: Band Gap comparison for each defect

Moving on to substitution defects, when two boron atoms and one nitrogen atom are added, the band structure shows no band gap. There is a slight enhancement in the Dielectric constant and loss, but it is almost negligible compared to the case of doping with two boron atoms and two hydrogen atoms. The PDOS shows an increase in the DOS of p orbitals in the conduction band with no change in the Fermi level position. The absorption also decreases in the visible light region, but it still remains within acceptable limits.

When two boron atoms and nitrogen atoms are added as a substitution defect, the band structure shows a band gap of 2.7 eV, resulting in a slight decrease in Dielectric constant and loss due to the static dielectric constant, which is similar to the case of doping with two boron atoms and two hydrogen atoms. The PDOS shows a good enhancement in the DOS of the p orbitals in the conduction band, causing a shift of the Fermi level towards the conduction band. However, the absorption in the visible light region is significantly lower than the case of doping with one nitrogen.

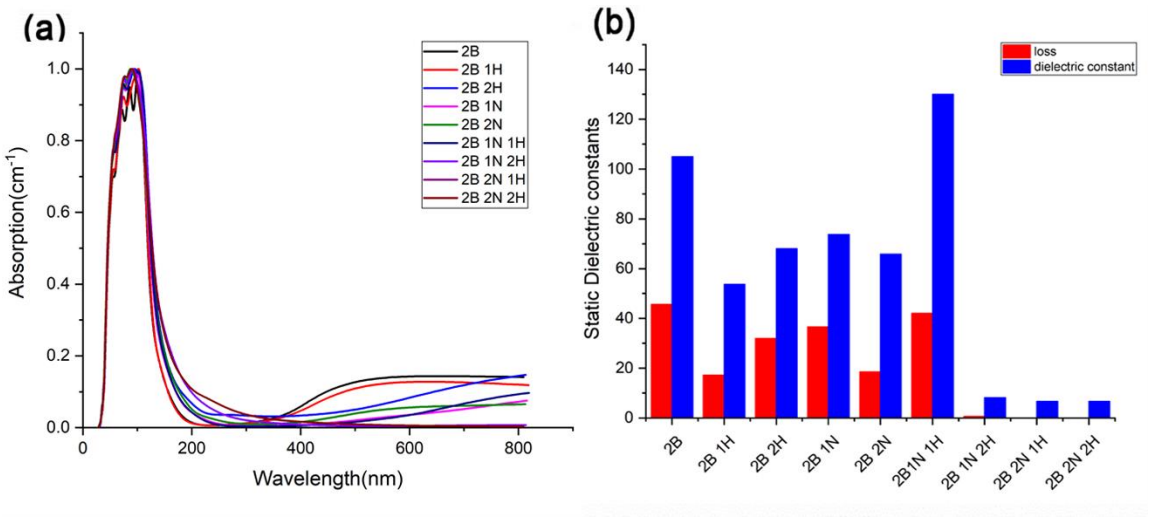

Figure 28: (a) Normalized Absorption coefficient **(b)** Values of static Dielectric constants.

When two boron atoms and one nitrogen atom are added as a substitution defect and one hydrogen atom is added as an interstitial defect, the band structure shows a band gap of 3.8 eV. The static dielectric constant significantly enhances the Dielectric constant while lowering the loss, making it the best case among the doped structures. The PDOS shows a small increase in the DOS of the p and s orbitals, causing a shift in the Fermi level far away from the valence band. The absorption graph shows a small increase in the visible light region compared to the case of 2B-1N.

In contrast, when two boron atoms and one nitrogen atom are added as a substitution defect and two hydrogen atoms are added as an interstitial defect, the band structure shows a band gap of 3.17 eV, and there is a significant drop in the Dielectric constant and loss due to the static dielectric constant. The PDOS shows new p and s orbitals in the valence band, causing a shift of the Fermi level towards the valence band, resulting in an expansion to the band gap. The absorption has significantly decreased in the visible light region. When two boron atoms and two nitrogen atoms are added as a substitution defect, supported with one or two hydrogen atoms as an interstitial defect, the band structure shows no band gap, and there is a significant drop in the

Dielectric constant and loss due to the static dielectric constant. The PDOS shows the evolution of electrons in the conduction band, causing a shift of the Fermi level towards it. The absorption in the visible light region was almost zero.

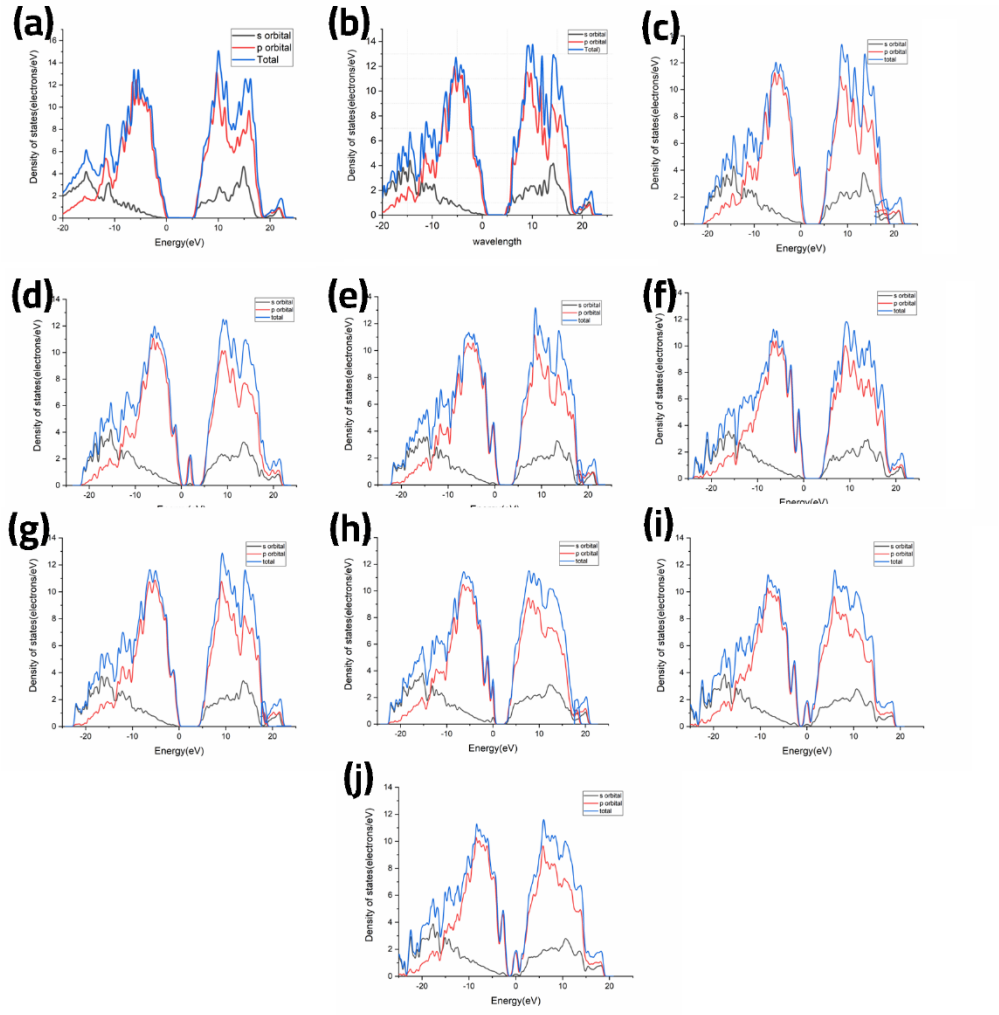

Figure 29: Partial density of states for each defect **(a)** Pristine Diamond **(b)** 2B –Diamond **(c)** 2B– 1H -Diamond **(d)** 2B –2H -Diamond **(e)** 2B –1N -Diamond **(f)** 2B –2N -Diamond**(g)** 2B –1N-1H -Diamond**(h)** 2B –1N-2H -Diamond**(i)** 2B –2N-1H -Diamond**(j)** 2B –2N-2H -Diamond

5.1.3 Doping 3B

When three boron atoms are doped into a diamond structure, the band structure shows an 2.85 eV band gap, and the static dielectric constant doubles, indicating significant polarizability in the material. However, the dielectric loss also increases, suggesting a higher energy loss in the material. The PDOS analysis indicates that substituting three boron atoms significantly affects the electrons and hole density, remarkably increasing the density of states for the holes in the valence band due to the added p orbitals in the structure.

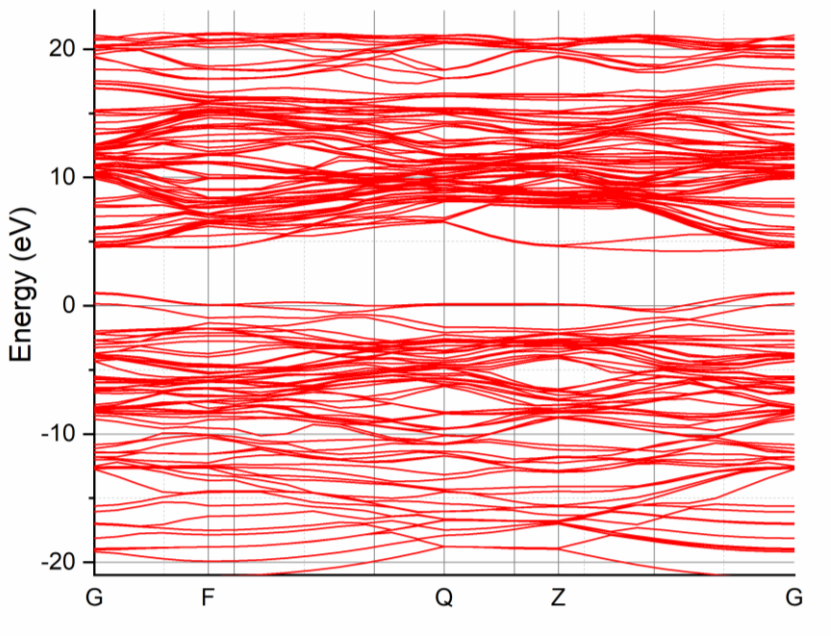

Figure 30: band structure of Diamond doped with three Boron atoms

This increase in the density of states for the holes could be responsible for enhancing the absorption in the visible light region. In contrast, the band structure shows no band gap when three boron atoms and one hydrogen atom are doped into the diamond structure. However, the static dielectric constant and loss have significantly decreased. The PDOS analysis shows that adding one hydrogen atom in the interstitial position has introduced new s and p orbitals around the gap region, causing a Fermi level shift towards the valence band, ending with a zero-band

gap. This shift of the Fermi level towards the valence band could be responsible for reducing the static dielectric constant and the loss. However, the absorption in the visible light region shows only a slight increase in its absorption coefficient, which can be neglected.

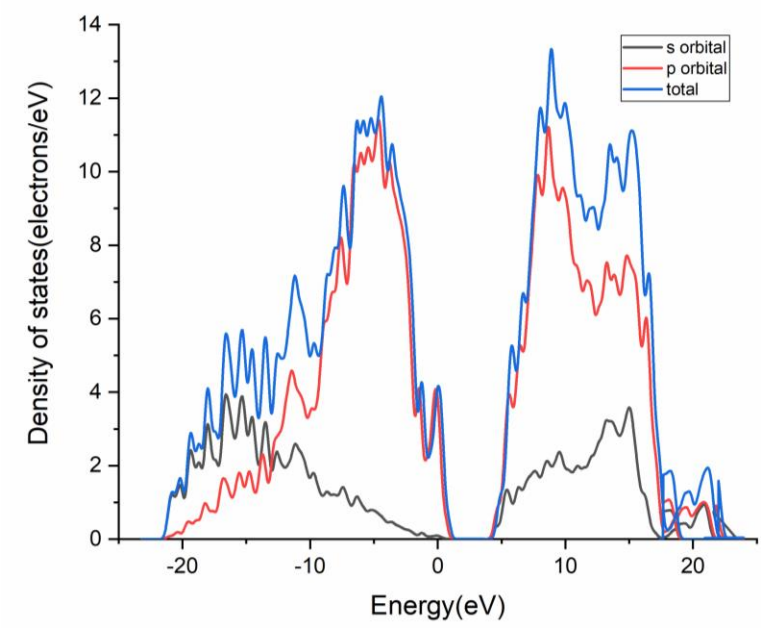

Figure 31: Partial Density of states for Diamond doped with three Boron atoms

While three boron atoms and two hydrogen atoms are doped into a diamond structure, the band structure shows a band gap of 1.32 eV, and the static dielectric constant and loss function decrease. However, adding one more hydrogen atom causes a return to an increase in the static dielectric constant and loss function. The PDOS analysis shows that adding two hydrogen atoms in the interstitial position has no observed effect on the electrons. However, it increases the density of states for the holes due to the added p vacant orbitals. This increase in the density of states for the holes causes a shift in the Fermi level away from the valence band, resulting in a new LUMO with a band gap of 1.4 eV when increasing the doped hydrogen atoms to three.

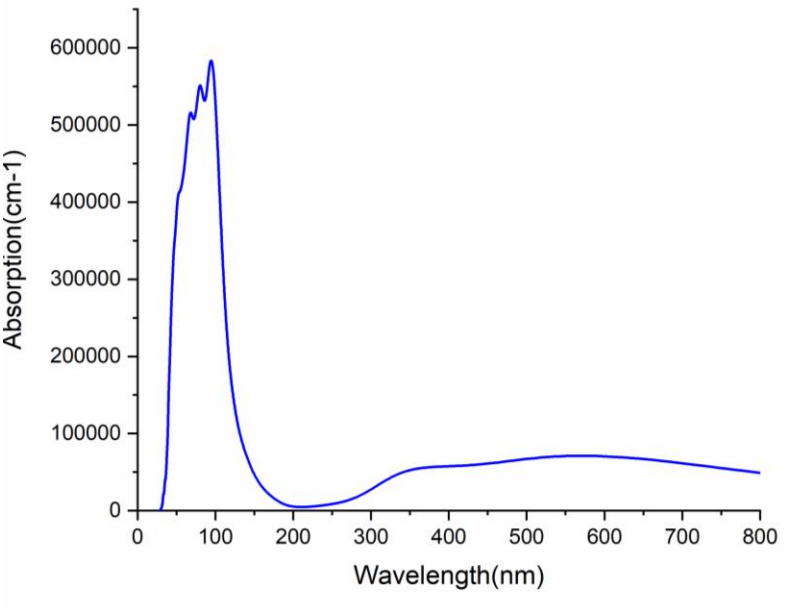

Figure 32: Normalized Absorption Coefficient of Diamond doped with three Boron atoms.

Interestingly, the absorption in the visible light region did not change, even after adding one, two, or three hydrogen atoms interstitially.

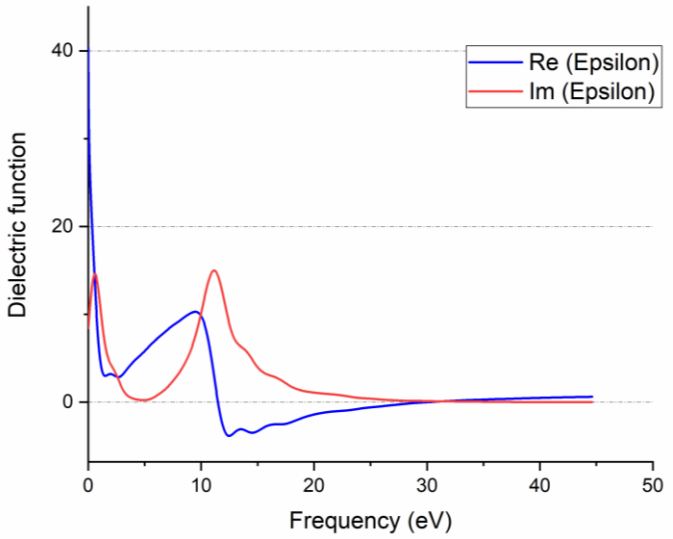

Figure 33: Dielectric constants of Diamond doped with three Boron atoms.

On the other hand, substituting one more nitrogen atom in addition to the three boron atoms' doped structure significantly enhances the absorption coefficient. This suggests that adding nitrogen atoms can significantly affect the doped material's optical properties. The PDOS analysis provides insights into the electronic properties of the doped materials, explaining the changes observed in the band structure and absorption.

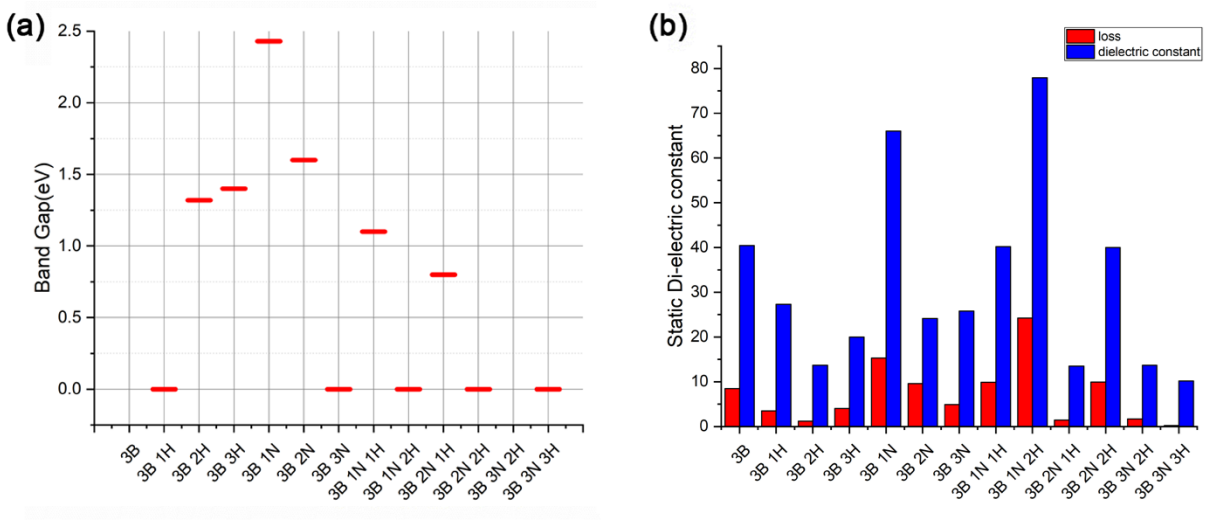

Figure 34: **(a)** Normalized Absorption coefficient **(b)** Values of static Dielectric constants.

In contrast to the previous cases, adding one or two more nitrogen atoms has an adverse effect on the absorption efficiency, as shown by the PDOS profile. The PDOS analysis indicates a narrow expansion of the region near low frequencies, suggesting the introduction of new bands in the material when doped with three hydrogen atoms interstitially. When adding one nitrogen atom, the dielectric constant reaches its highest value but with a higher loss. However, when introducing two or three nitrogen atoms, the dielectric constant drops with almost the same ratio for the real and imaginary parts. This drop in the dielectric constant suggests a reduction in the material's ability to store electrical energy in an electric field. The higher loss observed in the case of one nitrogen atom may be due to the increased polarizability of the material, which leads to a higher energy loss. The PDOS analysis provides insights into the electronic properties of the

doped materials, explaining the changes observed in the dielectric constant and absorption efficiency.

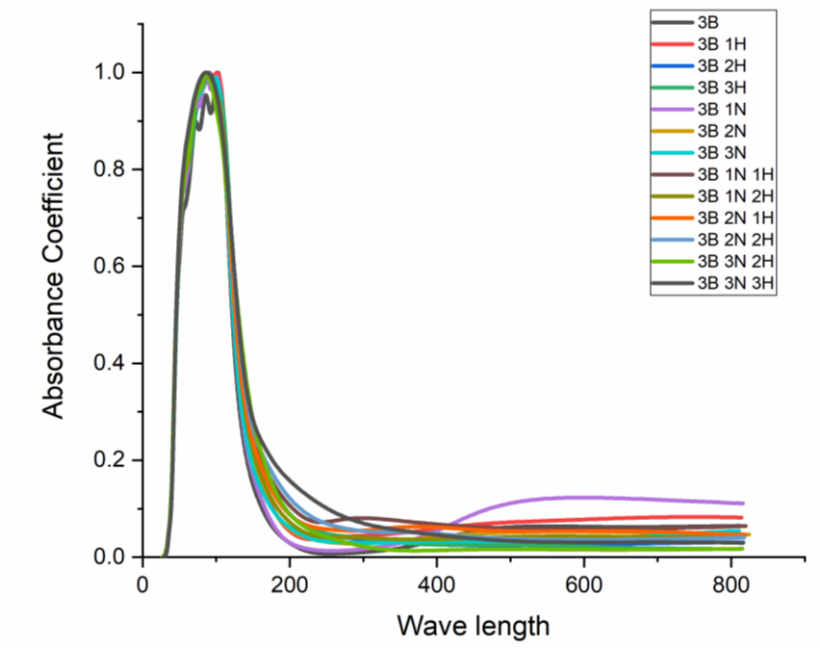

Figure 35: Normalized Absorption Coefficient comparison

In the case of doping with three boron atoms, one nitrogen atom, and one hydrogen atom as an interstitial defect, the band structure shows a band gap of 1.1 eV. However, if one more hydrogen atom is doped in an interstitial position, the band gap is found to be zero. This can be explained by the enrichment of the electron density in the conduction band, causing a slight shift in the Fermi level away from the valence band. As a result, doping two interstitial hydrogen atoms compared to one atom has improved the static dielectric constant and loss function. Adding more hydrogen atoms can enhance the electrical properties of the material.

Interestingly, the absorption in the visible light region did not change significantly. It shows a slight drop in its absorption in the case of one hydrogen atom, but the absorption remains almost the same when two hydrogen atoms are doped. This suggests that the addition of hydrogen atoms has a relatively slight impact on the material's optical properties.

Similarly, doping one and two hydrogen atoms to the already three boron with two nitrogen-doped structures of diamond lowers the band gap to 0.8 eV in the case of one hydrogen. In comparison, it falls to zero band gap for the two hydrogen atoms' doped structure. This behavior can be explained by the appearance of s orbitals of the hydrogen atom in the conduction band with a new LUMO line. As expected, the dielectric constant and loss dropped down in the case of one hydrogen atom but returned to an increase after introducing one more hydrogen atom. The interstitial hydrogen atoms here perform stress over the lattice that shrinks the length of the bond between carbon-nitrogen and carbon-boron atoms. This shrinkage of the bonds can cause a reduction in the polarizability of the material, which results in a lower dielectric constant.

Interestingly, the absorption of one hydrogen atom was higher than that of two hydrogen atoms. This suggests that adding one hydrogen atom has a more significant effect on the optical properties of the material than two hydrogen atoms. The PDOS analysis provides insights into the electronic properties of the doped materials, explaining the changes observed in the band structure, dielectric constant, and absorption. That could be presumed as doping a diamond structure with three boron and two nitrogen atoms, and adding one or two interstitial hydrogen atoms, reducing the band gap to 0.651 eV and 0.163 eV, respectively. The appearance of s orbitals of the hydrogen atom in the conduction band with a new LUMO line is responsible for this behavior. The dielectric constant and loss drop down in the case of one hydrogen atom but return to an increase after introducing one more hydrogen atom. The interstitial hydrogen atoms perform stress over the lattice that shrinks the bonds between carbon-nitrogen and carbon-boron atoms, reducing the polarizability of the material. Interestingly, the absorption in the case of one hydrogen atom was higher than that of two hydrogen atoms, suggesting that adding one hydrogen atom has a more significant effect on the optical properties of the material. The PDOS analysis provides insights into the electronic properties of the doped materials, explaining the

changes observed in the band structure, dielectric constant, and absorption.

In the case of doping three boron and nitrogen atoms supported by two and three interstitial hydrogen atoms, the band gap behavior shows exactly the expected scenario. Introducing two and three interstitial hydrogen atoms increases the band gap to 2.6 eV in the case of two hydrogens, while it drops to zero in the case of three hydrogen atoms. This can be explained by the PDOS, which shows an increase in the conduction band electrons due to the Fermi level shift towards it. In contrast, introducing one more hydrogen atom applies stress over the atoms, causing a narrowing in their bond lengths, which establishes a DOS from the p orbitals that changes the LUMO and HOMO. Similarly, the absorption was higher in the case of two hydrogens than in three. This suggests that the addition of two hydrogen atoms has a more significant effect on the optical properties of the material than three hydrogen atoms. Furthermore, the dielectric constant and loss show a lower loss that almost reaches zero in the case of three hydrogen atoms. This low loss is due to the reduction in the polarizability of the material caused by the shrinkage of the bonds between carbon-nitrogen and carbon-boron atoms.

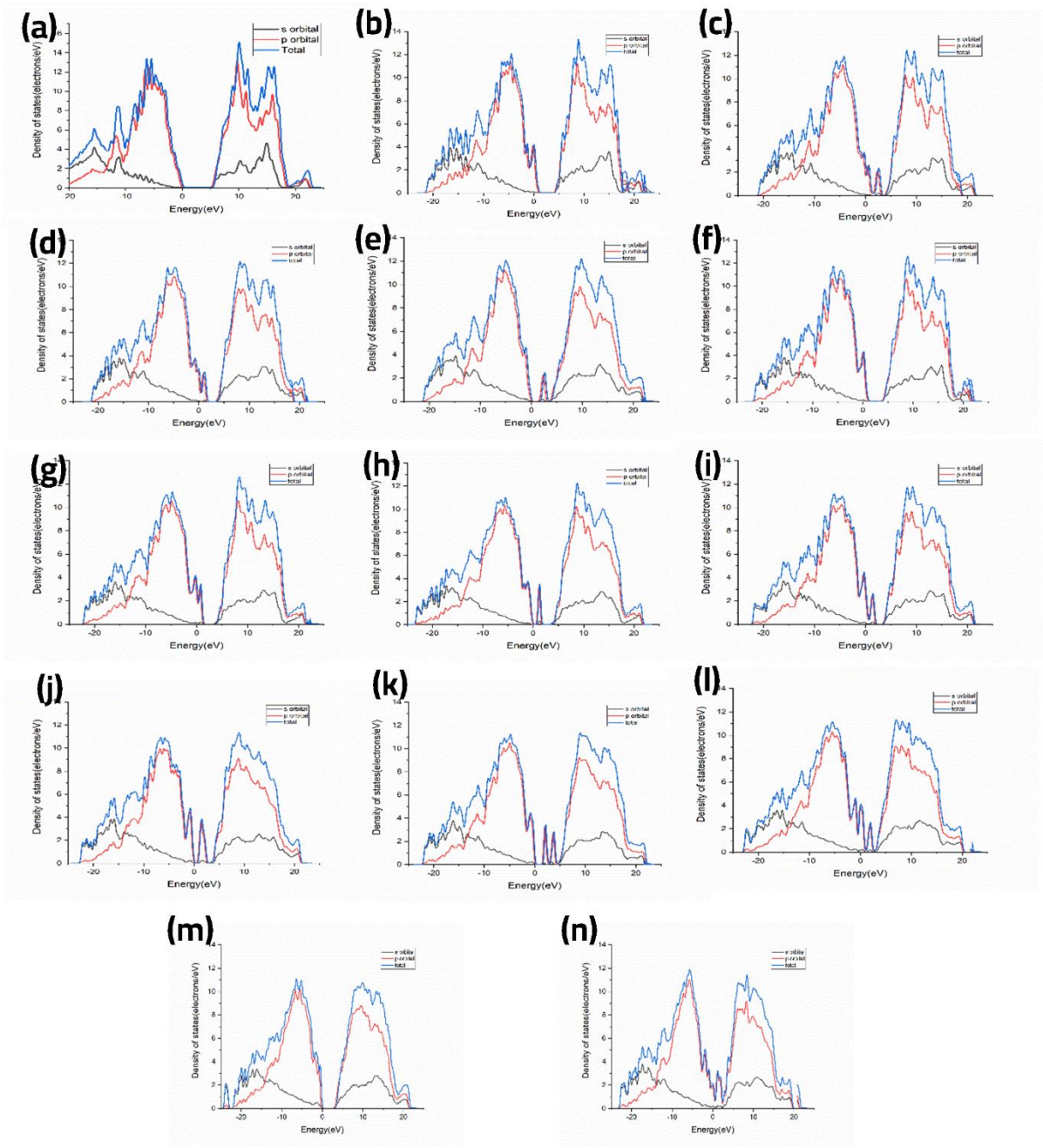

Figure 36: Partial density of states for each defect **(a)** Pristine Diamond**(b)** 3B –Diamond **(c)** 3B– 1H -Diamond **(d)** 3B –2H -Diamond **(e)** 3B –3H -Diamond **(f)** 3B –1N -Diamond **(g)** 3B –2N-Diamond **(h)** 3B –3N -Diamond **(i)** 3B –1N-1H -Diamond **(j)** 3B –1N-2H -Diamond **(k)** 3B –2N-1H -Diamond **(l)** 3B –2N-2H -Diamond **(m)** 3B –3N-3H -Diamond **(n)**3B –3N-3H -Diamond

5.2 The effect of defects on the photoelectrochemical characteristics of CuO

The electronic properties of the CuZnO (95%Cu, 5%Zn) material were investigated to Dielectric constant a better understanding of its potential use in photoelectrochemical water splitting. The calculated electronic band structure (EBS) allows the estimation of the band gap energy and determination of the semiconductor type. The EBS calculation revealed a band gap of 1.445 eV and a shift of the Fermi level towards the valence band, as shown in Figure 37 (a)&(b), indicating a p-type semiconducting behavior. Additionally, the partial density of states (PDOS) was computed to provide statistical insights into the role of each orbital in the number of occupied and unoccupied states as shown in Figure 37(c). While the region with low energy on the left side of the Fermi level represents the valence band, the region on the right represents the conduction band. Most of the state of the d orbital could be found in the valence band, which supports the hypothesis that the sample has a p-type semiconducting behavior. CuO is a p-type semiconductor with an indirect band gap of 1.2 eV. The band gap of CuO determines its electronic and optical properties and is an important characteristic for its potential application in optoelectronic devices5. In our study, it was found that the band gap of CuO increased to 1.42 eV (experimentally), and 1.44 (computationally) due to the added Zn to the material. Specifically, the Zn d orbitals caused a slight shift in the energy of the conduction band away from the Fermi level, leading to a widening of the band gap. This finding could have implications for the development and optimization of CuO-based materials. Since the CuZnO structure is intended for use in photoelectrochemical water splitting, it is important to investigate its interaction with electromagnetic waves, specifically in the visible light region. The complex dielectric constant $\varepsilon(\omega)$ is a key factor in understanding this interaction. By analyzing the complex dielectric constant $\varepsilon(\omega)$ insights, the behavior of the CuZnO structure, under different electromagnetic conditions, can be obtained. Overall, these investigations into the electronic properties and electromagnetic

interaction of the CuZnO structure provide a foundation for its potential use in PEC. In Eq. 1, the real and imaginary parts of the equation represent the energy Dielectric constant and energy loss by the material respectively. The dielectric constant was found to be 2.26

$$\varepsilon(\omega) = \varepsilon_1(\omega) + i\varepsilon_2(\omega) \quad (1)$$

The adsorption of hydrogen on the surface of the catalysts is a major step in the hydrogen evolution reaction (HER). HER is a two-electron transfer process with one catalytic intermediate, H*. HER occurs through two individual steps, either the Volmer-Heyrovsky step or the Volmer-Tafel step. If the surface coverage of H* is low, the Heyrovsky reaction would be favored. If the surface coverage of H* is high, the Tafel reaction would be favored.

(Volmer reaction): $H^+ + e^- \rightarrow H^*$

(Tafel reaction): $2H^* \rightarrow H_2$

(Heyrovsky reaction): $H^* + H^+ + e^- \rightarrow H_2$

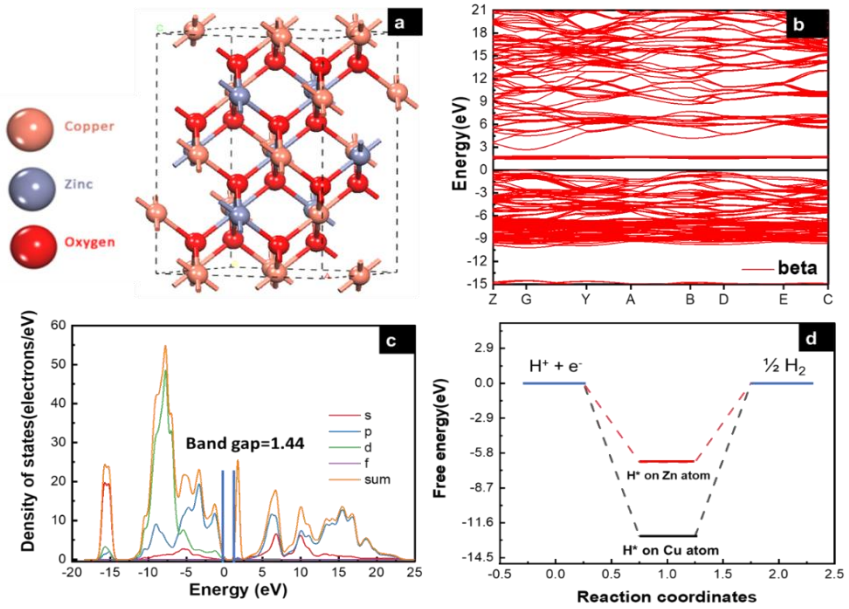

Figure 37: (a) Side-view of CuZnO bulk (95%Cu,5%Zn), **(b)** electronic band structure specified by the Fermi level with black line, **(c)** partial density of states (PDOS), and **(d)** Free energy (eV) of H* on Cu and Zn atom.

The free energy of hydrogen adsorption (ΔGH*) is an important parameter in HER. A negative ΔGH* means that H* binds favorably on the electrode surface making the Volmer reaction easy. However, if the value of ΔGH* is too large, the next Tafel or Heyrovsky step would be difficult. Therefore, ΔGH* should be close to 0 eV so that hydrogen would be able to easily adsorb and desorb from the surface of the electrode during HER. To study the catalytic activity of a CuZnO surface towards HER, it is important to identify the most favorable adsorption site for hydrogen on the surface of the catalyst. In this study, the adsorption energy (Eads) of hydrogen on the Cu and Zn atoms of the CuZnO catalyst was calculated as:

$$E_{ads} = E_{H+surface} - E_{surface} - \frac{1}{2}E_{H_2} \quad (29)$$

where $E_{H+surface}$ is the total energy of the hydrogen atom on the surface, $E_{surface}$ is the total energy for the (-1 1 1) surface, and E_{H_2} is the energy of the hydrogen molecule in vacuum. The calculations showed that the adsorption energy of H* on the Cu atom is lower than that on the Zn atom. This indicates that the adsorption of H* on the Cu atom is more favorable than that on the Zn as illustrated in Figure 37(d). The low ΔGH* on the Cu atom can block the desorption of H_2 molecules. Therefore, substituting zinc atoms in the cupric oxide lattice leads to bringing the value of the free energy of hydrogen adsorption closer to 0 eV, implying that hydrogen will easily adsorb and desorb in the case of CuZnO structure more than mere CuO.

Chapter 6

Conclusion and Future Work

This thesis tried to answer the question of how different types and concentrations of defects affect the optical and electronic properties of a catalyst used in photoelectrochemical reactions. The study focused on several categories of dopants, including boron and nitrogen atoms substituted into the material and interstitial hydrogen atoms. These dopants were chosen for their ability to enhance the catalytic properties of the material.

The study found that the type and concentration of dopants significantly impacted the band gap, dielectric constant, and material absorption. For category one of doping one Boron atom as a substitution defect, the band gap of diamond was successfully decreased to be 3.74, 3.42, and 2.68 ev for diamond doped with 1B-1H, 1B-1N, and 1B-1N-2H, respectively. Additionally, those defective structures showed almost the same absorption coefficients that are better than that of the pristine diamond. The highest dielectric constant was 110 for the structure of the diamond doped with 1B-1N, while for the diamond doped with 1B-1H was 65, which both are higher than the calculated dielectric constant for pristine diamond. On the other hand, the band gap for category two of doping two Boron atoms was decreased more than category one of doping one Boron. The lowest band gap was found to be 0.185 ev for the diamond doped with 2B-2H, while the highest value was 3.1 ev for the diamond doped with 2B-1N-1H, which shows the highest absorption coefficient value and dielectric constant. It is worth noting that diamond doped with 2B-2H also shows a promising ability to absorb light in the visible light region but with poor dielectric constant. The diamond-doped structure with 2B-2N showed a low dielectric loss function with a band gap of 2.35 ev and an excellent

absorption coefficient in the visible light region. For the last category of diamond doped with three boron atoms, the general characteristic is their shallow dielectric loss. They gave the best absorption coefficients for a wide range of visible light wavelengths; the highest absorption was for the diamond-doped structure with 3B-1N, which, unfortunately, has zero band gap. The best band gap was 2.1 eV for the diamond doped with 3B-3N-2H structure; it also has high absorption coefficients and appropriate dielectric constant. To validate the computational method, another structure of pristine CuO doped with Zn was investigated to calculate its optical and electronic properties and compared with the experimental work. The band gap for the CuO-Zn structure was found to be 1.44 ev, which agrees with the experimentally reported one of 1.44 eV.

The study also suggests that future work could be using the data calculated for feeding a machine learning module as a supervised learning model, as it has a detailed explanation of the behavior of orbitals in the band structure and how it directly affects the optical and electronic properties. It could tailor the specific band structure of a material to achieve desired optical properties by predicting the type and concentration of defects that would produce the desired performance. This could lead to the development of more efficient and applicable materials for various applications, including in fields such as electronics, optics, and energy storage.

References

1. Gowlett, John AJ. "The discovery of fire by humans: a long and convoluted process." Philosophical Transactions of the Royal Society B: Biological Sciences 371.1696 (2016): 20150164.

2. Stern, David I. "The role of energy in economic growth." Annals of the New York Academy of Sciences 1219.1 (2011): 26-51.

3. Herrero, Angel C., et al. "From the Steam Engine to STEAM Education: An Experience with Pre-Service Mathematics Teachers." Mathematics 11.2 (2023): 473.

4. Cushing, Lara J., et al. "Historical red-lining is associated with fossil fuel power plant siting and present-day inequalities in air pollutant emissions." Nature Energy 8.1 (2023): 52-61.

5. Arrhenius, Svante. "XXXI. On the influence of carbonic acid in the air upon the temperature of the ground." The London, Edinburgh, and Dublin Philosophical Magazine and Journal of Science 41.251 (1896): 237-276.

6. He, Changpei, et al. "A review of datasets and methods for deriving spatiotemporal distributions of atmospheric CO2." Journal of Environmental Management 322 (2022): 116101.

7. Rezaei Sadr, Nahid, Tarokh Bahrdo, and Rahim Taghizadeh. "Impacts of Paris agreement, fossil fuel consumption, and net energy imports on CO2 emissions: a panel data approach for three West European countries." Clean Technologies and Environmental Policy 24.5 (2022): 1521-1534.

8. Shan, Changgong, et al. "Observations of atmospheric CO2 and CO based on in-situ and ground-based remote sensing measurements at Hefei site, China." Science of The Total Environment 851 (2022): 158188.

9. Max Roser, Hannah Ritchie, Esteban Ortiz-Ospina and Lucas Rodés-Guirao (2013) - "World Population Growth". Published online at OurWorldInData.org. Retrieved from: 'https://ourworldindata.org/world-population-growth' [Online Resource] https://ourworldindata.org/world-population-growth last visited June 16th 2023

10. Hasanuzzaman, M., et al. "Energy demand." Energy for sustainable development. Academic Press, 2020. 41-87.

11. Dietz, Thomas, and Eugene A. Rosa. "Effects of population and affluence on CO2 emissions." Proceedings of the National Academy of Sciences 94.1 (1997): 175-179.

12. Wei, Ting, et al. "Developed and developing world responsibilities for historical climate change and CO2 mitigation." Proceedings of the National Academy of Sciences 109.32 (2012): 12911-12915.

13. Wang, Mengxia, et al. "Heterogenous Effects of Circular Economy, Green energy and Globalization on CO2 emissions: Policy based analysis for sustainable development." Renewable Energy 211 (2023): 789-801.

14. Liu, Zhu, et al. "Monitoring global carbon emissions in 2021." Nature Reviews Earth & Environment 3.4 (2022): 217-219.

15. Hannah Ritchie, Max Roser and Pablo Rosado (2022) - "Energy". Published online at OurWorldInData.org. Retrieved from: 'https://ourworldindata.org/energy' [Online Resource]

16. Wei, T. Y., et al. "A review on the characterization of hydrogen in hydrogen storage materials." Renewable and Sustainable Energy Reviews 79 (2017): 1122-1133.

17. Mansilla, Christine, et al. "Hydrogen applications: Overview of the key economic issues and perspectives." Hydrogen Supply Chains (2018): 271-292.

18. Sorgulu, Fatih, et al. "Experimental investigation for combustion performance of hydrogen and natural gas fuel blends." International Journal of Hydrogen Energy (2023).

19. Zgonnik, Viacheslav. "The occurrence and geoscience of natural hydrogen: A comprehensive review." Earth-Science Reviews 203 (2020): 103140.

20. Fukuoka, Hiroaki, et al. "Absolute concentration measurement for hydrogen." Energy Procedia 29 (2012): 283-290.

21. Dincer, Ibrahim. "Green methods for hydrogen production." International journal of hydrogen energy 37.2 (2012): 1954-1971.

22. Züttel, Andreas, et al. "Hydrogen: the future energy carrier." Philosophical Transactions of the Royal Society A: Mathematical, Physical and Engineering Sciences 368.1923 (2010): 3329-3342.

23. Peters, Glen P. "Carbon footprints and embodied carbon at multiple scales." Current Opinion in Environmental Sustainability 2.4 (2010): 245-250.

24. Grisham, L. R. "Nuclear Fusion in: Future Energy, Improved, Sustainable and Clean Options for our Planet, Edited by Trevor M. Letcher." (2008): 291-301.

25. Alamoud, A. R. M. "Characterization and assessment of spectral solar irradiance in Riyadh, Saudi Arabia." Journal of King Saud University-Engineering Sciences 12.2 (2000): 245-254.

26. Ding, Yulong, et al. "Solar electrical energy storage." Solar Energy Storage. Academic Press, 2015. 7-25.

27. Kumi, Ebenezer Nyarko. "Energy storage technologies." Pumped Hydro Energy Storage for Hybrid Systems. Academic Press, 2023. 1-21.

28. Cooper, Jasmin, et al. "Hydrogen emissions from the hydrogen value chain-emissions profile and impact to global warming." Science of The Total Environment 830 (2022): 154624.

29. Woods, Philip, Heriberto Bustamante, and Kondo-Francois Aguey-Zinsou. "The hydrogen economy-Where is the water?." Energy Nexus 7 (2022): 100123.

30. Idriss, Hicham. "Hydrogen production from water: past and present." Current Opinion in Chemical Engineering 29 (2020): 74-82.

31. Baykara, Sema Z. "Hydrogen: A brief overview on its sources, production and environmental impact." International Journal of Hydrogen Energy 43.23 (2018): 10605-10614.

32. Yalamati, Hari Pavan Sriram, R. K. Vij, and Rohit Srivastava. "Hydrogen production driven by nuclear energy." Solar-Driven Green Hydrogen Generation and Storage. Elsevier, 2023. 347-362.

33. Internet, in http://nsl.caltech.edu/energy.html

34. Li, Xiaona, et al. "Latest approaches on green hydrogen as a potential source of renewable energy towards sustainable energy: Spotlighting of recent innovations, challenges, and future insights." Fuel 334 (2023): 126684.

35. Baykara, S. Z. "Hydrogen production by direct solar thermal decomposition of water, possibilities for improvement of process efficiency." International Journal of Hydrogen Energy 29.14 (2004): 1451-1458.

36. Baykara, S. Z., and E. Bilgen. "An overall assessment of hydrogen production by solar water thermolysis." International journal of hydrogen energy 14.12 (1989): 881-891.

37. Smolinka, Tom, Emile Tabu Ojong, and Jürgen Garche. "hydrogen production from renewable energies—electrolyzer technologies." Electrochemical energy storage for renewable sources and grid balancing. Elsevier, 2015. 103-128.

38. Kumar, S. Shiva, and Hankwon Lim. "An overview of water electrolysis technologies for green hydrogen production." Energy reports 8 (2022): 13793-13813.

39. Park, Sung-Gwan, et al. "Addressing scale-up challenges and enhancement in performance of hydrogen-producing microbial electrolysis cell through electrode modifications." Energy Reports 8 (2022): 2726-2746.

40. Frowijn, Laurens SF, and Wilfried GJHM van Sark. "Analysis of photon-driven solar-to-hydrogen production methods in the Netherlands." Sustainable Energy Technologies and Assessments 48 (2021): 101631.

41. Olmos, Fernando, et al. "Thermodynamic feasibility analysis of a water-splitting thermochemical cycle based on sodium carbonate decomposition." International Journal of Hydrogen Energy 44.8 (2019): 4041-4061.

42. Grimes, Craig A., Oomman K. Varghese, and Sudhir Ranjan. "Hydrogen generation by water splitting." Light, Water, Hydrogen: The Solar Generation of Hydrogen by Water Photoelectrolysis. Boston, MA: Springer US, 2008. 35-113.

43. Osterloh, Frank E. "Inorganic materials as catalysts for photochemical splitting of water." Chemistry of Materials 20.1 (2008): 35-54.

44. Berezin, Feliks Aleksandrovich, and Mikhail Shubin. The Schrödinger Equation. Vol. 66. Springer Science & Business Media, 2012.

45. Griffiths, David J. "The adiabatic approximation." Introduction to Quantum Mechanics, 2nd ed.; Pearson Prentice Hall: Upper Saddle River, NJ, USA (2004): 371-396.

46. Hartree, Douglas R. "The wave mechanics of an atom with a non-Coulomb central field. Part I. Theory and methods." Mathematical Proceedings of the Cambridge Philosophical Society. Vol. 24. No. 1. Cambridge university press, 1928.

47. Martin, Philippe Andre, and François Rothen. Many-body problems and quantum field theory: an introduction. Springer Science & Business Media, 2004.

48. Fischer, Charlotte Froese. "General hartree-fock program." Computer physics communications 43.3 (1987): 355-365.

49. Kambili, A., C. J. Lambert, and J. H. Jefferson. "Hartree-Fock study of phase sensitivity in disordered rings." Physical Review B 60.11 (1999): 7684.

50. Kaplan, Ilya G. The Pauli exclusion principle: origin, verifications, and applications. John Wiley & Sons, 2017.

51. Bilc, D. I., et al. "Hybrid exchange-correlation functional for accurate prediction of the electronic and structural properties of ferroelectric oxides." Physical Review B 77.16 (2008): 165107.
52. Hohenberg, Pierre, and Walter Kohn. "Inhomogeneous electron gas." Physical review 136.3B (1964): B864.
53. Fermi, Enrico. "A statistical method for the determination of some properties of atoms." Rend. Accad. Nat. Lincei 6.602-607 (1927): 32.
54. Gilbert, Thomas L. "Hohenberg-Kohn theorem for nonlocal external potentials." Physical Review B 12.6 (1975): 2111.
55. Li, Li, et al. "Kohn-Sham equations as regularizer: Building prior knowledge into machine-learned physics." Physical review letters 126.3 (2021): 036401.
56. Kohn, Walter, and Lu Jeu Sham. "Self-consistent equations including exchange and correlation effects." Physical review 140.4A (1965): A1133.
57. Negele, John W. "Structure of finite nuclei in the local-density approximation." Physical review C 1.4 (1970): 1260.
58. Grüner, G. "The dynamics of spin-density waves." Reviews of modern physics 66.1 (1994): 1.
59. Perdew, John P., Kieron Burke, and Matthias Ernzerhof. "Generalized gradient approximation made simple." Physical review letters 77.18 (1996): 3865.

60. Burke, Kieron, John P. Perdew, and Matthias Ernzerhof. "Why the generalized gradient approximation works and how to go beyond it." International journal of quantum chemistry 61.2 (1997): 287-293.

61. Schwarz, Karlheinz. "DFT calculations of solids with LAPW and WIEN2k." Journal of Solid State Chemistry 176.2 (2003): 319-328.

62. Huzinaga, Sigeru. "Basis sets for molecular calculations." Computer physics reports 2.6 (1985): 281-339.

63. Kamenev, Alex. Field theory of non-equilibrium systems. Cambridge University Press, 2023.

64. Dixit, Anant, János G. Ángyán, and Dario Rocca. "Improving the accuracy of ground-state correlation energies within a plane-wave basis set: The electron-hole exchange kernel." The Journal of Chemical Physics 145.10 (2016).

65. Kresse, Georg, and Jürgen Furthmüller. "Efficient iterative schemes for ab initio total-energy calculations using a plane-wave basis set." Physical review B 54.16 (1996): 11169.

66. Sher, A., M. van Schilfgaarde, and M. A. Berding. "Review of the status of computational solid-state physics." AIP Conference Proceedings. Vol. 235. No. 1. American Institute of Physics, 1991.

67. Freysoldt, Christoph, Jörg Neugebauer, and Chris G. Van de Walle. "Electrostatic interactions between charged defects in supercells." physica status solidi (b) 248.5 (2011): 1067-1076.

68. Bochner, S. "Bloch's theorem for real variables." (1946): 715-719.

69. Morgan, Wiley S., et al. "Efficiency of generalized regular k-point grids." Computational Materials Science 153 (2018): 424-430.

70. Schwerdtfeger, Peter. "The pseudopotential approximation in electronic structure theory." ChemPhysChem 12.17 (2011): 3143-3155.

71. Giannozzi, Paolo, Balazs Hetenyi, and Roberto Car. "Reconstruction of the all-electron wavefunction from an ultrasoft pseudo-wavefunction." APS March Meeting Abstracts. 2001.

72. Lippert, Gerald, Jürg Hutter, and Michele Parrinello. "The Gaussian and augmented-plane-wave density functional method for ab initio molecular dynamics simulations." Theoretical Chemistry Accounts 103 (1999): 124-140.

73. Fadla, Mohamed Abdelilah, et al. "Insights on the opto-electronic structure of the inorganic mixed halide perovskites γ-CsPb (I1-xBrx) 3 with low symmetry black phase." Journal of Alloys and Compounds 832 (2020): 154847.

74. Blöchl, Peter E. "Projector augmented-wave method." Physical review B 50.24 (1994): 17953.

75. Hafner, Jürgen. "Ab-initio simulations of materials using VASP: Density-functional theory and beyond." Journal of computational chemistry 29.13 (2008): 2044-2078.

76. Giannozzi, Paolo, et al. "QUANTUM ESPRESSO: a modular and open-source software project for quantum simulations of materials." Journal of physics: Condensed matter 21.39 (2009): 395502.

77. Romero, Aldo H., et al. "ABINIT: Overview and focus on selected capabilities." The Journal of chemical physics 152.12 (2020).

78. Bakhtiar, Syed Ul Hasnain, et al. "Zinc phthalocyanine sensitized g-C3N4 photocatalyst for exceptional photocatalytic hydrogen evolution and pollutant degradation." International Journal of Hydrogen Energy 48.43 (2023): 16320-16329.

79. Gerischer, Heinz. "Photoelectrochemical catalysis of the oxidation of organic molecules by oxygen on small semiconductor particles with TiO2 as an example." Electrochimica acta 38.1 (1993): 3-9.

80. Sopyan, Iis, et al. "Highly efficient TiO2 film photocatalyst. Degradation of gaseous acetaldehyde." Chemistry letters 23.4 (1994): 723-726.

81. Takizawa, Takuo, Tadashi Watanabe, and Kenichi Honda. "Photocatalysis through excitation of adsorbates. 2. A comparative study of Rhodamine B and methylene blue on cadmium sulfide." The Journal of Physical Chemistry 82.12 (1978): 1391-1396.

82. Zhang, Tao, et al. "Advances in dual-functional photocatalysis for simultaneous reduction of hexavalent chromium and oxidation of organics in wastewater." Environmental Functional Materials (2023).
83. Tong, Hua, et al. "Nano-photocatalytic materials: possibilities and challenges." Advanced materials 24.2 (2012): 229-251.

84. Pisula, Wojciech, et al. "Liquid crystalline ordering and charge transport in semiconducting materials." Macromolecular rapid communications 30.14 (2009): 1179-1202.

85. Nie, Jingheng, et al. "Chemical doping of lead-free metal-halide-perovskite related materials for efficient white-light photoluminescence." Materials Today Physics (2023): 100992.

86. Mitra, T. K., Ashok Chatterjee, and Sukla Mukhopadhyay. "Polarons." Physics Reports 153.2-3 (1987): 91-207.

87. García-López, Elisa I., and L. Palmisano. "Fundamentals of photocatalysis: The role of the photocatalysts in heterogeneous photo-assisted reactions." Materials Science in Photocatalysis. Elsevier, 2021. 3-9.

88. Amoresi, Rafael Aparecido Ciola, et al. "Oxygen defects, morphology, and surface chemistry of metal oxides: a deep insight through a joint experimental and theoretical perspective." Metal Oxide Defects. Elsevier, 2023. 191-215.

89. Kuklja, Maija M. "Quantum-chemical modeling of energetic materials: Chemical reactions triggered by defects, deformations, and electronic excitations." Advances in Quantum Chemistry. Vol. 69. Academic Press, 2014. 71-145.

90. Zhao, Hui, et al. "Photodeposition of earth-abundant cocatalysts in photocatalytic water splitting: Methods, functions, and mechanisms." Chinese Journal of Catalysis 43.7 (2022): 1774-1804.

91. Aggarwal, Sanjeev, and R. Ramesh. "Point defect chemistry of metal oxide heterostructures." Annual review of materials science 28.1 (1998): 463-499.

92. King, Tzu-Chyang. "Defect mode properties of self-similar symmetry order in triadic Cantor photonic crystals." Chinese Journal of Physics (2023).

93. Fang, Tsang-Tse. Elements of structures and defects of crystalline materials. Elsevier, 2018.

94. Kroger, F. A. "Defect chemistry in crystalline solids." Annual Review of Materials Science 7.1 (1977): 449-475.

95. Swaminathan, Jayashree. "The emergence of analytical techniques for defects in metal oxide." Metal Oxide Defects. Elsevier, 2023. 27-60.

96. Xie, Chao, et al. "Insight into the design of defect electrocatalysts: from electronic structure to adsorption energy." Materials Today 31 (2019): 47-68.

97. Nayfeh, Ammar, et al. "Tunable plasmon–polarizmon resonance and hotspots in metal–silicon core–shell nanostructures." AIP Advances 11.12 (2021).

98. Li, Jiangtian, and Deryn Chu. "Energy band engineering of metal oxide for enhanced visible light absorption." Multifunctional photocatalytic materials for energy (2018): 49-78.

99. Catlow, C. R. A., and A. M. Stoneham. "Ionicity in solids." Journal of Physics C: Solid State Physics 16.22 (1983): 4321.

100. Feng, Haifeng, et al. "Efficient visible-light photocatalysts by constructing dispersive energy band with anisotropic p and sp hybridization states." Current Opinion in Green and Sustainable Chemistry 6 (2017): 93-100.

101. Mahesha, A., et al. "Chromium-doped ZnO nanoparticles synthesized via auto-combustion: Evaluation of concentration-dependent structural, band gap-narrowing effect, luminescence properties and photocatalytic activity." Ceramics International 49.14 (2023): 22890-22901.

102. Zhang, Chunwei, et al. "A first-principles study of hydrostatic strain engineering on the electronic properties of β-Ga2O3." Physica B: Condensed Matter 660 (2023): 414851.

103. Kaviti, Ajay Kumar, and Siva Ram Akkala. "Influence of anodization time on Al2O3 nanoporous morphology and optical properties using energy band gap at room temperature." Results in Engineering 17 (2023): 100816.

104. Li, Shenggang, and David A. Dixon. New and Future Developments in Catalysis: Chapter 2. Structural and Electronic Properties of Group 6 Transition Metal Oxide Clusters. Elsevier Inc. Chapters, 2013.

105. Xia, Congxin, et al. "Tuning the band gap of hematite α-Fe2O3 by sulfur doping." Physics Letters A 377.31-33 (2013): 1943-1947.

106. Açıkgöz, Muhammed, et al. "Theoretical analysis of crystal field parameters and zero field splitting parameters for Mn2+ ions in tetramethylammonium tetrachlorozincate (TMATC-Zn)." Polyhedron 235 (2023): 116341.

107. Mashhadzadeh, Amin Hamed, et al. "Influence of defects upon mechanical properties of oxide materials." Metal Oxide Defects. Elsevier, 2023. 253-280.

108. Zlatar, Matija, and Maja Gruden. "Introduction to ligand field theory and computational chemistry." Practical approaches to biological inorganic chemistry. Elsevier, 2020. 17-67.

109. Takayanagi, Toshiyuki. "Two-state reactivity in the acetylene cyclotrimerization reaction catalyzed by a single atomic transition-metal ion: The case for V+ and Fe+." Computational and Theoretical Chemistry 1211 (2022): 113682.

110. Bullett, D. W. "Bulk and surface electron states in WO3 and tungsten bronzes." Journal of Physics C: Solid State Physics 16.11 (1983): 2197.

111. Hussein, Mahmoud I., and Michael J. Frazier. "Band structure of phononic crystals with general damping." Journal of Applied Physics 108.9 (2010).

112. French, M., et al. "Electronic band structure of Cu2O by spin density functional theory." Journal of Physics: Condensed Matter 21.1 (2008): 015502.

113. Yan, Hui, et al. "Band structure design of semiconductors for enhanced photocatalytic activity: The case of TiO2." Progress in Natural Science: Materials International 23.4 (2013): 402-407.

114. Hurle, D. T. J. "A comprehensive thermodynamic analysis of native point defect and dopant solubilities in gallium arsenide." Journal of Applied Physics 85.10 (1999): 6957-7022.

115. Xiao, Hao, et al. "Point defect properties in high entropy MAX phases from first-principles calculations." Acta Materialia 248 (2023): 118783.

116. Liu, X., et al. "Native point defects in low-temperature-grown GaAs." Applied Physics Letters 67.2 (1995): 279-281.

117. Grabowski, Blazej, Tilmann Hickel, and Jörg Neugebauer. "Formation energies of point defects at finite temperatures." physica status solidi (b) 248.6 (2011): 1295-1308.

118. Grieshammer, Steffen, Tobias Zacherle, and Manfred Martin. "Entropies of defect formation in ceria from first principles." Physical Chemistry Chemical Physics 15.38 (2013): 15935-15942.

119. Hagen, Michael, and Michael W. Finnis. "Point defects and chemical potentials in ordered alloys." Philosophical Magazine A 77.2 (1998): 447-464.

120. Pacchioni, Gianfranco. "Oxygen vacancy: the invisible agent on oxide surfaces." ChemPhysChem 4.10 (2003): 1041-1047.

121. Nadgornyi, Edward. "Dislocation dynamics and mechanical properties of crystals." Progress in materials science 31 (1988): 1-530.

122. Maillard, Serge, et al. "Assessment of atomistic data for predicting the phase diagram and defect thermodynamics. The example of non-stoichiometric uranium dioxide." Journal of Nuclear Materials 569 (2022): 153864.

123. Alberi, K., et al. "Valence-band anticrossing in mismatched III-V semiconductor alloys." Physical review B 75.4 (2007): 045203.

124. Zhang, Yanwen, et al. "Coupled electronic and atomic effects on defect evolution in silicon carbide under ion irradiation." Current Opinion in Solid State and Materials Science 21.6 (2017): 285-298.

125. Schmidt-Mende, Lukas, and Judith L. MacManus-Driscoll. "ZnO–nanostructures, defects, and devices." Materials today 10.5 (2007): 40-48.

126. Xie, Deqiao, et al. "A review on distortion and residual stress in additive manufacturing." Chinese Journal of Mechanical Engineering: Additive Manufacturing Frontiers (2022): 100039.

127. Sharma, Indu, et al. "Review on bandgap engineering in metal-chalcogenide absorber layer via grading: a trend in thin-film solar cells." Solar Energy 246 (2022): 152-180.

128. Abbas, M. T., et al. "Lanthanide and transition metals doped materials for non-contact optical thermometry with promising approaches." Materials Today Chemistry 24 (2022): 100903.

129. Horstmann, Robin, et al. "Structural and dynamical properties of liquids in confinements: A review of molecular dynamics simulation studies." Langmuir 38.21 (2022): 6506-6522.

130. Huang, Wei, Dongliang Zhang, and Mitang Wang. "A Review: Research Progress on Photoelectric Catalytic Water Splitting of α-Fe2O3." Current Nanoscience 19.6 (2023): 758-769.

131. Wu, Lan, et al. "Fabrication of Fe2O3/BiVO4 heterojunction by doping method to improve the solar water splitting performance of BiVO4." Journal of Alloys and Compounds 949 (2023): 169822.

132. Kaur, Jasleen, et al. "Polaron-induced metal-to-insulator transition in vanadium oxides from density functional theory calculations." Physical Review B 107.12 (2023): 125162.

133. Leopold, Nikolai, et al. "Landau–Pekar equations and quantum fluctuations for the dynamics of a strongly coupled polaron." Pure and Applied Analysis 3.4 (2022): 653-676.

134. Mardonov, Shukhrat N., et al. "Polaron Dynamics in a Quasi-Two-Dimensional Bose–Einstein Condensate." Universe 9.2 (2023): 89.

135. Mitrić, Petar, et al. "Spectral functions of the Holstein polaron: exact and approximate solutions." Physical Review Letters 129.9 (2022): 096401.

136. Ellinger, Florian, et al. "Small polaron formation on the Nb-doped SrTiO 3 (001) surface." Physical Review Materials 7.6 (2023): 064602.

137. Reticcioli, Michele, Ulrike Diebold, and Cesare Franchini. "Modeling polarons in density functional theory: lessons learned from TiO2." Journal of Physics: Condensed Matter 34.20 (2022): 204006.

138. Green, Ben L., Alan T. Collins, and Christopher M. Breeding. "Diamond spectroscopy, defect centers, color, and treatments." Reviews in Mineralogy and Geochemistry 88.1 (2022): 637-688.

139. Palyanov, Yuri N., et al. "Crystal growth of diamond." Handbook of Crystal Growth. Elsevier, 2015. 671-713.

140. Smith, J. M. "Characterisation of single defects in diamond in the development of quantum devices." Quantum Information Processing with Diamond. Woodhead Publishing, 2014. 68-97.

141. Green, Ben L., Alan T. Collins, and Christopher M. Breeding. "Diamond spectroscopy, defect centers, color, and treatments." Reviews in Mineralogy and Geochemistry 88.1 (2022): 637-688.

142. Laidlaw, F. H. J., et al. "Point defects and interstitial climb of 90° partial dislocations in brown type IIa natural diamond." Acta Materialia 201 (2020): 494-503.

143. Muruganathan, Manoharan, and Hiroshi Mizuta. "Boron vacancy color center in diamond: Ab initio study." Diamond and Related Materials 114 (2021): 108341.

144. Tan, Xin, et al. "Theoretical study on the formation of diamond germanium vacancy color center." Surface Science 715 (2022): 121950.

145. Tsubouchi, Nobuteru, and S. Shikata. "Change of structural and electrical properties of diamond with high-dose ion implantation at elevated temperatures: Dependences on donor/acceptor impurity species." Nuclear Instruments and Methods in Physics Research Section B: Beam Interactions with Materials and Atoms 286 (2012): 303-307.

146. Galimberti, Daria Ruth, et al. "Static vs dynamic DFT prediction of IR spectra of flexible molecules in the condensed phase: The (ClCF2CF (CF3) OCF2CH3) liquid as a test case." Spectrochimica Acta Part A: Molecular and Biomolecular Spectroscopy 183 (2017): 195-203.

147. Sen, Kalidas D., et al. "Atomic ionization radii using Janak's theorem." Chemical Physics Letters 325.1-3 (2000): 29-32.

148. Scharoch, Pawel, and Maciej Winiarski. "An efficient method of DFT/LDA band-gap correction." Computer Physics Communications 184.12 (2013): 2680-2683.

149. Achatz, Philipp, et al. "Isotopic substitution of boron and carbon in superconducting diamond epilayers grown by MPCVD." Diamond and related materials 19.7-9 (2010): 814-817.

150. Peaker, C. V., et al. "Assignment of 13C hyperfine interactions in the P1-center in diamond." Diamond and Related Materials 70 (2016): 118-123.

151. Gao, Nan, Lilin Gao, and Hongyu Yu. "First-principles study of N and S co-doping in diamond." Diamond and Related Materials 132 (2023): 109651.

152. Cai, Zhenghao, et al. "Fully Analyze the Mechanism of NHO Impurities Effect on Diamond Growth at Hpht." Available at SSRN 4066163.

153. Yang, Hongchao, Yandong Ma, and Ying Dai. "Progress of structural and electronic properties of diamond: a mini review." Functional Diamond 1.1 (2022): 150-159.

154. Feng, Shihao, et al. "Lithium-rich diamond-like solid electrolytes for lithium batteries." Electrochimica Acta 439 (2023): 141637.

155. Delun, Zhou, et al. "First-principles calculation to N-type LiN Co-doping and Li doping in diamond." Diamond and Related Materials 110 (2020): 108070.

156. Wang, Wennie, Anderson Janotti, and Chris G. Van de Walle. "Role of oxygen vacancies in crystalline WO 3." Journal of Materials Chemistry C 4.27 (2016): 6641-6648.

157. Clark, Stewart J., et al. "First principles methods using CASTEP." Zeitschrift für kristallographie-crystalline materials 220.5-6 (2005): 567-570.

158. Segall, M. D., et al. "First-principles simulation: ideas, illustrations and the CASTEP code." Journal of physics: condensed matter 14.11 (2002): 2717.

159. Sanad, Mohamed Fathi, et al. "Co–Cu bimetallic metal organic framework catalyst outperforms the Pt/C benchmark for oxygen reduction." Journal of the American Chemical Society 143.10 (2021): 4064-4073.

160. Himmetoglu, Burak, Renata M. Wentzcovitch, and Matteo Cococcioni. "First-principles study of electronic and structural properties of CuO." Physical Review B 84.11 (2011): 115108.

161. Imteyaz, Shahla. "Metal oxide-based optical fibers (preparation, composition, composition-linked properties, physical parameters, and theoretical calculations)." Metal Oxides for Optoelectronics and Optics-Based Medical Applications. Elsevier, 2022. 73-93.

162. Zuliani, Claudio, et al. "Properties and customization of sensor materials for biomedical applications." (2014): 221-243.